Utrecht University

CARDIFF UNIVERSITY
PRIFYSGOL CAERDYDD
School of Earth and Ocean Sciences
Ysgol Gwyddorau'r Ddaear a'r Môr

Masters thesis

Deformation mechanisms in the Gwna mélange on Anglesey (UK) and the implications for aseismic subduction zones

Aagje Eijsink

supervised by
Dr. Åke Fagereng and Dr. André Niemeijer

Abstract

The Gwna mélange, exposed on Anglesey (north Wales) allows for the study of pre-Cambrian (∼610-540 Ma) subduction-related rocks. Knowledge about how, where and why deformation has occurred in these rocks give insights about seismicity in the unaccessible rocks in currently active subduction zones. This type of field-based studies is needed to evaluate the applicability of conceptual models and laboratory experiments to natural rocks.

Microstructural observations are used to study the deformation mechanisms in these rocks, which differ between the mélange blocks and the matrix. Before any other research question can be considered, the first thing is to decipher are the main deformation phases , to see which deformation mechanisms have been active during the main subduction event. These deformation mechanisms, together with chlorite geothermometry are then used to put temperature constraints on the three deformation phases observed in these rocks.

The first deformation phase D1 is characterized by pressure solution seams parallel to the bedding, due to low temperature pressure solution as the result of vertical compaction due to the accumulation of sediments on the seafloor. The main subduction event D2 occurred mainly by deformation in the pelagic sediments, in which oblique solution seams formed, and in the basalts. Both the basalts and the sediments consist of large amounts of very fine grained muscovite, which allows easy deformation along the basal phyllosilicate planes. Within the matrix-supported microstructure there are blocks of quartz and carbonates, which show some brittle veins, but have mostly deformed by recrystallization and ductile creep processes. The occurrence of these ductile creep processes, in spite of relatively low deformation temperatures of ∼280°C, might be explained by hydrolitic weakening or high inherited dislocation densities. The last deformation event D3 developed a spaced foliation in the weak pelagic sediments and muscovite-rich basalts, and is possibly linked to continental collision late in the deformation history of these rocks.

To quantify the deformation during the main subduction event, conceptual models are used for deformation of a phyllosilicate matrix with single quartz grains and for strong quartz blocks in a weak matrix. This allowed for estimation of the differential stress and shear stress, deformation depth and strain rates in the blocks and the matrix. There was a clear distinction between strong slowly deforming blocks and high strain rates in the mélange matrix, which can reach values high enough to allow aseismic creep without the need for seismic events.

Contents

1 Introduction

Destructive plate margins, where an oceanic plate subducts under a continental plate, are often characterized by destructive, high magnitude (M_{max}>8.3) earthquakes (e.g. Sumatra, 2004; Tohoku-oki, 2011; Chile, 2016). This in contrast to other subduction zones that constantly deform by aseismic creep, with only minor (M_{max}<5.5) earthquakes (Cloos and Shreve, 1996). Examples of these are the north Hikurangi, the southern Japan trench and the Manilla Trench (Fagereng and den Hartog, 2016). Suggested reasons for differences between these Chilean-type and Marianas-type margins are related to the amount of sediment subducting and the thickness of the subduction channel shear zone (Cloos and Shreve, 1996).

These reasons are suggested based on worldwide comparisons of earthquake magnitudes and trench sediment input in major active subduction zones (Ruff, 1989). Also, lab experiments have been used to explain why seismogenesis is limited to certain depths in subduction zones (Den Hartog et al., 2013) or to test hypotheses like seismicity being the result of subducting topographic highs (Ikari et al., 2013). Ultimately, experiments have lead to conceptual models for microstructures that are thought to be present in subduction channels. However, conditions during lab experiments are different from geological conditions, especially in terms of deformation temperature and strain rate. To assess if this knowledge can be applied to actively deforming zones, we need natural samples to see what mechanisms have caused the deformation under natural conditions.

Subduction mélanges are the likely remnants of the subduction channels in exposed subduction-related rocks (Shreve and Cloos, 1986), so the study of exposed mélanges can provide insight in the deformation processes happening at depth in subduction channels. For this reason, the Gwna mélange has been investigated. The most important question in this research is what deformation mechanisms have operated in the mélange and why. In order to answer this question, microstructural observations are used.

First of all, the deformation history of the rocks must be deciphered, including what deformation mechanisms where active at different times. When this is known, the reasons for these differences are explored. Temperature plays a big role in this, which is why all possible methods are explored to find the deformation temperature, including mineralogy, deformation mechanisms and chlorite geothermometry.

The limited brittle features found, show this subduction zone was of the aseismic, Marianas-type, which fits with the limited amounts of sediments present, generally held responsible for aseismic behaviour (Cloos and Shreve, 1996). This makes it possible to use current models for aseismic behaviour in combination with models and flow laws for the found deformation mechanisms, in order to find whether or not aseismic creep rates can be fast enough to keep up with plate boundary convergence rates. This ultimately answers the question why there are no or little preserved signs of seismic activity during the deformation of this mélange.

2 Mélange deformation

This research is focussed on the deformation in the Gwna Group in Anglesey, North Wales. This is the type locality for the term mélange, a term nowadays used to describe many types of rock of various origins.

2.1 The term mélange

The word mélange, derived from the French word for mixture, is defined many times. Greenly (1919) was the first to use the word for lenticular blocks in a schistose matrix, Cowan (1985) defined mélange as fragments enveloped by a finer-grained matrix of mudstone. Raymond (1975, 1984) argued that the definition should not be based on origin, as there is no common origin for mélanges and introduced the constraint that a mélange should be mappable at a scale of 1:24000 or smaller. After the Penrose Conference on mélanges (Silver and Beutner, 1980) it became clear adjectives need to be used to distinguish different mélanges by origin, like tectonic, sedimentary, and diapiric. Unfortunately, many different adjectives are used and many authors define and use their own adjectives. All of the following terms have or can be used to describe the Gwna mélange.

2.1.1 Tectonic mélange and broken formation

The term broken formation is used to distinguish stratigraphically disrupted beds without exotic blocks from tectonic mélanges, in which mixing occurs and where both exotic and native blocks are present (Hsü, 1968). Difficulties with this division are that the term exotic is also not well defined and that the transition from broken formation to mixing in usually gradational. Tectonic mélanges occur in various settings, including strike-slip tectonics, convergent margins and intracontinental deformation (Festa et al., 2010, 2012).

2.1.2 Subduction mélange

To distinguish a subduction mélange from other tectonic mélanges, Kimura et al. (2012) suggest four key criteria that should be met. These include lithological mixing of trench-fill sediments, younging of the sediments towards the trench-fill, a shear-related fabric consistent with the relative paleo-convergence and pressure-temperature conditions in the expected range for subduction zones. The term subduction mélange is therefore more specific than tectonic mélange (Kimura et al., 2012).

2.1.3 OPS mélange

OPS is short for Ocean Plate Stratigraphy, meaning the sediments deposited on top of an oceanic plate, during its travel from a mid-ocean ridge to the subduction trench. The term OPS mélange is proposed by Wakita (2015) to describe a chaotic mixture composed only of OPS, which is mappable and has a

block-in-matrix structure. This distinguishes it from serpentinite mélanges and ophiolite or ophiolitic mélanges, which are also present at convergent margins. Important for this is the distinction between an ophiolite, which is the succession of a complete oceanic lithospheric plate and includes peridotite, layered gabbros, dykes, pillow lavas and sediments, and OPS, which is only the upper part of the ophiolite and may include basalt, limestone, chert and siliceous shale and trench turbidites. This term therefore refers to a subduction mélange with certain lithologies and is therefore even a more specific term then subduction mélange (Wakita, 2015).

2.1.4 Olistostrome

There is a clear distinction between mélange and olistostrome deposits. An olistostrome is a sedimentary layer, but is chaotic and heterogeneous. It contains blocks called olistoliths in a matrix and can be formed for example by submarine gravity sliding, like in trenches in subduction zones (Hsü, 1974). With the block-in-matrix appearance, one could argue an olistostrome is in fact a type of mélange and indeed Cowan (1985) mentions that what he defines as a type I mélange is by other referred to as olistostrome. Differences between the two are that the olistoliths can be rounded due to transport and the matrix of a mélange is pervasively sheared (Hsü, 1974). The problem arises when an olistostrome is sheared, making the distinction difficult.

2.2 Subduction mélange formation

The mechanisms of mélange formation are multiple, all leading to different types of mélanges (Fig.1). Festa et al. (2010) refer to subduction related mélanges as type 4 and distinguish two types. Mélanges of type 4a are mass-transport deposits and type 4b are tectonic mélanges due to offscraping and underplating. These 4a mass-transport deposits would be the olistostromes as described above. The type of deposit would also depend on state of consolidation of the sediments, and sedimentary mass deposits may be caused by a tectonic trigger, producing a tectonized olistostrome (Festa et al., 2010).

The formation of tectonic mélanges can be caused by offscraping of sediments, or by the widening of fault zones in a zone of underplating, driven by the tectonic motion across the subduction zone (Twiss and Moores, 1992). Cloos and Shreve (1988) suggested a subduction channel model, in which poorly consolidated sediments act as a lubricant and will underplate onto the hanging wall. In some margin types, olistostromes will be subducted, making it likely that they will become tectonized to a degree in which they are not distinguishable from mélanges any more (Cloos and Shreve, 1988). This is because they are mechanical weak and therefore easily redeformed.

This leads to the suggestion that all mélanges are olistostrome deposits, deformed by the plate boundary displacement that localizes in these weak layers (Rowe et al., 2013). Recent studies of Franciscan mélanges (Wakabayashi, 2015; Wakabayashi and Rowe, 2015) show that these indeed have a sedimentary ori-

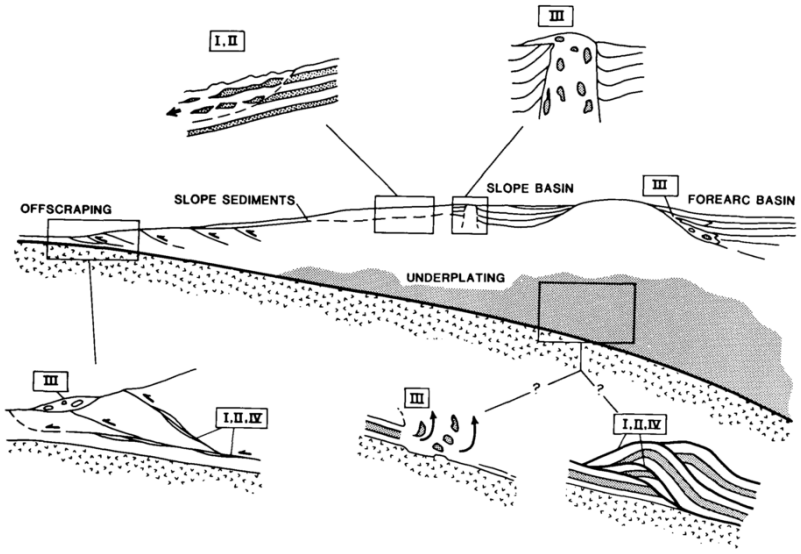

Figure 1: Mélanges form at multiple places in a subduction zone setting, including by mass wastings and by offscraping and underplating. From Cowan (1985)

gin. Displacement along the subduction plate boundary is accommodated by one or more fault strands, bounding less deformed rock (Rowe et al., 2013). The sedimentary origin of the Franciscan mélange is recognised because of exotic blocks (Wakabayashi and Rowe, 2015), but the lack of these and careful geological observations of the primary textures in the Japanese Mugi mélange are used to argue this is a true tectonic mélange (Kimura et al., 2012), so both tectonized sedimentary mélanges and true tectonic mélanges do exist.

2.3 Deformation mechanisms

The main characteristic of mélanges, with competent blocks in a weaker matrix, is that shear strain rates are inferred to have been higher in the matrix than in the competent blocks (Fagereng and Sibson, 2010). This causes the bulk rheology to be governed by the deformation of the matrix. That is, if the amount of weak material is large enough. Estimates of the amount necessary vary from 10%-20% for continuous deformation, if the weak material is interconnected (Fagereng and Sibson, 2010) to 50% for the viscosity of the rock to vary less than one order of magnitude from the matrix viscosity (Grigull et al., 2012). The most reported deformation mechanism in the matrix is dissolution-precipitation creep, allowing the matrix to be modelled as a Newtonian viscous fluid (Grigull et al., 2012).

Studies from the Mugi mélange (SW Japan) show that this dissolution-precipitation creep, or mass transfer by pressure solution, is accompanied by

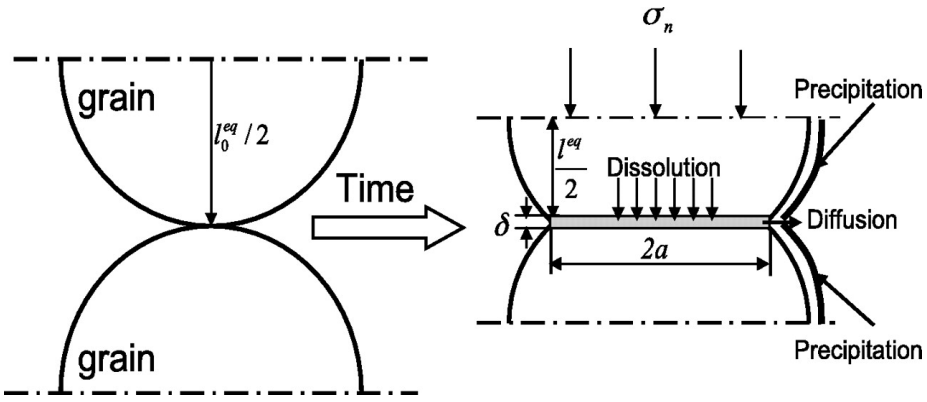

Figure 2: Pressure solution is a three-step process of dissolution at stressed grain boundaries, diffusion through a fluid phase and precipitation in unstressed regions. From Aharonov and Katsman (2009)

preferred alignment of illites (Kimura et al., 2007, 2012). The presence of Y-P and Riedel shears is the result of cataclastic deformation that accompanies the pressure solution in microshear zones (Kitamura and Kimura, 2012). The formation of a 'web' structure is reported to be the first deformation phase in this mélange (Kimura et al., 2007; Kitamura and Kimura, 2012), which is an irregular network of curviplanar dark veins, present in sandstones (Cowan, 1982).

Kimura et al. (2012) also report the presence of basaltic rocks, including hyaloclastites, in the mélange, which are deformed to foliated cataclasites with deformation concentrated in ultracataclasites which are present at the lithological boundaries.

2.3.1 Dissolution-precipitation creep

Deformation by dissolution-precipitation creep or pressure solution is one of the three diffusion creep mechanisms. It differs from the other two diffusion creep mechanisms in that it does not involve diffusion of vacancies through either the crystal lattice (Nabarro-Herring creep) or along grain boundaries (Coble creep). Instead it involves dissolution in a fluid, diffusion through the fluid phase and precipitation (Fig.2) (Knipe, 1989). The driving force for this mechanism is a gradient in solubility due to a gradient in chemical potential, which will be higher at stressed contacts than at unstressed contacts, therefore causing dissolution at stressed contacts and precipitation at unstressed contacts. It requires the presence of an aqueous fluid at the grain boundary, but the relatively low activation energy causes it to be the dominant deformation mechanism at low temperatures (Fig.3). The rate of pressure solution depends on many factors and is controlled by the slowest step of the three consecutive processes of dissolution, diffusion and precipitation. If interface kinetics (i.e. dissolution or

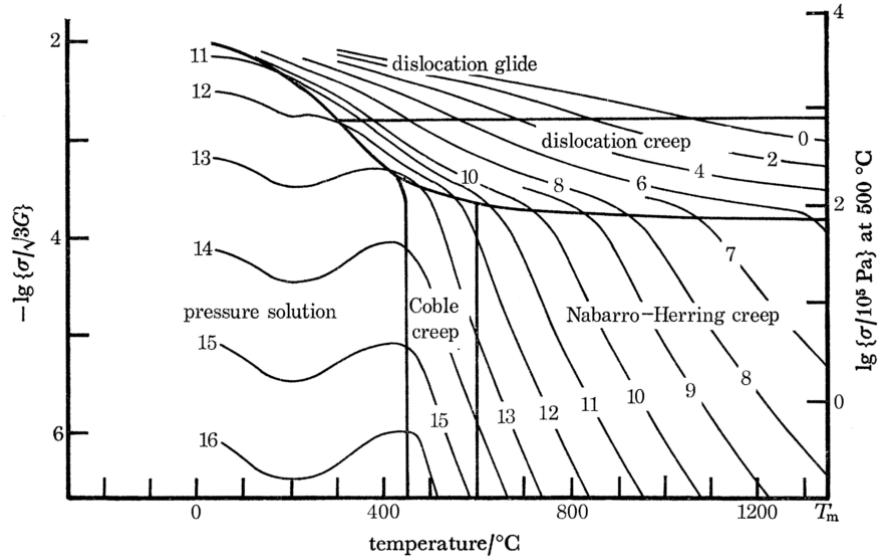

Figure 3: Typical deformation mechanism map for pure quartz with a grain size of 100μm, showing that pressure solution is dominant at low pressures and temperatures and dislocation creep mechanisms occur at higher pressures. From: Rutter (1976)

precipitation) are rate controlling, the overall rate depends linearly on grainsize, whereas diffusion-controlled pressure solution has a cubic dependence on grainsize, like Coble creep (Knipe, 1989). The presence of a second phase, especially phyllosilicates like illite and muscovite, may enhance the rate of pressure solution (Hickman and Evans, 1995).

Microstructures indicative of pressure solution include truncations, indentations and overgrowths. If material is removed out of the rock volume, also solution seams or stylolites may form. If material is added, it will generally precipitate in cracks, forming veins (Twiss and Moores, 1992).

2.3.2 Cataclasis

Diffusive deformation mechanisms are always accompanied by grain boundary sliding, to accomodate the change in grain shape. This can be frictional grain-boundary sliding without fracture, or cataclastic flow (Knipe, 1989). Cataclastic flow is a brittle process that involves the fracturing of grains and therefore causes a decrease in grainsize. Microstructures indicative of this mechanism have angular grain shapes and a broad and often fractal grain size distribution (Twiss and Moores, 1992). It occurs at low-grade metamorphic conditions (Passchier and Trouw, 1996).

2.3.3 Dislocation creep

At higher temperatures and pressures, deformation may occur by dislocation creep (Fig.3). This occurs by the motion of dislocations, which are linear lattice defects, through the crystal lattice (Knipe, 1989). The rate and microstructure are controlled by the relative rates of grain boundary migration, dislocation climb and dislocation production. Based on experimental deformation of quartz at relatively high strain rates, three different regimes are recognised by Hirth and Tullis (1992). In the lowest temperature regime 1, deformation is accomodated by grain boundary migration and new grains develop from bulges at grain boundaries. At higher temperatures, dislocation climb rates are increased and subgrains form, which causes new grains to form from progressive subgrain rotation. In the highest temperature, grain boundary migration rates are high enough to form new grains larger than subgrains (Hirth and Tullis, 1992). Temperatures associated with the three different regimes also depend on strain rate. Stipp et al. (2002a) have found these regimes in naturally deformed quartz veins. Fig.4 shows both the temperatures needed for the three regimes at the high strain rates during the experiments by Hirth and Tullis (1992) and how these relate to natural quartz veins sheared at low strain rates of 10^{-12}-10^{-14}. Temperatures found for natural conditions are 280-400°C for bulging, 400-500°C for subgrain rotation and 500-700°C for grain boundary migration (Stipp et al., 2002a).

2.4 Seismogenesis

The use of identifying the deformation mechanisms is to know where and how earthquakes may nucleate in the subduction mélange. Pseudotachylytes are the most direct evidence for seismogenic slip, but findings of these are rare in mélanges (Kimura et al., 2012). The ones found are in the upper boundary thrust or roof thrust of the duplex (Kitamura et al., 2005), which fits with the observation that slip in subduction zones is localized on thin fault surfaces (Rowe et al., 2013). The limited findings of pseudotachylytes may be explained by the large amounts of water present in the subduction zone, favouring other velocity-weakening mechanisms such as fluidization of ultracataclasite, causing a maximum temperature lower than the melting temperature (Kimura et al., 2012).

The presence of pseudotachylytes only in the roof faults led to the suggestion that the tectonic mélange deforms by a slow process, with concentrated fast episodic slip along the roof thrust (Kitamura et al., 2005). This slow process of mélange deformation is suggested to be viscous deformation of the matrix, possibly linked to slow earthquakes (Kitamura and Kimura, 2012). Fracturing of rigid lenses in a weaker, viscously deforming matrix are suggested mechanisms for tremor and slow slip (Hayman and Lavier, 2014). The flow of matrix around rigid lenses causes concentration of strain rate along the boundaries of the blocks, which may lead to brittle failure (Fagereng et al., 2014). Brittle deformation of sandstone blocks shows they are capable of releasing seismic waves

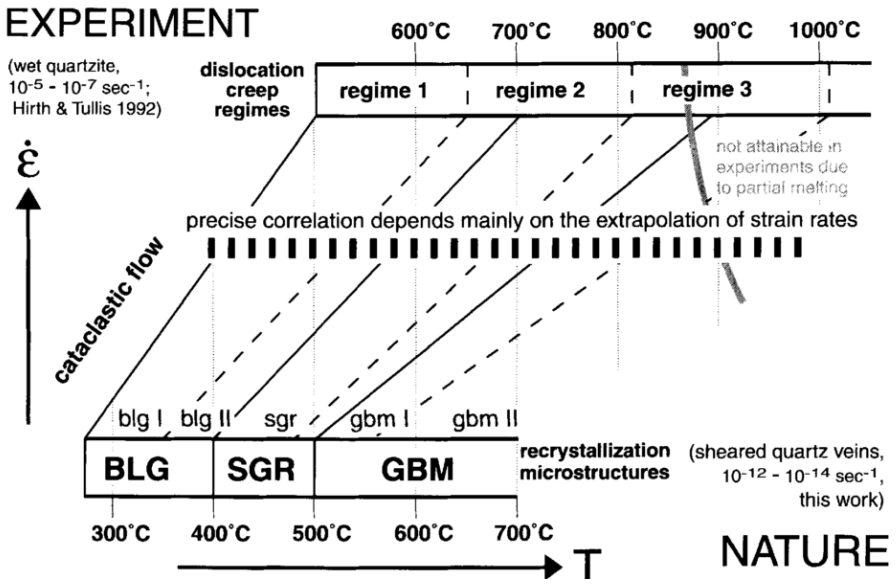

Figure 4: The three different quartz deformation mechanisms: bulging (BLG), subgrain formation (SGR) and grain boundary migration (GBM), measured in lab experiment at relatively high strain rates and temperatures (top), extrapolated to temperatures and strain rates found in deformed quartz veins (bottom). From Stipp et al. (2002a)

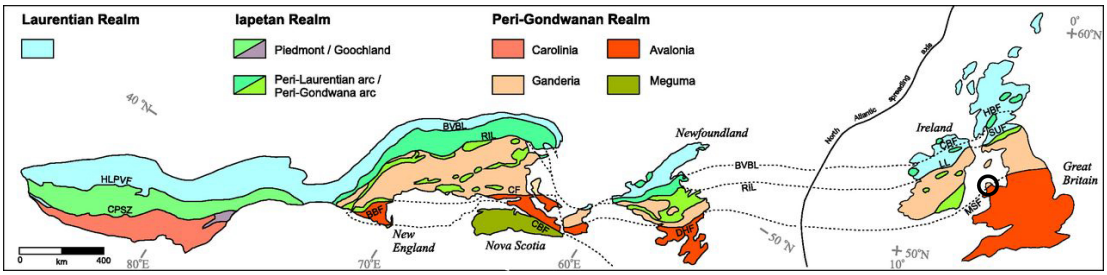

Figure 5: Terrane map showing the continuation of Avalonia and Ganderia from the UK to the Appalachians. Note the Menai Strait Fault (MSF) marking the boundary between Anglesey (middle of black circle) and the Welsh mainland. From Pollock et al. (2012)

(Kitamura and Kimura, 2012). The sandstone blocks in the Mugi mélange show localization along Riedel shear surfaces, possibly related to very low frequency earthquakes (VLFs) (Kimura et al., 2012). After brittle deformation nucleates in these so-called asperities, the elevated strain rates at the rupture tips may cause it to continue into normally aseismic regions (Fagereng and Sibson, 2010). Topographic highs, like calcareous seamounts, may act as mega-asperities. The high frictional strength in combination with observed velocity-weakening behaviour in chalk, could explain large subduction earthquakes (Ikari et al., 2013).

A major complication may be fluid pressures in the subduction zone. The subducting sediments contain water in pore spaces and in the form of hydrated minerals. These get trapped in the subduction interface shear zone due to a low permeability, causing near-lithostatic overpressures along the plate interface (Sibson, 2013). These fluid pressures may even change the seismic style (Fagereng and Ellis, 2009).

3 Geological setting

The Gwna Group, exposed on Anglesey Island and the Llŷn Peninsula, has become the type locality for mélange since Greenly first described it here (Greenly, 1919). The Gwna Group itself is part of the Mona Complex or the Monian Supergroup, which is interpreted as an imbricate stack, formed in a subduction zone setting.

3.1 Gondwanas margin

The Mona Complex formed between ∼600 (Asanuma et al., 2015) and ∼500 (Collins and Buchan, 2004) million years ago by imbrication of several units onto each other. This happened on the margin of supercontinent Gondwana, before several microcontinents started to break off. Many regard Avalonia the microcontinent on which the Mona Complex was formed (Kawai et al., 2006;

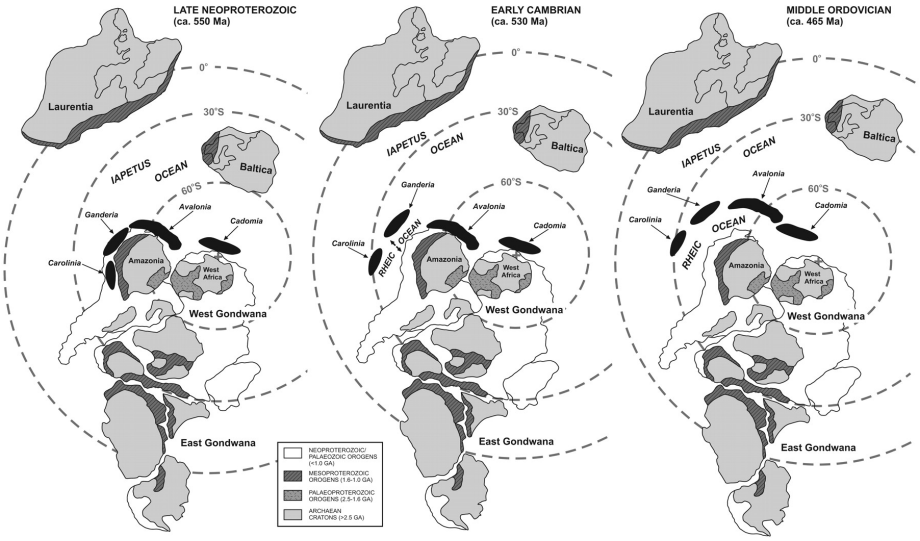

Figure 6: Plate reconstruction from Pollock et al. (2009), showing how several microcontinents, including Ganderia and Avalonia separated from Gondwana and moved north across the Iapetus Ocean. From Pollock et al. (2009)

Wood, 2012; Asanuma et al., 2015). However, Pollock et al. (2012) assume the Menai Strait Fault to be the terrane boundary between Ganderia and Avalonia, making Anglesey part of the microcontinent Ganderia (Fig.5). Detrital zircon data shows that both Ganderia and Avalonia were located on the Amazonian margin of Gondwana (Pollock et al., 2012), as was the Gwna Group on Anglesey (Asanuma et al., 2015).

These microcontinents were two out of several that separated from Gondwana by the opening of the Rheic Ocean (Fig.6). The reason for initiation of rifting in the Rheic Ocean is unclear but may involve slab rollback and the opening of a back-arc basin, ridge-trench collision or an inboard ridge jump (Pollock et al., 2009). Although the exact mechanism is uncertain, the separation of Ganderia occurred during Middle to Late Cambrian (509-485 Ma) and the separation of Avalonia occurred during Early Ordovician (485-470 Ma).

These microcontinents then moved north across the Iapetus Ocean, colliding with the Laurentian Continent in the Late Ordovician (457-444 Ma) and Early Devonian (419-393 Ma), based on evidence from the Appalachians (Pollock et al., 2012). Evidence from the English Lake District, based on age groups in detrital zircons and their provenance, shows collision of Ganderia occurred first with Baltica and slightly later with Laurentia in the Wenlock epoch (433-427 Ma) (Fig.7) (Waldron et al., 2014).

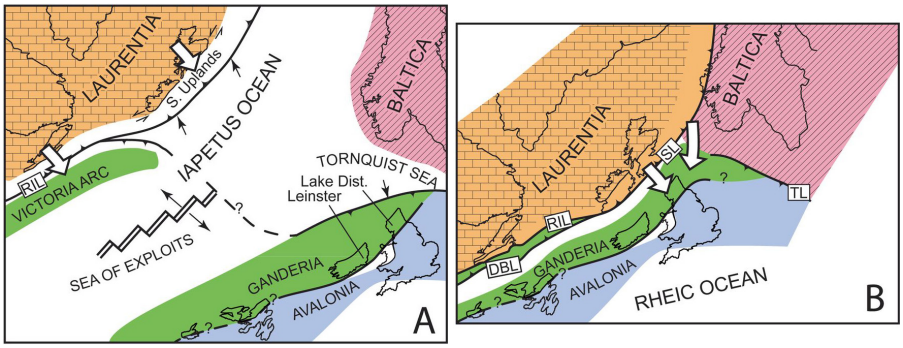

Figure 7: Reconstruction of microcontintents according to Waldron et al. (2014) for the (a) Late Ordovician (c. 450 Ma) and (b) Wenlock epoch (c. 430 Ma) showing that Ganderia, which included Anglesey, collided with Baltica first and then with Laurentia. From Waldron et al. (2014)

3.2 The rocks of the Mona Complex

The Mona Complex consists basically of three different groups, the Gwna Group, including a Blueschist Unit, the New Harbour Group and the South Stack Group. The groups of this imbricate stack, where new groups were added by underplating is described oldest to youngest, rather than based on their stratigraphic position, because the oldest is now at the stratigraphic top.

3.2.1 Coedana granites and gneisses

This complex with a leucogranite in quartzo-feldspatic gneisses with a metamorphic U-Pb zircon age of 666 ± 7Ma (Strachan et al., 2007) is considered the basement of the Mona Complex. The granite postdates the deformation of surrounding gneiss and has a U-Pb zircon age of 613 ± 4 Ma (Tucker and Pharoah, 1991). Suggestions for the origin of the Coedana granite include arc magmatism and melting of the crust due to the subduction of a mid-ocean ridge (Kawai et al., 2007). The origin of the gneisses is equally unknown, but suggestions are that they originated as a basement to the accretionary rocks, as a suspect terrane or that it is a klippe that was part of the (Avalonian) microcontinent (Kawai et al., 2007).

3.2.2 Gwna Group

Greenly (1919) characterized the Gwna Group rocks as "a chaotic assemblage of limestones, radiolarites, turbidites, and basalts, which may occur associated with peridotites, gabbros and blueschists (...) surrounded by a plastic rock matrix" (Wood, 2012). This chaotic character is used to distinguish this group from other rocks, although there are significant differences in the internal structure and composition of chaotic parts, as will become clear.

The Gwna Group is generally regarded as the oldest, first accreted group of the Mona Complex, although its position in the top of the sequence has been used to suggest this group is the youngest (Collins and Buchan, 2004). Absolute ages make it likely the Gwna Group is indeed the oldest, as strontium isotope data shows the age of carbonate megaclasts on the north coast of Anglesey is 860-800 Ma (Horák and Evans, 2011). Kawai et al. (2008) estimate ages of mudstone in the Gwna Group on Llanddwyn Island of 595-550 Ma. Alternatively, detrital zircon data show the Gwna mélange on the Llŷn Peninsula can be divided into two age groups, one with maximum depositional ages of 601 ± 6 Ma, the other with maximum depositional ages of 539 ± 19 Ma which were then incorporated in thrust duplexes and accreted (Asanuma et al., 2015).

- basalts The lowermost part of Gwna Group consists of pillow basalts, in places with red jasper in between the pillows. Thorpe (1993) describes these pillows on Anglesey as mid-ocean ridge basalts (MORB) although Saito et al. (2015) also report the presence of pillow basalts with a within plate basalt (WPB) or ocean island basalt (OIB) composition. Interestingly, the pillow basalts with WPB basalt composition are described to be overlain by the oxidized sediments, whereas the MORB pillow basalts are overlain by anoxic sediments (Saito et al., 2015). This correlates with the different age groups of Gwna Group described by Asanuma et al. (2015) with different ages of sedimentation for the anoxic (601 ± 6 Ma) and oxic (539 ± 19 Ma) sediments. Both these pillows with WPB composition and the two age groups of Gwna Group have been described on the Llŷn Peninsula, so it is uncertain how these are related to the pillow basalts in the current study areas on Anglesey Island.

- sediments On the northern coast of Anglesey (Cemaes Bay), different kinds of sediments are present in the mélange. These are mainly quartz and limestone, but also include (secondary) dolomite, ironstone, red chert, sandstone, phyllite and pillow lava (Wood, 2012). The extent of deformation makes the stratigraphic order unrecognisable. On Llandwyn Island and in the neighbouring Newborough Wood, the succession is preserved better. Here, the pillow basalts show a range of deformation stages, from very deformed to well-preserved. The interpillow spaces are filled with red jasper and carbonate and hyaloclastites are present. This is overlain by mafic mudstones, limestones, bedded cherts and turbiditic sediments (Maruyama et al., 2010).

This is different from the stratigraphic order on the Llŷn Peninsula as described by Sato et al. (2015), starting with dolostone, then a layer of black mudstone, followed by chert and mudstones with siliceous layers and a sandstone layer. This is again different from the stratigraphic relations described in Asanuma et al. (2015) at five different localities on the Llŷn Peninsula.

3.2.3 Blueschist Unit

This unit, of which the stratigraphic position is thought to be in between two different tectonostratigraphic parts of the Gwna Group, contains both greenschists

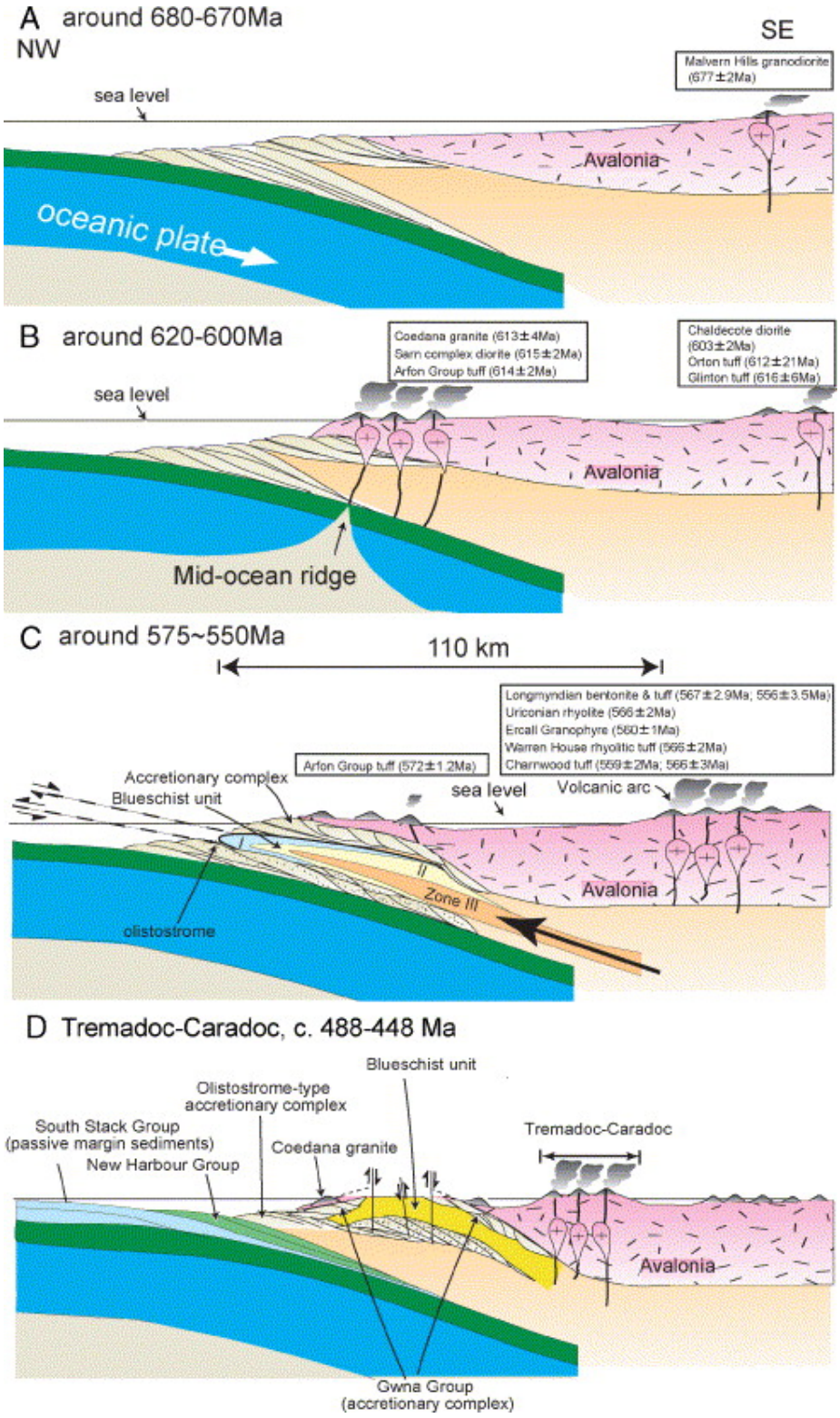

Figure 8: Tectonic model according to Kawai et al. (2007), with subduction of an oceanic plate underneath Avalonia. After subduction of a mid-oceanic ridge, there is extrusion of an isoclinally folded wedge of blueschist. After Kawai et al. (2007).

and blueschists that are remnants of pillow basalts. Thorpe (1993) showed these have MORB-type geochemistry, suggesting the blueschists may be similar to the Gwna Group schists, only of higher metamorphic grade (Kawai et al., 2006). Kawai et al. (2006) recognised three metamorphic zones, based on the occurrence of crossite and barroisite and suggested an isoclinal fold structure, with the highest metamorphic zone in the middle (Kawai et al., 2007).

Age constraints on this unit come from $^{40}Ar/^{39}Ar$ data, which are 560-550 Ma for phengite (Dallmeyer and Gibbons, 1987) and ca. 590-580 Ma for actinolite (Asanuma et al., 2015). The first is interpreted as the age of peak metamorphism, whereas the latter would be the time of formation of the protolith. This would mean this unit was formed at the same time, or in between the two stages of formation of the Gwna Group.

3.2.4 New Harbour Group

The rocks in this unit are deformed metabasalts, with olivine, plagioclase, pyroxene and oxides altered to greenschist assemblages (Thorpe, 1993), locally with red chert (Maruyama et al., 2010). The western part contains a band of serpentinite (Greenly, 1919). Thorpe (1993) showed the metabasalts of the New Harbour Group have chemical compositions of volcanic arc basalts and andesites. These are interpreted to have formed in a supra-subduction zone setting (SSZ) as "SSZ ophiolites have the geochemical characteristics of island arcs but the structure of oceanic crust" (Pearce et al., 1984). Although sometimes this group is referred to as the olistostromal New Harbour Group (Kawai et al., 2007; Saito et al., 2015). No absolute ages of this group are known.

3.2.5 South Stack Group

The South Stack Group consists of thick beds of quartzite, interbedded with thin mafic pelites (Maruyama et al., 2010), that formed as turbiditic sandstones, pelites and quartzites on a passive continental margin (Phillips, 1991). U/Pb dating of detrital zircons indicate that with youngest ages of 501 $\pm$ 10 Ma (Collins and Buchan, 2004), this is the youngest group in the sequence.

3.3 Tectonic model

Being the oldest of the sedimentary units, the Gwna Group was accreted first in the accretion-subduction complex. Asanuma et al. (2015) argue this was in two stages: the first at 620-600 Ma, the second at 575-500 Ma. The blueschists are thought to be isoclinally folded first, causing the highest metamorphic zone in the middle (section 3.2.3). This isoclinal fold structure is thought to be bounded by a normal fault on the top and thrust fault on the base, so that it intruded as a wedge into the Gwna Group. This would be very similar to blueschists in SW Japan.

The reason for extrusion of the blueschists is suggested to be a shallowing subduction angle due to the subduction of a mid-oceanic ridge (Kawai et al.,

2007). This would fit with the observation of Maruyama et al. (2010) that the age of the subducting plate must have been less than 10 Ma, based on the thickness of the accumulated sediments in the Gwna Group, which is c. 300m on Llandwyn Island (Maruyama et al., 2010). This is based on the assumption pre-Cambrian subduction zones can be compared with modern-day subduction zones. It is possible sediment accumulation rates were different in the pre-Cambrian and other differences may include warmer and more magnesium-rich sea-floors, of which the effect is unknown (Palin and White, 2016).

The mélange deformation or the formation of a mélange by deformation of pre-existing rocks, may have happened before, during or continued after the emplacement of the Blueschist Unit. After the formation of the Gwna Group and Blueschist Unit, the Mona Complex was completed by subsequent underplating of the New Harbour Group and the South Stack Group. This must be the sequence since ages show the South Stack Group is the youngest and the contact between the South Stack Group and the underlying New Harbour Group is a thrust plane (Barber and Max, 1979). The whole Mona Complex was cut by secondary high angle faults, disrupting the original subhorizontal structure, and is unconformably overlain by Ordovician sediments (Asanuma et al., 2015).

4 Methods

This research is based on thin sections of samples of the Gwna Group in Anglesey. These are collected on known locations of this subduction mélange rock assemblage. Since subduction mélanges consist of blocks in matrix, samples are taken of both the blocks and the matrix. When blocks with different lithologies were recognized, all of these were sampled. The matrix in between the blocks generally has more and less deformed parts, so I tried to sample the least deformed matrix and the most deformed matrix. However, very deformed rocks tend to fall apart and sometimes slightly less deformed samples had to be taken because samples must be coherent in order to preserve the deformation structures.

All thin sections are studied in great detail using a normal petrological microscope with magnifications up to x100 in plane polarized light (ppl) and crossed polarized light (xpl). This is needed to find deformation features like solution seams, foliations and twinning, undulose extinction, subgrains and recrystallized grains. Photomicrographs are taken and used for measurements like (sub)grainsize, thickness of veins and stylolites and aspect ratio of (sheared) vesicles.

After this, a selection is made for secondary electron microscope (SEM) studies. Samples are selected so that representative samples of each lithology are analyzed, as well as samples which contain minerals that are not easily identified using the petrological microscope because of their small grainsize. There is a special interest for samples containing chlorite and white mica, since chlorite geothermometry and white mica end-member compositions are to be analyzed.

An E-SEM (environmental-SEM) is used, operated under a vacuum of $\sim 1e^{-4}$ mbar with a beam current of 20 keV. A back-scatter electron (BSE) collector is used in combination with an energy-dispersive (EDS) detector in order to make spot analyzes of mineral composition. The samples are coated with a 5-10 nm thick layer of carbon in order to remove the excess surface charge. Therefore, the carbon detected by the EDS is removed from the data, the other measured elements are corrected to add up to a 100% total. Oxygen is not measured, but added according to stoichiometry after which compound percentages are calculated. This means that the measurements do not distinguish between different oxides of the same element, like FeO and Fe_2O_3 and tetrahedral Al(VI) and octahedral Al(IV). The amount of tetrahedral aluminium is calculated from assuming a perfect mineral structure in which all the tetrahedral sites that are not filled by silicium are filled with tetrahedral aluminium. All other aluminium has an octahedral configuration.

The measurement errors for the EDS-detector used with the E-SEM have not been quantified, but are typically $<<10\%$ relative, often $<5\%$ relative, depending on concentration (D. Muir, personal communication, February 16, 2017). This means internal sample compositional variation is often higher than measurement errors. A problem with measuring elemental composition from spot-size analyses, is that the (spherical) interaction volume of the beam might be larger than a single mineral, especially if minerals are small or platy. The measurement then gives a spectrum for the whole interaction volume, including minerals around the crystal that was aimed for, which 'contaminates' the measurement. Another limitation in the use of spot-size analyses is that there is no quantification of how much of a mineral is present in a rock, apart from a first estimate by the eye. Also, it is possible that minerals that are present only in small amounts, have been overlooked. However, the advantage of spot-size analyses is the limited time needed per analysis, which means the amount of analyses that can be performed is high. This makes it suitable to quickly obtain information on the main mineral phases present. Exact quantification of mineral amounts and accessory minerals do not have a large influence on rock strength and deformation behaviour, which makes the spot-size analyses suitable for the needs of this research.

4.1 White mica

For white mica, the number of ions per formula unit (p.f.u.) is calculated based on 11 oxygen, the relative amounts of silicium, aluminium and M+ (iron, magnesium and titanium) are calculated by adding their amounts p.f.u. and are given as a percentage of this total. It does not make a difference whether this aluminium is occupying octahedral or tetrahedral sites. Number of ions p.f.u. and not weight percentages are used because the number of ion substitutions in the structure are important. This is because the white mica muscovite ($KAl_2AlSi_3O_{10}(OH)_2$) usually contains some phengite ($K\ (AlMg)_2(AlSi)_4O_{10}(OH)_2$), where magnesium (or iron) replaces octahedral aluminium and at the same time silica is substituted for tetrahedral aluminium to balance the charge. This is im-

portant because an increase in phengite content (i.e. increase in magnesium, iron and silicium) indicates formation at higher metamorphic pressures (Guidotti et al., 2000), indicating formation at depth in a subduction zone rather than by seafloor alteration.

4.2 Chlorite geothermometry

For chlorite ($(Mg,Fe,Mn,Al)_{12}[(Si,Al)_8O_{20}](OH)_{16}$), the number of ions is calculated based on 28 oxygen. Chlorite geothermometry is based on the principle that at higher temperatures, aluminium substitutes for silicium in the tetrahedral sites. Cathelineau (1988) found a linear correlation between the amount of tetrahedral aluminium [Al(VI)] and temperature T: $T(°C) = -61.92 + 321.98 * [Al(IV)]$, with an uncertainty of ± 25°C.

Jiang et al. (1994) found this relationship breaks down when there is too much calcium, sodium or potassium present in the chlorite, possibly because this means the chlorite is contaminated by a second phase like muscovite or illite. This is why measurements where the amount of [Ca + Na + K] p.f.u. is higher than 0.20 are discarded. It is also possible a measurement is contaminated by iron oxides present in the sample, which would result in higher amounts of iron and possibly titanium and a decrease in all other elements. Unlike muscovite and illite, the bright iron oxides are easily distinguished from chlorite in the SEM and could therefore be avoided in the measurements.

Zang and Fyfe (1995) found that the iron content in chlorite X_{Fe} ($Fe/(Fe+Mg)$) influences the amount of tetrahedral aluminium. Therefore, if high amounts (generally accepted >0.50 p.f.u.) of iron are present in chlorite, a correction to the earlier geothermometer should be used. This produced the following relationship: $T(°C) = 17.5 + 106.2 * ([Al(IV)] - 0.88 * (X_{Fe} - 0.34))$. When iron content is low, but magnesium content is high, the method by Kranidiotis and MacLean (1987) must be preferred. This relationship: $T(°C) = 19 + 106 * ([Al(IV)] + 0.7X_{Fe})$ corrects for the fact that chlorite might be undersaturated in aluminium.

All three of these geothermometers are used to calculate paleotemperature, after which based on magnesium content and iron number the decision is made which temperature is most reliable. However, this decision is not always straightforward and the three geothermometers can yield significantly different temperatures, which reduces the reliability of chlorite geothermometry in general. de Caritat et al. (1993) stress that chlorite geothermometry depends on many natural variables and should therefore only be used in combination with other methods of estimating paleotemperature. In this research it is used in combination with temperature estimates from deformation mechanisms that were active.

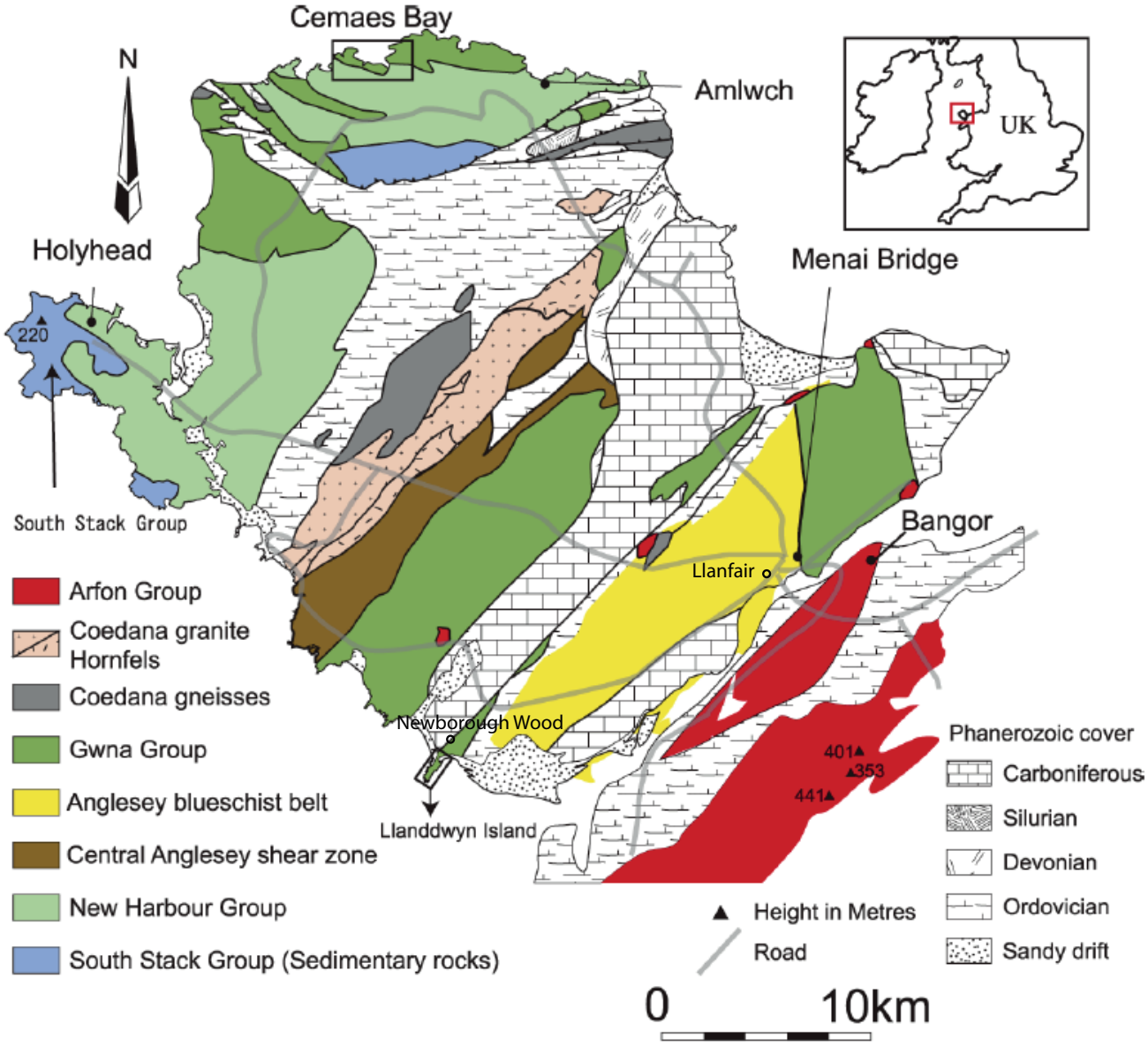

Figure 9: Geological map of the area (From Wood (2012)) showing the sample location in Newborough Wood, also showing the locations of the geological map of Llandwyn Island (Fig.10) and the geological map of Cemaes Bay (Fig.11)

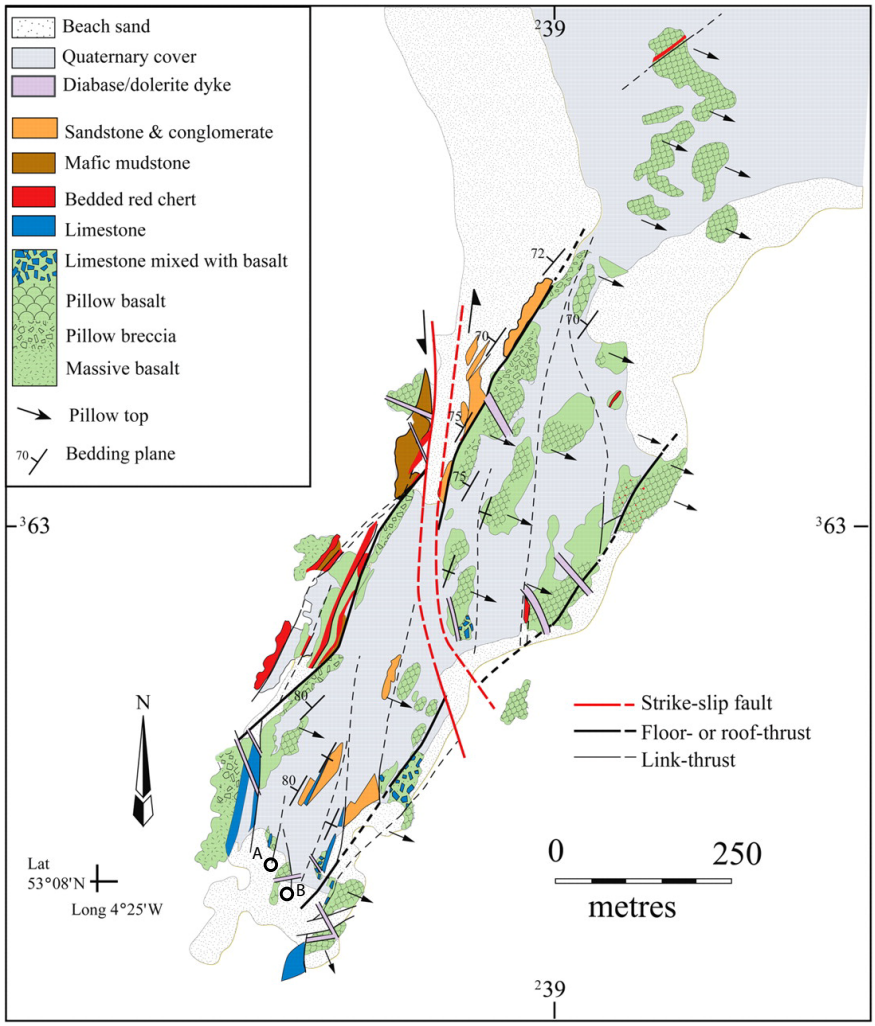

Figure 10: Geological map of Llandwyn Island (From Maruyama et al. (2010)) with sample localities A and B. For location see Fig.9

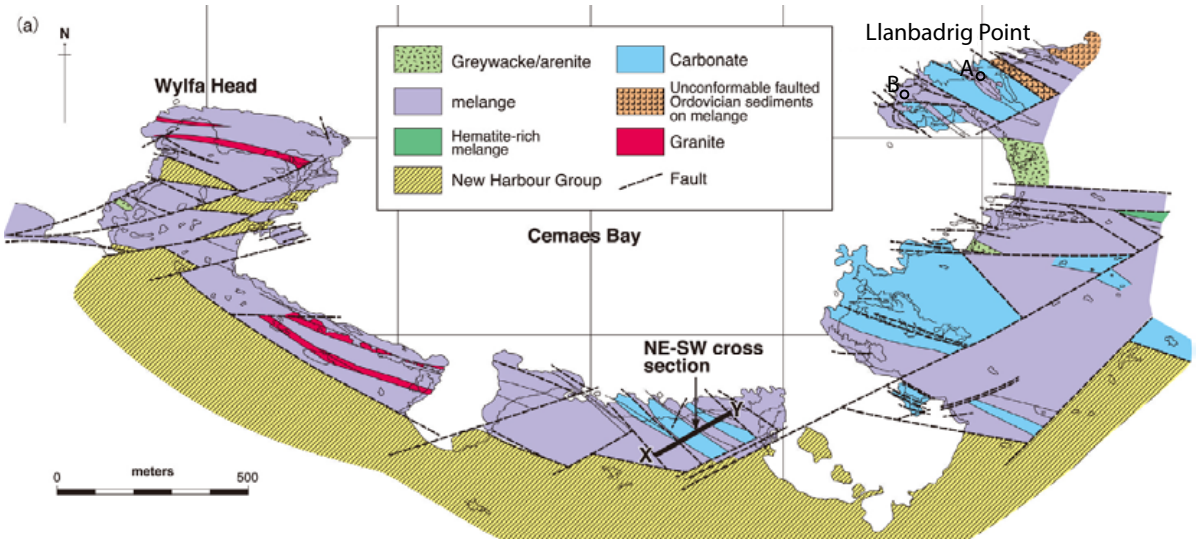

Figure 11: Geological map of Cemaes Bay (From Wood (2012)) with sample locations A and B. For location see Fig.9

5 Results

This section will start with a description of the locations and rocks in outcrops, after which it will be continued with a detailed description of each thin section studied, followed by EDS analyses of white mica and chlorite. An overview of the samples and thin sections studied is given in table 1, the locations where these were taken are shown in Figures 9, 10 and 11.

Observations will be separated by study area, because they are thought to come from different stratigraphic levels. The rocks from Llandwyn Island are interpreted as the lower part of the ocean plate stratigraphy, because they include basalts. The rocks from Cemaes Bay are thought to be the upper part of the sequence, as they do not contain basalts but do contain quartzite layers and stromatolitic limestones (see section 3.2.2).

5.1 Field observations

5.1.1 Llandwyn Island

At Llandwyn Island, the mélange consists of juxtaposed slices of different lithologies. These blocks include mainly basalts (Fig.12b), but also sediments (Fig.12d) and hyaloclastites (Fig.12c). There is no clear matrix surrounding these blocks, but the boundaries are highly deformed. In places where the basalts are less deformed the original pillow shape is recognizable (Fig.12e).

Included in this section is a sediment from Newborough Wood, which was not deformed in the mélange and therefore gives a better overview of the general

Figure 12: outcrops on Llandwyn Island, with a) alternating red and green chert layers, interbedded with dark clay-rich layers (AN16-022), b) elongated basalt pillows surrounded by carbonates (AN16-025), contact with the sediment is a highly deformed layer (white arrow) c), hyaloclastite in which the basaltic lenses have a clear elongation direction (black arrow) (AN16-026), d) deformed red mudstone that is located in between the hyaloclastite and elongated pillows (AN16-027), e) where the basalt is less deformed, the pillow shape is clear (AN16-028 is from similar shaped pillows)

Figure 13: outcrop at Cemaes Bay A, with a) overview of the location where samples AN16-004 - AN16-007 were taken, b) elongated dolomitic block (orange) cross-cut by veins, c) highly deformed layer at the boundary of the large dolomitic block (white arrow), d) there are many small blocks in the matrix

Figure 14: outcrop at Cemaes Bay B, with a) elongated quartz boudins, and b) small quartz blocks in the matrix

regional deformation events. This is an alternation of red and green chert layers with clay-rich layers, of which sample AN16-022 is an example. These are folded into upright folds, of which the hinges are collapsed, indicating the sediment was not fully consolidated when it was folded (Fig.12a).

Combining observations from Llandwyn Island and Newborough Wood, the stratigraphic sequence becomes clear, starting with the pillow basalts with red jasper and carbonate in the interpillow spaces. This is overlain by the red and green bedded chert described above. On top of this are layers of sandstone, followed by a brecciated limestone.

5.1.2 Cemaes Bay

Compared to Llandwyn Island, the mélange at Cemaes Bay has a more typical block-in-matrix structure, with blocks of dolomite, limestone and quartz. There were two sample locations in Cemaes Bay, approximately 200 meters apart, with different lithologies. This causes differences in deformation mechanisms and therefore these two areas will be treated separately.

What is called location A (Fig.11) contains carbonate blocks in a fine grained matrix (Fig.13a,b). The matrix of the mélange showed more deformed parts close to the blocks and less deformed parts further away from the blocks (Fig.13c). Samples from this location include two carbonate blocks, one orange in outcrop which did not react with HCl and is dolomitic, the other is gray in outcrop and did react with HCl and consists mainly of calcite. Some parts of the mélange matrix included many small blocks (Fig.13d).

At location B there is a similar block-in-matrix structure, but the blocks contain quartz instead of carbonates and the mélange matrix itself is also very rich in quartz (Fig.14). In order of increasing matrix content the samples taken here are: sample AN16-012 comes from a quartzite block and therefore consists

of almost pure quartz, sample AN16-011 is a quartz rich part of the mélange matrix and consists mainly of a quartz block with one really deformed layer. Sample AN16-009 comes from a quartz boudin and includes some matrix and sample AN16-008 is a part of the mélange matrix with many quartz blocks. In between the quartz blocks and matrix there was one thin layer that mainly caught attention because it looked red, although fresh surface revealed it was a gray very fine grained rock. In the outcrop it looked as if this was a very deformed layer in the matrix (AN16-010). An overview of the samples is given in table 1.

5.2 Microstructural observations

5.2.1 Llandwyn Island

basalts As can be seen in table 1, two basalt samples were taken at Llandwyn Island, AN16-025 and AN16-028. Their sample locations are approximately 50 meters away from each other (Fig.9 and Fig.10) and no major discontinuities were observed, so that the differences can be linked to the amount of deformation and not metamorphic grade. From the outcrops (section 5.1.1, Fig.12), it could be seen that sample AN16-025 was more elongated and therefore more deformed than sample AN16-028. The thin section of sample AN16-028 shows signs of alteration, the minerals are altered to mainly albite and muscovite, with minor apatite and iron and titanium oxides. The crystals have random orientations and there are vesicles present that have retained their original rounded shape (Fig.15a-c). This in contrast to sample AN16-025 where the muscovite crystals are aligned in two directions at an angle of about 40° relative to each other (Fig.16a,b).

Both basalt samples have carbonate and quartz veins. In the less deformed AN16-028, this is one rounded blob of calcite, of which the contacts with the basalt are lined by quartz. There are also veins, in which more quartz is present. The carbonate in this sample shows twinning and subgrains, grain boundaries are irregular. The quartz is very fine grained, but does not show signs of deformation like undulose extinction, and grain boundaries are straight (Fig.15d-f).

The carbonate in sample AN16-025 is present as elongated bands and has in general a more chaotic appearance. Relative to sample AN16-028, there are less subgrains, but twinning is more pronounced. In one area, there are smaller interlocking partly dolomitized grains (0.37 Mg p.f.u.) that do not show undulose extinction, but have very closely spaced twins and cleavage. Most twins are smaller than one μm, the thickest are several μm (Fig.16c). This is in contrast to the twins in the calcite in the sample, which are around 20 μm thick and irregular in shape (Fig.16d,e). Again quartz is present, but in this case it does not simply line the boundary between the carbonate and the basalt any more. Instead, it forms semi-circular aggregates on the boundary (Fig.16f).

sediments There are two samples of sediments (Tab.1), one taken at Llandwyn Island (AN16-027, Fig.10) and one taken in Newborough Wood (AN16-022,

Table 1: overview of the samples taken and their locations

Sample number	Sampling location	GPS coordinates (lat (N); long (W))	Sample description	mineral assemblage*
AN16-004	Cemaes Bay A	53.42359; 4.44710	most deformed mélange matrix	
AN16-005	Cemaes Bay A	53.42359; 4.44710	least deformed mélange matrix	*Ap, FeO, Qtz, Rt, Wmca, Zrn*
AN16-006	Cemaes Bay A	53.42359; 4.44710	mélange matrix including small blocks	*Ap, Chl?, FeO, Qtz, Rt, Wmca*
AN16-007	Cemaes Bay A	53.42359; 4.44710	carbonate block in mélange	Dol
AN16-008	Cemaes Bay B	53.42303; 4.44998	mélange matrix	*Ap, FeO, Qtz, Wmca, Zrn*
AN16-009	Cemaes Bay B	53.42303; 4.44998	quartz block in mélange	Qtz + Wmca
AN16-010	Cemaes Bay B	53.42303; 4.44998	fine grained mélange matrix	*Ap, FeO, Kln, Qtz, Rt, Wmca, Zrn*
AN16-011	Cemaes Bay B	53.42303; 4.44998	mélange matrix	*FeO, Mnz, Py, Qtz, Wmca*
AN16-012	Cemaes Bay B	53.42303; 4.44998	quartzite block in mélange	Qtz + Wmca
AN16-013	Cemaes Bay A	53.42359; 4.4471	elongated carbonate block in mélange	Cal
AN16-022	Newborough Wood	53.15078; 4.40026	siliceous mudstone with soft sediment deformation	*Ab, Ap, Cal (veins), Chl, FeO**, Qtz, Rt, Wmca*
AN16-025	Llandwyn Island A	53.13437; 4.41418	elongated pillow basalt in dolostone	*Ab, Ap, Cal, Chl, Dol, FeO**, Qtz, Rt, Wmca*
AN16-026	Llandwyn Island A	53.13437; 4.41418	deformed hyaloclastite	*Ap, Cal, Chl, Dol, Qtz, Rt, Wmca*
AN16-027	Llandwyn Island A	53.13437; 4.41418	deformed schistose mudstone	*Ab,Ap, Chl, FeO, Qtz, Rt, Wmca*
AN16-028	Llandwyn Island B	53.13474; 4.41457	greenish pillow basalt in less deformed lens	*Ab, Cal (veins), Chl, FeO, Qtz, Rt, Spl, Wmca*

*Based on optical studies of thin sections, italics mean confirmed by SEM measurements (Ab=Albite, Ap=Apatite, Cal=Calcite, Chl=Chlorite, Dol=Dolomite, Kln=kaolinite, Mnz=monazite, Py=pyrite, Qtz=Quartz, Rt=Rutile, Spl=spinel, Wmca=white mica, Zrn=zircon)
**ratio between Fe and O cannot be measured, therefore it is unknown what the iron oxide mineral is

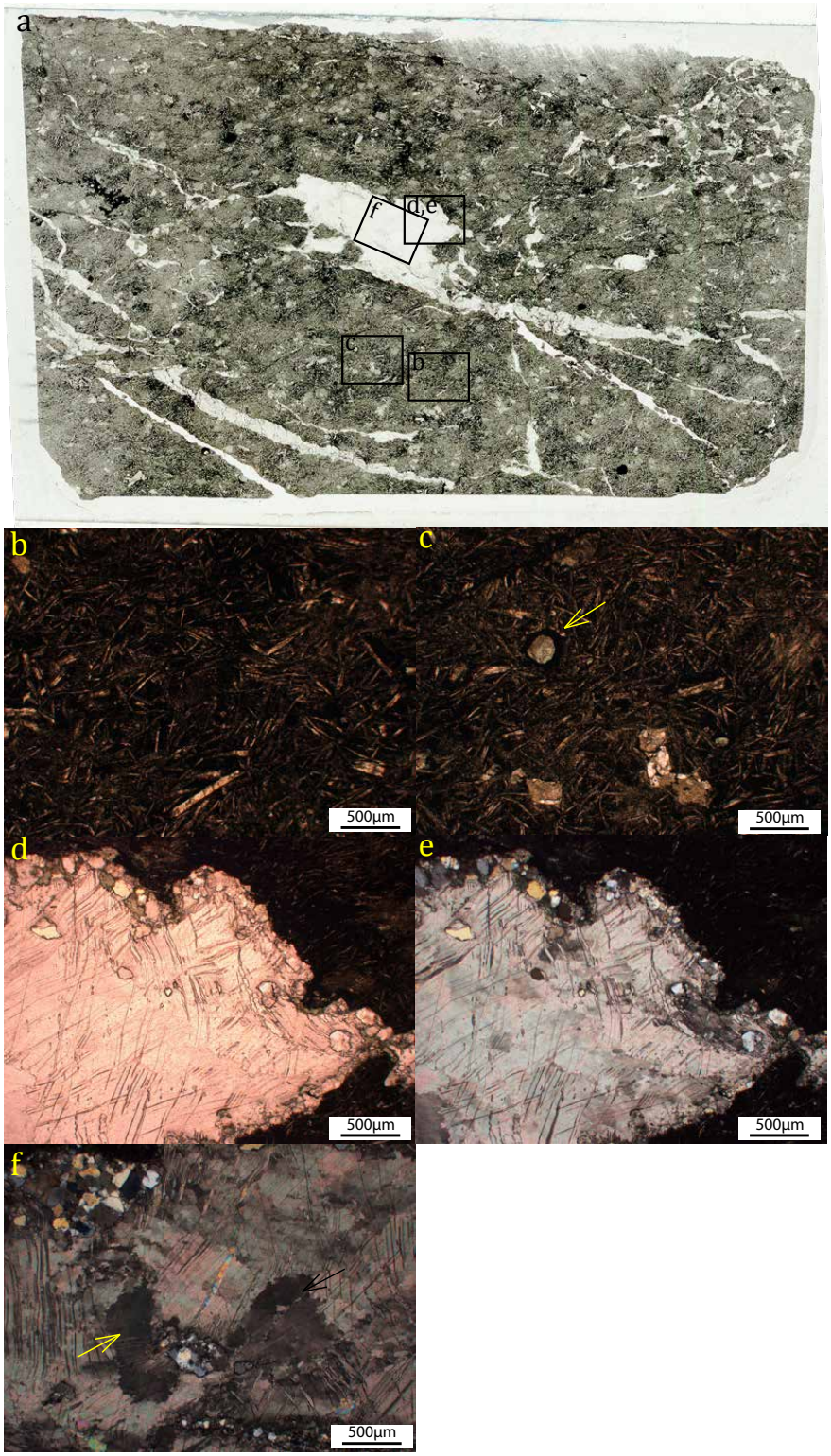

Figure 15: Photomicrographs of thin section AN16-028, the relatively undeformed basalt, with a) an overview of the sample, also showing where in the sample figures b-f come from, b) there is no clear crystal alignment, c) vesicles filled with chlorite, d) a quartz layer is present on the boundary between the basalt and the calcite in plane polarized light and e) in crossed polarized light, f) relatively strain-free crystals are present in the middle of the calcite

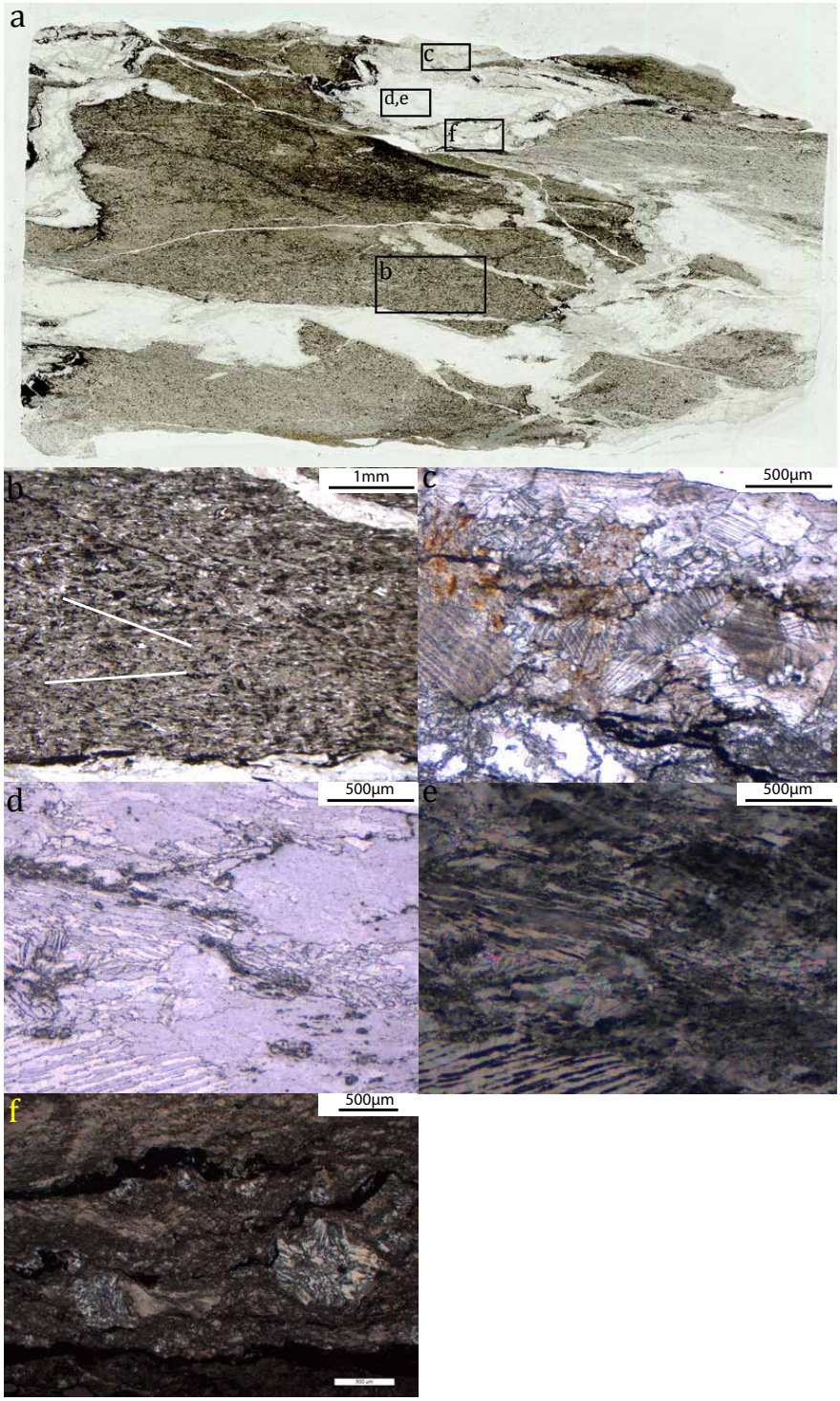

Figure 16: Photomicrographs of thin section AN16-025, the deformed basalt, with a) an overview of the sample, also showing where in the sample figures b-f come from, b) there are two directions of alignment, c) one cluster of crystals shows many thin twins, d) calcite crystals show many thick twins and recrystallization in plane polarized light and e) in crossed polarized light, f) quartz forms circular aggregates near the boundary of the calcite with the basalt (xpl)

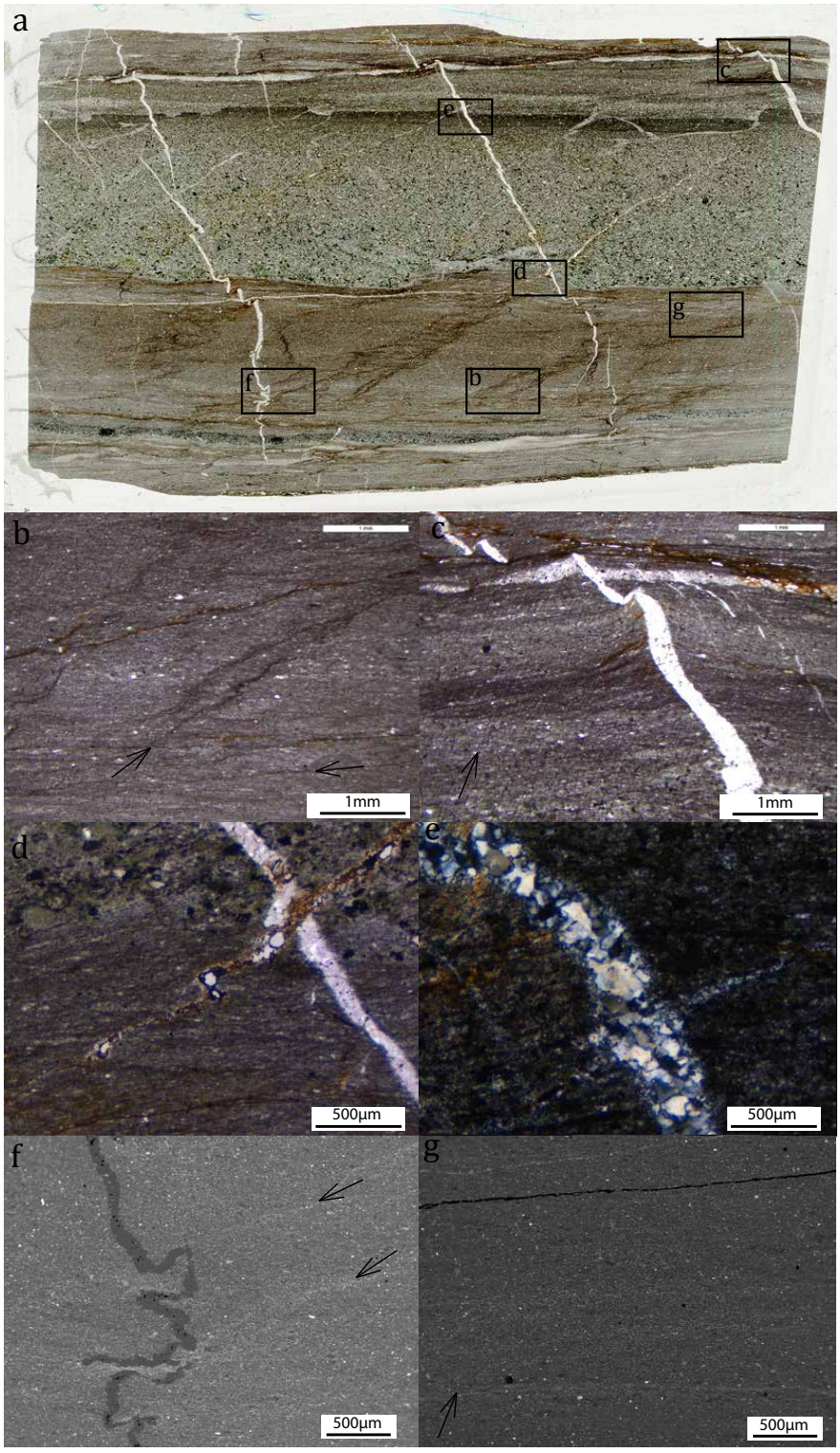

Figure 17: Photomicrographs of thin section AN16-022, the deformed sediment from Newborough Forest, with a) an overview of the sample, also showing where in the sample figures b-e come from, b) pressure solution seams in two directions, c) the quartz veins are offset by the pressure solution seams, also note the clear inclined foliation in the left bottom part of the sample, d) the inclined pressure solution seam continues as a crack filled with a brown mineral, e) quartz grain in veins have irregular grain boundaries and show small amounts of undulose extinction (xpl), f) BSE image showing the light-coloured solution seams are enriched in muscovite and oxide minerals, cross-cutting the dark quartz vein, g) BSE image showing no compositional variation defines the spaced foliation that should be present in the direction of the arrow

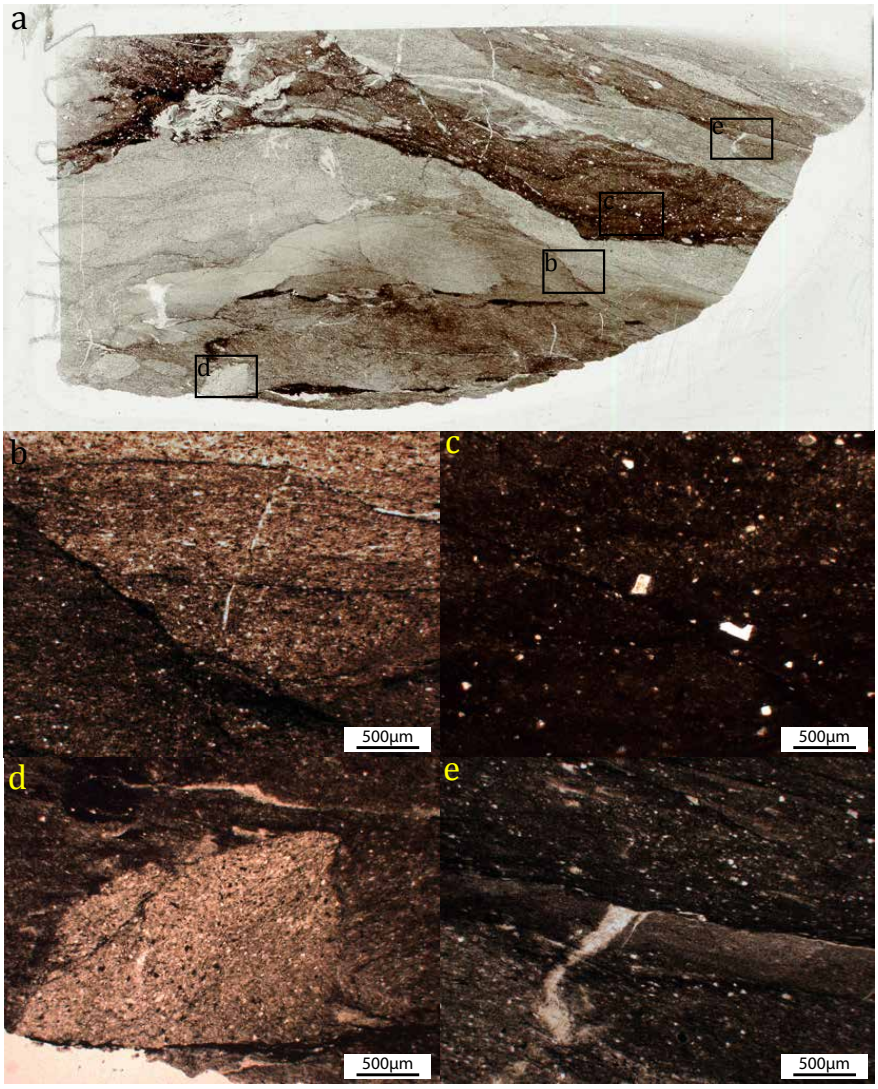

Figure 18: Photomicrographs of thin section AN16-027, the deformed sediment, with a) an overview of the sample, also showing where in the sample figures b-e come from, b) pressure solution seams are also present in the coarser grained layers, c) in the very dark parts only some coarse quartz grains are left, some rounded and some angular, d) one of the three coarse-grained blocks that do not have the same crystal alignment as the rest of the sample, e) veins terminate on solution seams

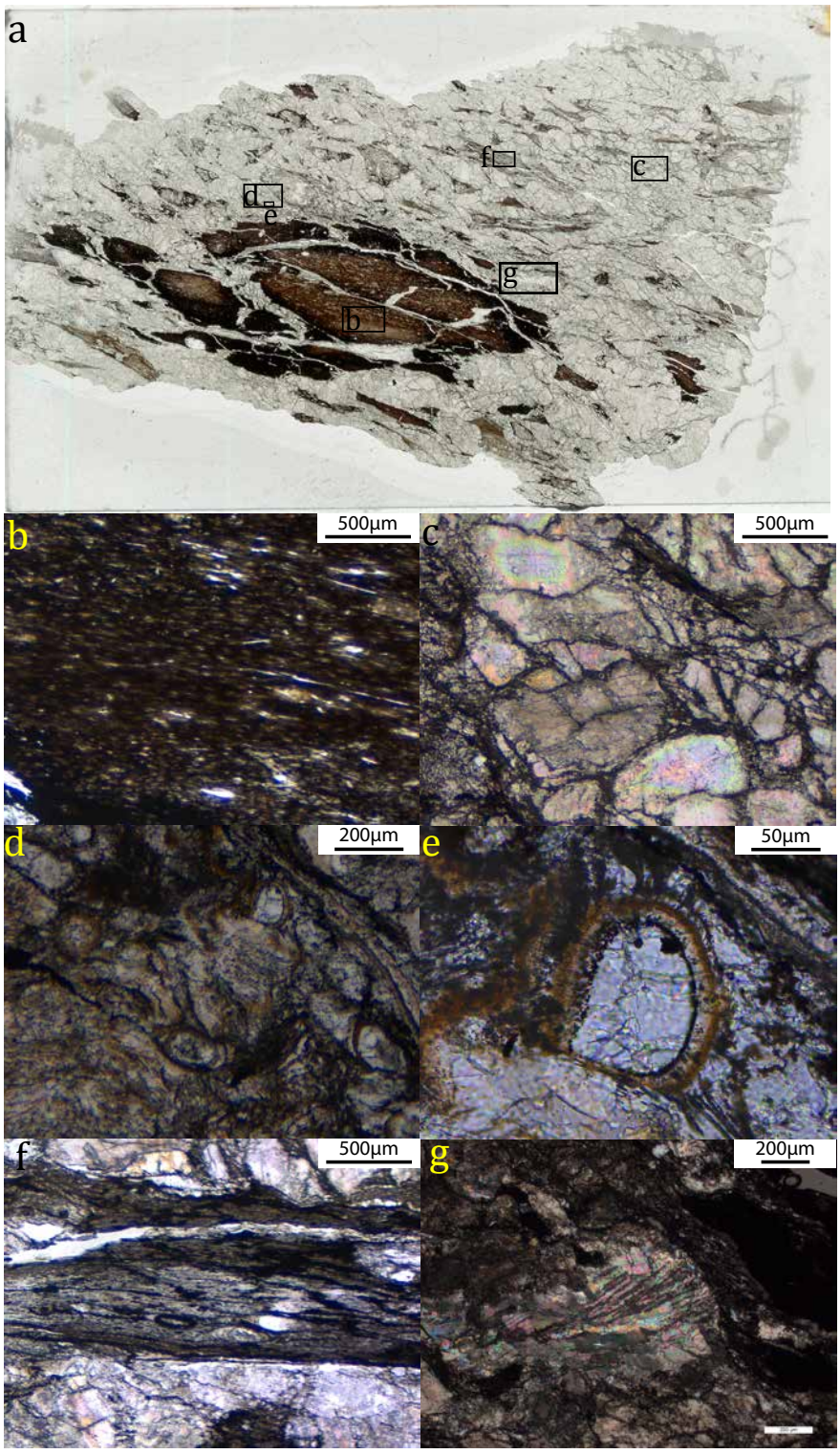

Figure 19: Photomicrographs of thin section AN16-026, the hyaloclastite, with a) an overview of the sample, also showing where in the sample figures b-g come from, b) the basalt does still show a preferred alignment, c) there is a dark mineral present at the grain boundaries , d) there are vesicles, filled with carbonate, e) some of these vesicles show a clear rim , f) in other places, further away from the basalt the vesicles are stretched, and g) some crystals do show twinning (xpl)

Fig.9). This last one contains mostly very fine grained material, but includes a coarser grained layer, which is fining upwards, and lenses of coarser and finer grained material. Minerals, although too fine grained to be identified, have a preferred orientation subparallel to this layering defined by grainsize variations. A faint spaced foliation has also developed, at an angle of 60° to the sedimentary layering (Fig.17 a,c). Back-scatter electron images show there is no compositional variation that defines this foliation (Fig.17g).

Parallel to the primary layering, dark solution seams are visible, indicating pressure solution operated in this rock. More solution seams are present at an angle of about 30° to the primary layering. These are only visible in the finer grained layer, but continue into the coarser grained layer as a small crack, lined with a brown mineral (Fig.17 b,d). The solution seams are enriched in muscovite and oxide minerals (Fig.17f). The quartz veins vary in orientation from perpendicular to these layer-oblique solution seams to perpendicular to the stratigraphic layering. The layer-parallel solution seams offset the quartz veins. The grains in the quartz veins show a range in grainsize (∼15-250μm), and contain undulose extinction and in places also subgrains (Fig.17 c,e).

The thin section of the sediment slice (AN16-027) in between the basalt and the hyaloclastite reveals the original sedimentary layering in the form of a coarser grained band and there is again some mineral alignment. There are many signs of pressure solution in the form of solution seams, mostly parallel to the bedding. In places this causes almost opaque bands, with a few large (∼150μm) crystals remaining, of which some are really rounded and some are very angular (Fig.18 a-c). The solution seams are not restricted to the finer grained layers, although they are more pronounced there.

A few areas show localized quartz, but these are not through-going veins and do not have a consistent orientation. The quartz has a very fine grain size and some larger grains again show undulose extinction and some subgrains. Some of the quartz veins stop at solution seams. There are three blocks with coarser grainsize that do not form a layer. These blocks have diameters of 2.1, 1.8 and 1.3 mm and have aspect ratio's of 1.31, 1.91 and 3.60. The solution seams do not continue into these blocks, but also do not appear to curve around them (Fig.18 d,e).

hyaloclastite The hyaloclastite (AN16-026) shows deformation in the form of elongated lenses of basalt in a green carbonate matrix, which is visible both in the outcrop and in thin section (Fig.19a). This carbonate matrix is partly dolomitized, with magnesium content varying between 0.34 Mg p.f.u. and 0.48 Mg p.f.u. The dolomite grains do not show any deformation twins, with the exception of two grains, that may be less dolomitized. Grain boundaries are relatively straight, although in most places there is a dark second phase present, making the grain boundaries appear as thick lines (Fig.19c).

There are vesicles in the matrix, now filled in with calcite, chlorite and muscovite. Close to the basalt these vesicles still have their original roundish shape, average over three measurements gives a diameter of 107 μm and aspect

ratio of 1.41. In the more sheared matrix, vesicles are elongate, with average over three measurements gives a diameter of 137 μm and aspect ratio of 3.71(Fig.19d-f). The dark colour of the basalt makes it seem more altered than the other samples, especially around the edges of the lens the minerals are opaque. Where individual muscovite crystals can be identified, these are aligned (Fig.19b).

5.2.2 Cemaes Bay - A

carbonate blocks There are two samples of carbonate blocks, one dolomitic (AN16-007) and one elongated, less dolomitized block (AN16-013). The dolomitic block shows large variations in grainsize, the coarser of which are found within veins. These mostly have a vertical orientation, if the stylolites are considered horizontal (Fig.20a,d). In this sample there are two types of stylolites, one of which are very fine (<20 μm) linear seams. Single seams are not continuous, but together they define a foliation throughout different parts of the sample (Fig.20b). They are not present in the parts with large grains and they are cross-cut by the veins. The other type are thicker (>50 μm), irregular stylolites, that cut across the whole sample, including the coarse grained bands (Fig.20c). The veins are 100μm to 2mm in width with large grains up to 300μm. Individual crystals have a brown staining which is typical for dolomite (Fig.20e), but do not contain any twins.

The other carbonate block, with more calcite (AN16-013) looked elongated in the outcrop. There are dark seams that resemble the irregular stylolites from sample AN16-007, but they are less pronounced and more diffuse (Fig.21a,b). They do not all have similar orientations, but may indicate there was compaction in at least two directions. There are more gaps and cracks along these stylolite seams. This sample does not have the fine linear seams that are present in AN16-007, but there are similar veins (Fig.21c). These veins are less wide (1-100μm) and do not have coarser grains than the surrounding material. They do not have a clear preferred direction, but occur in many orientations. Most of them are cross-cut by the stylolites, although one vein cross-cuts the whole sample. It contains mostly large calcite grains, in certain areas these are very clear and contain many twins. These vary in width and spacing from submicrometer width to 30-40μm and some crystals contain up to three twinning directions (Fig.21d,e). In other areas the calcite is very fine grained, possibly also forming dolomite.

mélange matrix Unlike the blocks in the mélange, the matrix does not contain any carbonates. Instead it is a network of fine grained muscovite, with quartz-rich parts and minor amounts of iron and titanium oxides, apatite and zircon (Fig.22f). Similar to the samples from Llandwyn Island, the sample (AN16-005) that looked like it was least deformed in the field shows the most deformation features in thin section. There are no clear sedimentary layers, but there are coarser lenses present (Fig.22a,b). There are solution seams parallel to these lenses and there is a spaced foliation at an angle of about 35° to

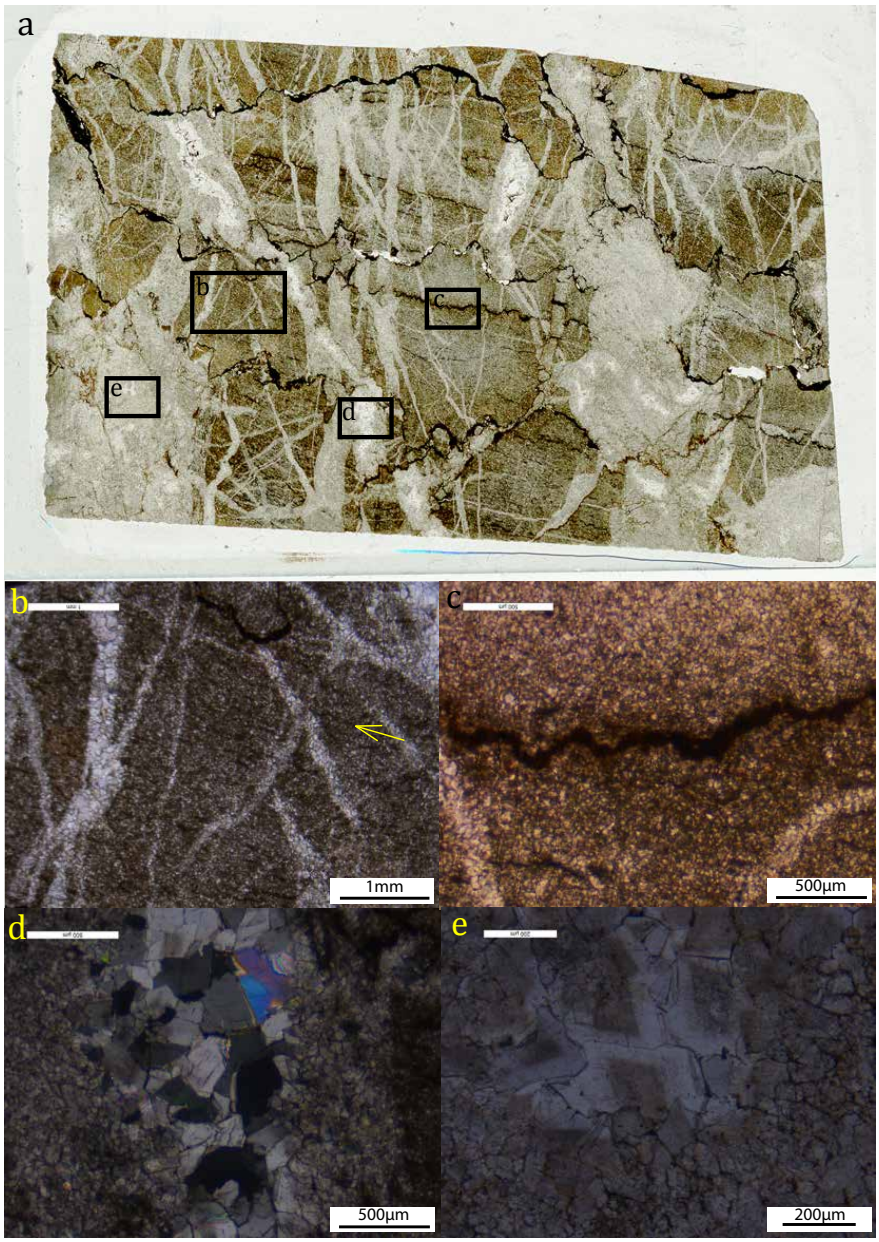

Figure 20: Photomicrographs of thin section AN16-007, the dolomitized block, with a) an overview of the sample, also showing where in the sample figures b-e come from, b) thin solution seams are aligned in the direction of the arrow but not continuous, c) thick irregular stylolites, d) the larger interlocking grains in the veins (xpl), e) these grains have staining typical of dolomite

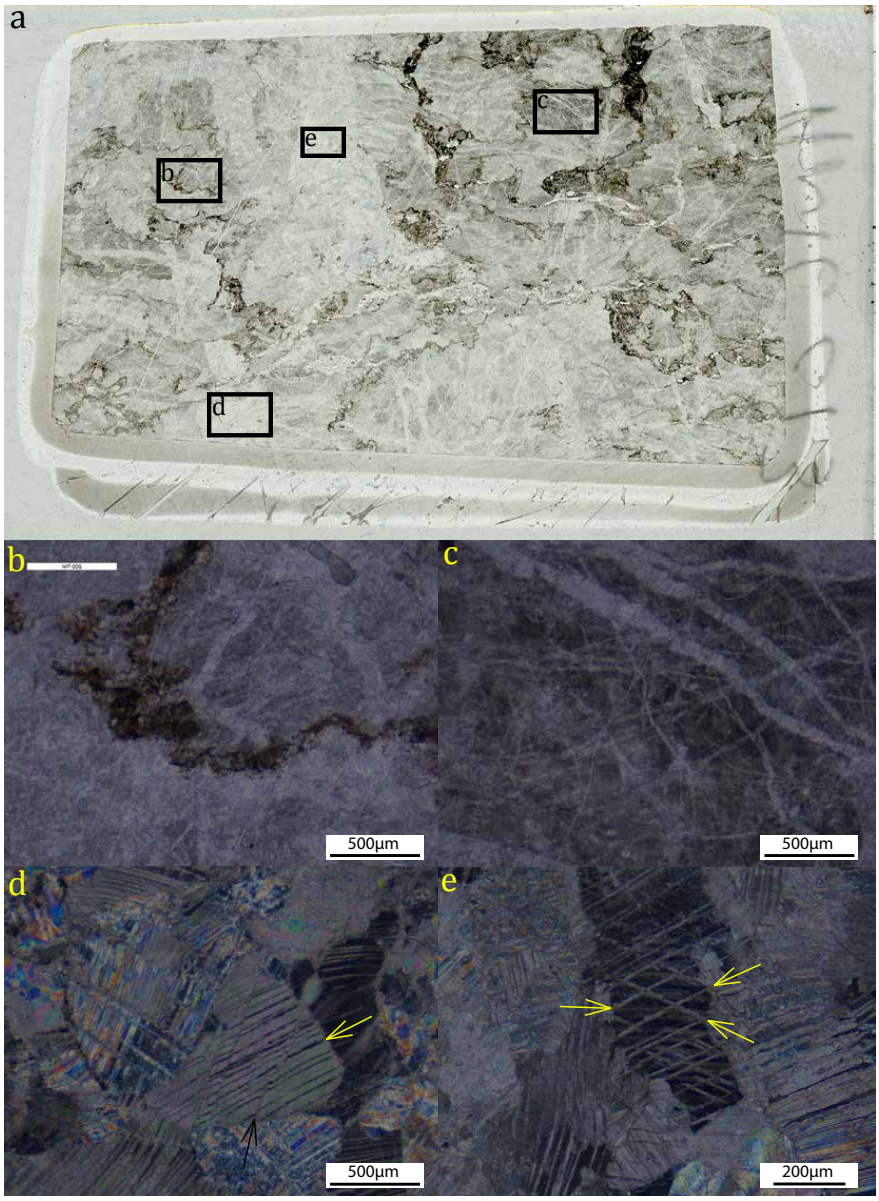

Figure 21: Photomicrographs of thin section AN16-013, the calcite block, with a) an overview of the sample, also showing where in the sample figures b-e come from, b) irregular stylolite surface, c) veins in many directions, d) thin twins (black arrow) that offset thick twins (yellow arrow) in the middle crystal (xpl), e) three twinning directions in a single crystal (xpl)

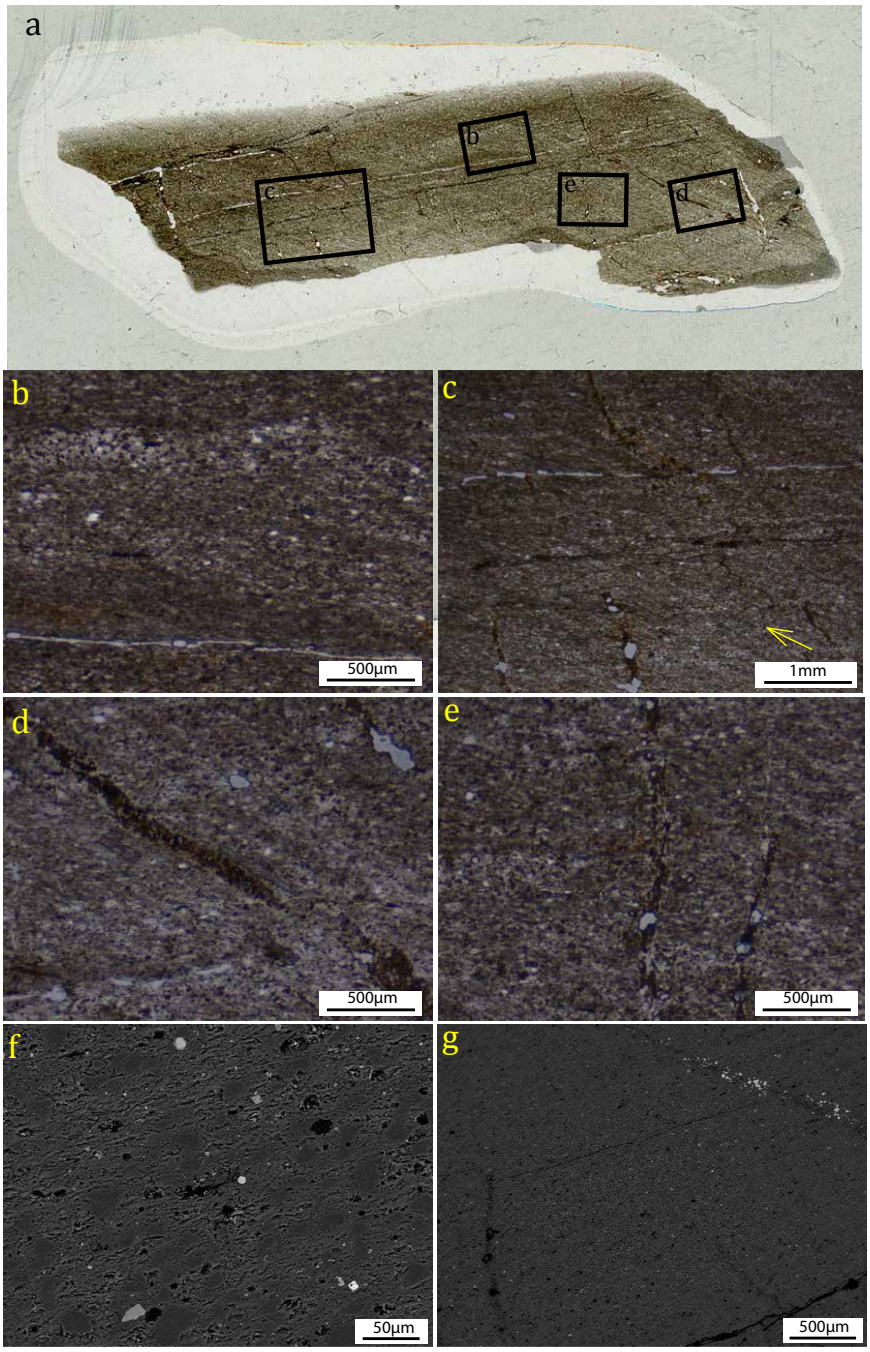

Figure 22: Photomicrographs of thin section AN16-005, the least deformed mélange matrix at Cemaes A, with a) an overview of the sample, also showing where in the sample figures b-e come from, b) quartz rich/coarser grained lenses parallel to the cracks and solution seams, c) a spaced foliation (direction of the arrow) at an angle of 35° to the sedimentary and pressure solution foliation, d) veins with a brown mineral follow the spaced foliation, e) veins with a brown mineral are perpendicular to the main sedimentary and pressure solution foliation, f) small dark grey quartz grains in a network of grey muscovite, with minor apatite and oxides (light gray and white) (BSE image), g) the spaced foliation in direction of the top right-hand vein is not visible in this BSE image

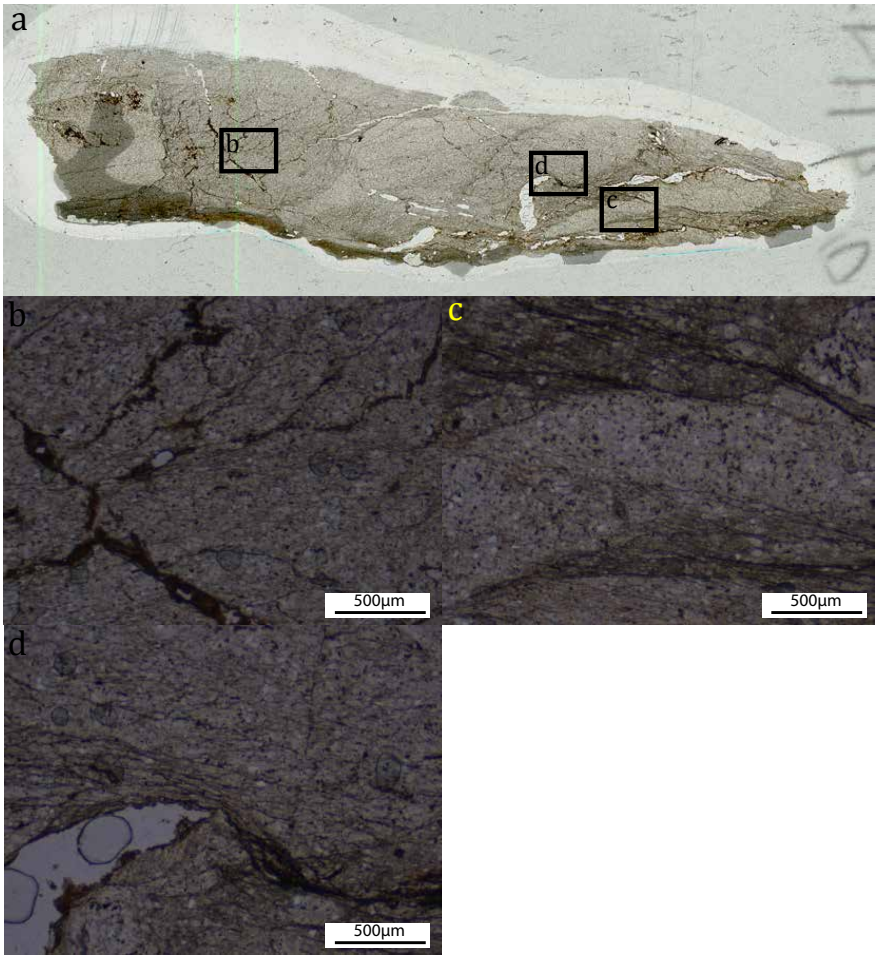

Figure 23: Photomicrographs of thin section AN16-004, the deformed sediment from Cemaes Bay A, with a) an overview of the sample, also showing where in the sample figures b-d come from, b) brown veins and solution seams, c) solution seams curve around the coarser grained/quartz-rich parts, but also go through them, d) crack tip continues as a solution seam

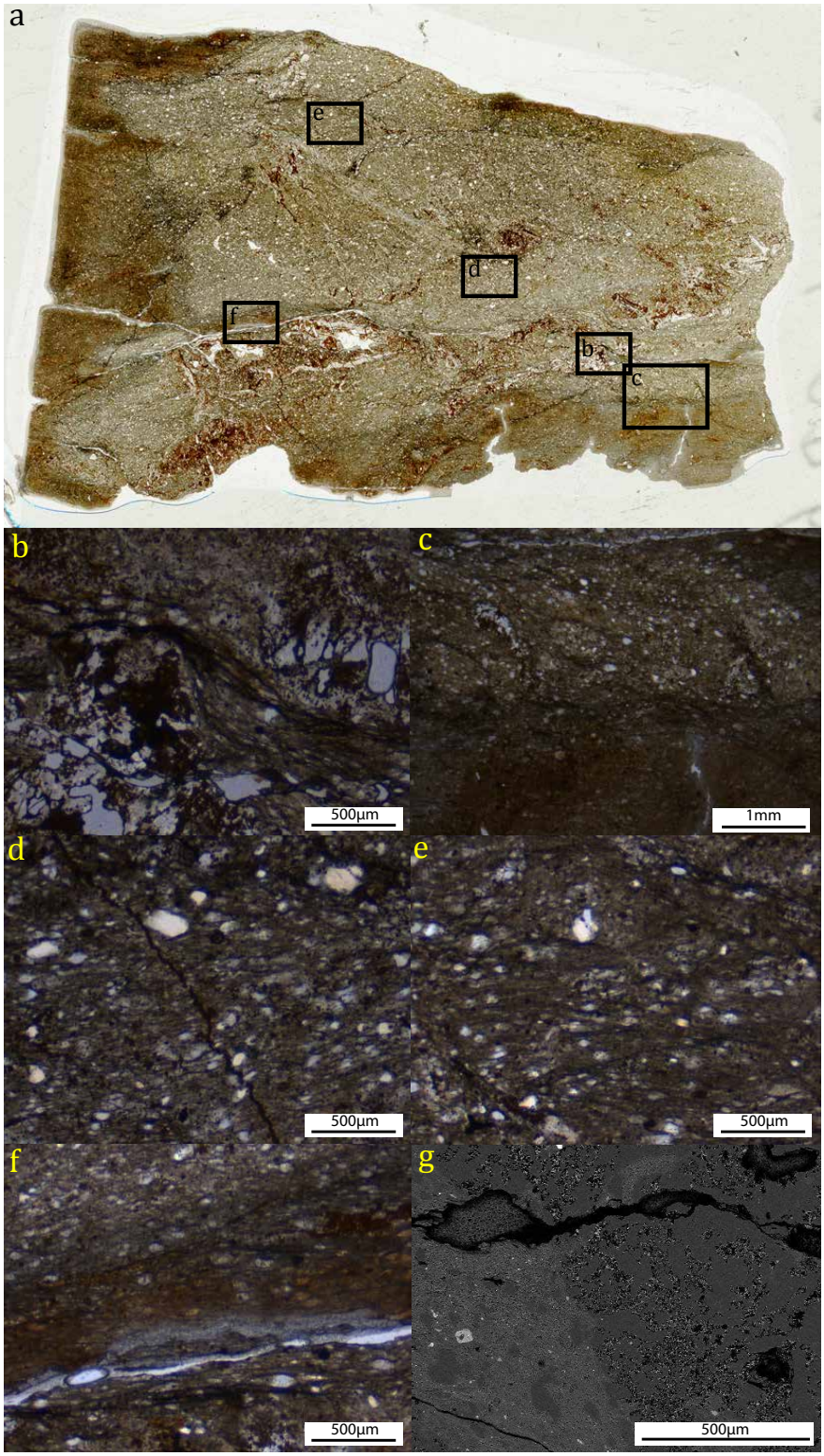

Figure 24: Photomicrographs of thin section AN16-006, the mélange matrix with small blocks, with a) an overview of the sample, also showing where in the sample figures b-g come from, b) the solution seams curve around the blocks, c) solution seams continue into the reaction front, which does not follow specific layering, d) brown veins cross-cut the sample (scalebar=500μm), e) solution seams occur in many different orientations, f) this solution seam has opened and there is alteration along this crack, g) porous quartz block in the right half of the sample, quartz in a network of muscovite on the left (BSE image)

these. This spaced foliation is only very faintly visible in BSE images at low magnification, so this is not defined by a compositional variation (Fig.22g).

The veins are offset along the solution seam (Fig.22c), caused by either shortening or shear displacement along the seam or a combination. The cracks that are present in the same orientation as the solution seams were probably also solution seams, along which opening is easier due to their weakness. Along some of these there are zones of alteration. There are veins of quartz and oxide minerals both parallel to the spaced foliation (Fig.22d), and perpendicular to the first sedimentary and solution seam foliation(Fig.22e).

The in outcrop more deformed sample AN16-004 does not show such a clear foliation. The sedimentary foliation is harder to determine as there are not as many lithological variations (Fig.23a). There are parts with more quartz than the surrounding material, but their boundaries are irregular (Fig.23c). The solution seams curve around these boundaries, but also have irregular shapes and orientations (Fig.23d). There is a second foliation defined by the alignment of muscovite in the matrix. There are some veins filled by oxides and many cracks. These are often parallel to the solution seams, but rather irregular (Fig.23b).

Sample AN16-006 contains some blocks in a muscovite matrix (Fig.24a,b). These blocks are not carbonates, but are made of quartz, which is more porous (>20%) than the surrounding muscovite-rich parts (Fig.24g). Throughout the matrix there are smaller quartz grains present in a network of muscovite. The many solution seams in this sample curve around these larger porous blocks, but also line up to form a through-going shear zone (Fig.24f). Along this there is again a zone of alteration, similar to sample AN16-005. Along the boundaries of this sample there are alteration zones, of which the boundaries are not very clear. There are no lithological boundaries here, the composition is similar to the rest of the sample and the solution seams go through the alteration zone (Fig.24c). There are some very thin ($\sim$20μm) dark veins (Fig.24d).

5.2.3 Cemaes Bay - B

quartzite The quartzite sample (AN16-012) consists almost solely of quartz, although small amounts of muscovite are present at the grain boundaries. Grain size is variable in the sample. In places there are large rounded grains (average diameter 256$\pm$100 μm) that clearly have compacted by pressure solution, because of the grain-to-grain indentations (Fig.25c,d). There are patches of finer grains, with a maximum grainsize of 30 μm (Fig.25e,f). These patches of small grains do not seem to be sedimentary as they do not form layers. There are microcracks, along which small new quartz grains have formed, that cross-cut the larger grains (Fig.25e,f). Many of the quartz grains show undulose extinction, including grains that show subgrains with an average subgrainsize of 110μm (Fig.25g,h). Some also have finer grains (<50μm) along the grain boundaries.

quartz-rich matrix In the outcrop it was visible this matrix consisted mainly of quartz lenses with some highly deformed layers. One of these highly deformed

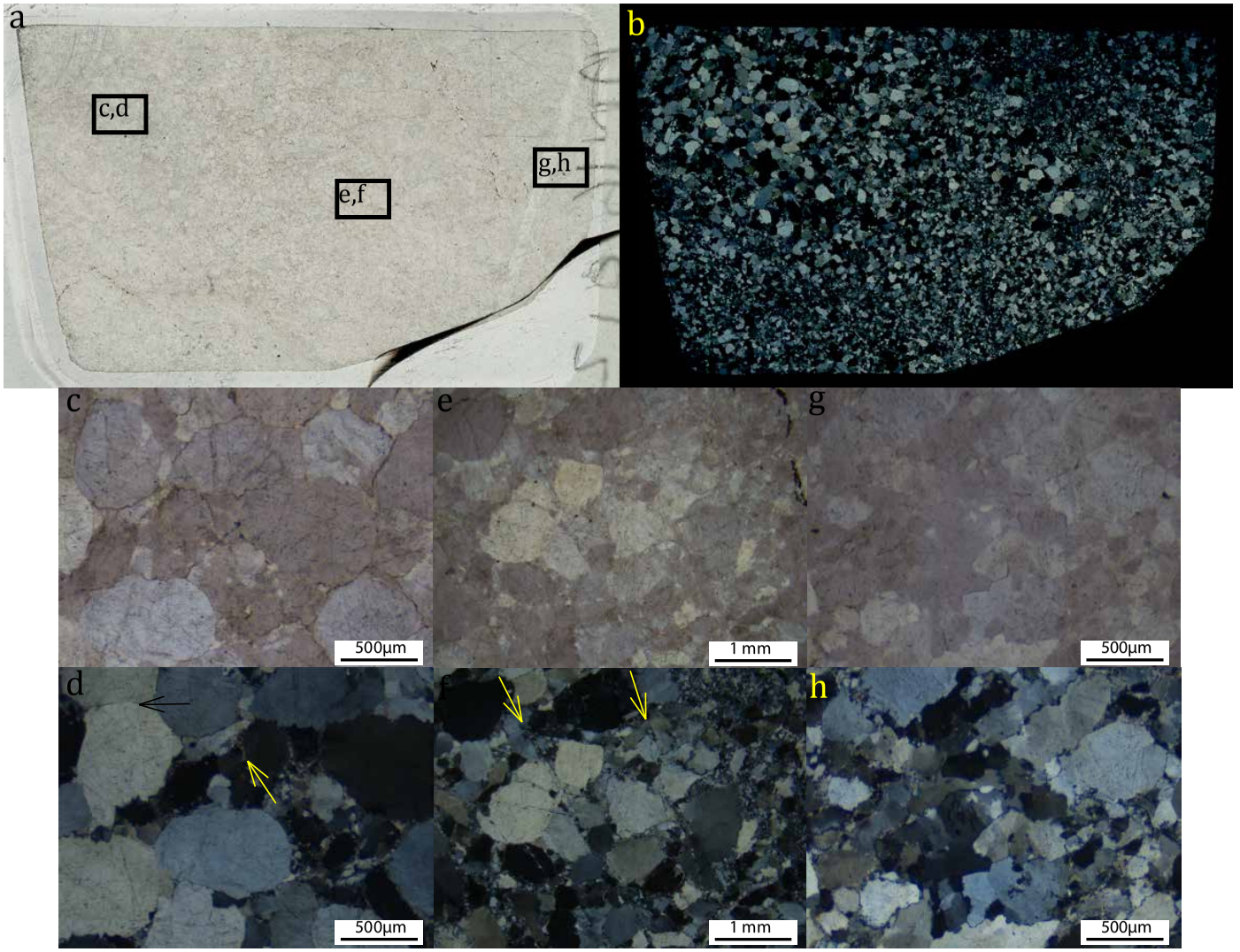

Figure 25: Photomicrographs of thin section AN16-012, the quartzite, with a) an overview of the sample, also showing approximately where in the sample figures c-h come from, b) an overview of the sample in cross-polarized light, showing there are coarse and fine grained areas, but no clear layering, c&d) rounded quartz grains with indentations (black arrow), no undulose extinction and muscovite present at the grain boundaries (yellow arrow) (c=ppl, d=xpl), e&f) microcracks, which are thin bands of new grains, cut though the large grains (yellow arrows), at the top right corner, a patch of small grains is present (e=ppl, f=xpl), g&h) elongated grains with subgrain formation (g=ppl, h=xpl)

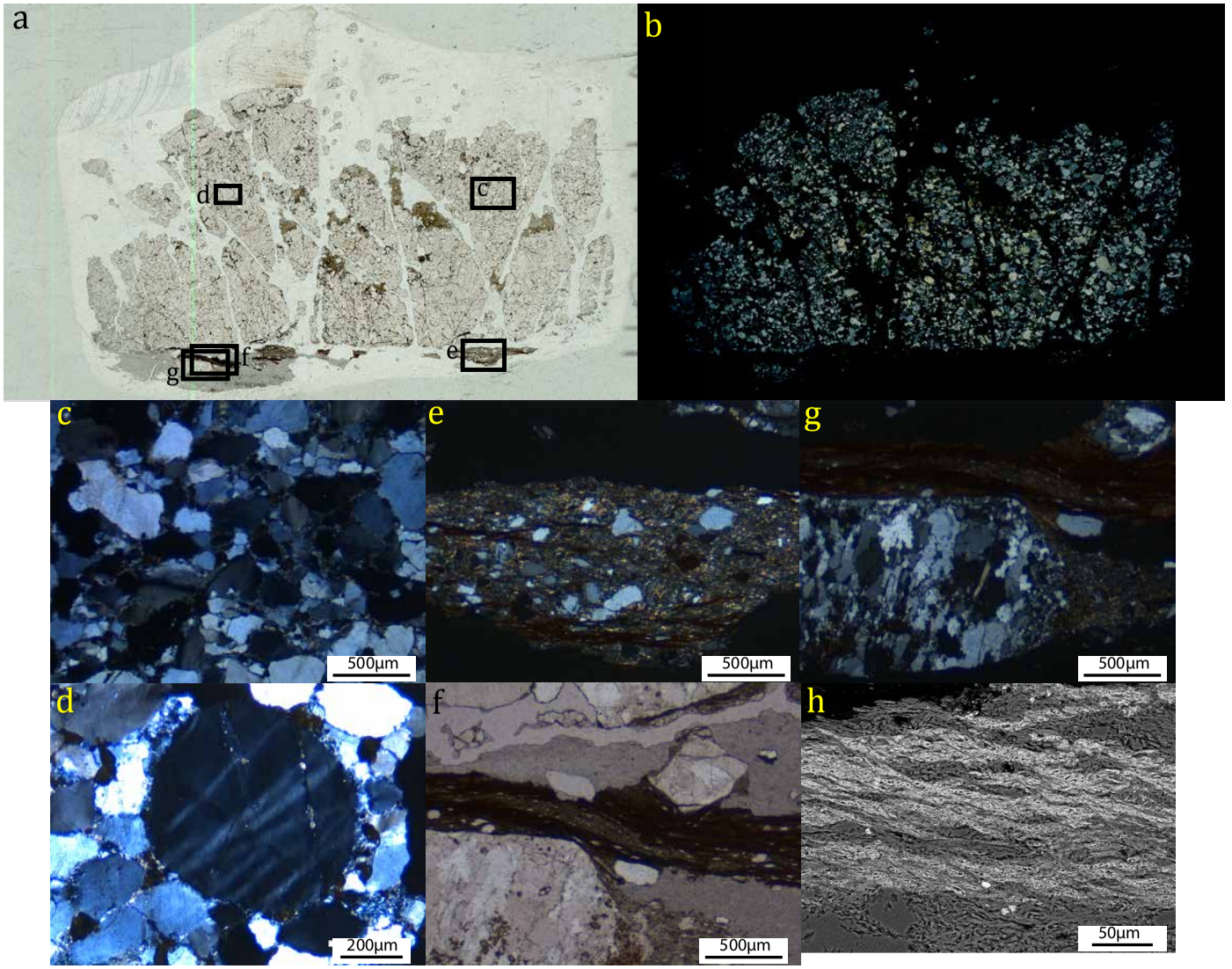

Figure 26: Photomicrographs of thin section AN16-011, a quartz block in the mélange matrix, with a very localized layer at the bottom, with a) an overview of the sample, also showing where in the sample figures c-h come from (ppl), b) an overview of the sample in cross-polarized light, showing there are coarse and fine grained areas, but no clear layering, c) undulose extinction and small grains at the grain boundaries (xpl), d) extinction lamellae in a quartz grain (xpl), e) thin layer of localized deformation with solution seams in cross-polarized light, f) even more localized deformation and more solution seams, g) the small quartz block has elongated grains with irregular grain boundaries (xpl), h) the solution seams consist of muscovite (grey) and titanium and iron oxide (white), there is a second foliation in the direction of the arrow on top of the horizontal foliation of the solution seams (BSE-image)

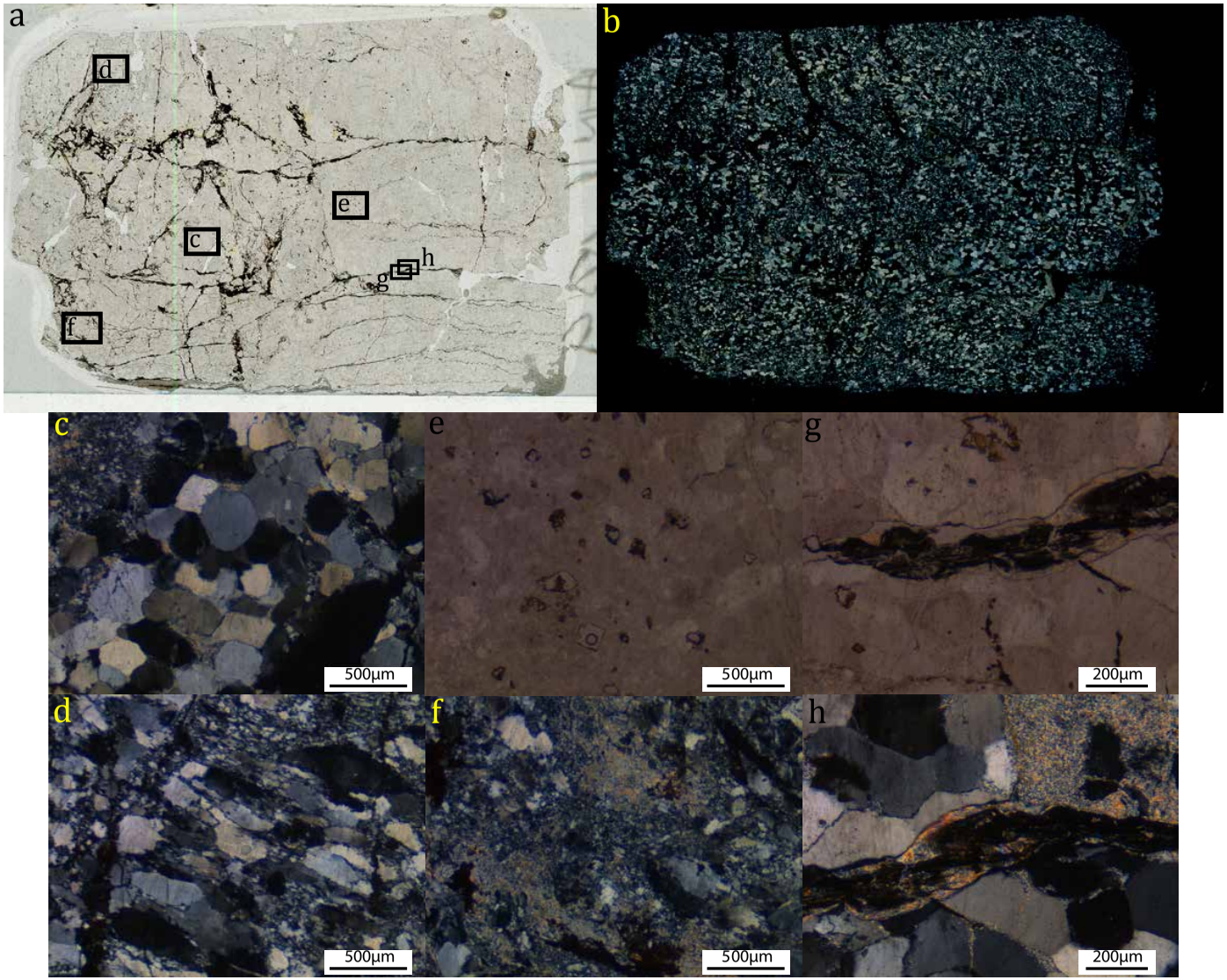

Figure 27: Photomicrographs of thin section AN16-009, the quartz boudin, with a) an overview of the sample, also showing where in the sample figures c-h come from (ppl), b) an overview of the sample in cross-polarized light, showing there are coarse and fine grained areas, but no clear layering, c) some of the larger grains, indenting but with little undulose extinction, some small grains are present at the boundaries (xpl), d) these grains are elongated and there are many smaller grains (xpl), e) square gaps in the quartz block, f) patches of muscovite in between the small quartz grains (xpl), g) solution seam in the quartz, h) solution seam is enriched in muscovite, which is also present in between the quartz grains and in large amounts at the right top (xpl)

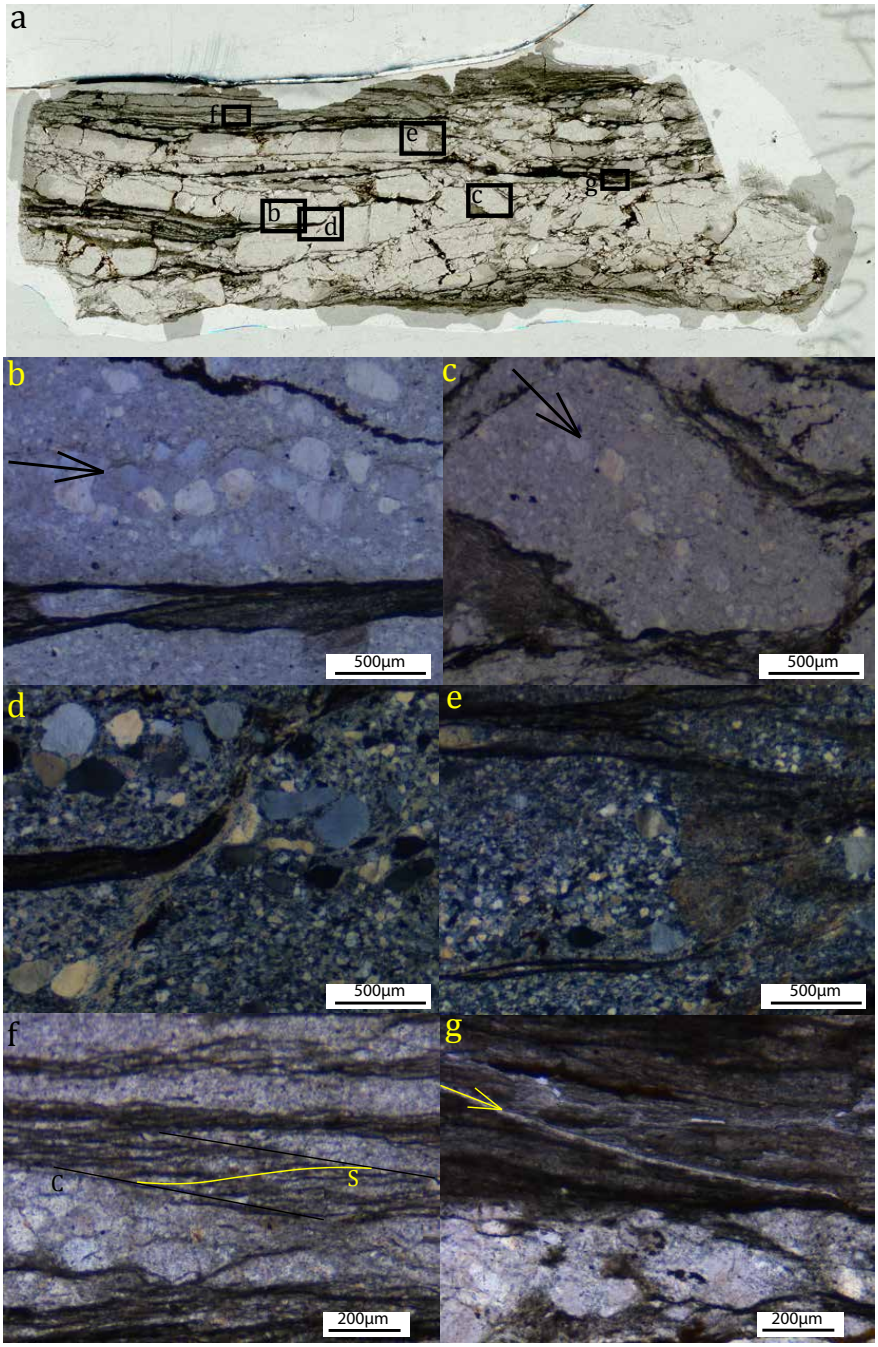

Figure 28: Photomicrographs of thin section AN16-008, mélange matrix with many quartz blocks, with a) an overview of the sample, also showing where in the sample figures b-g come from, b) the coarse grained layer inside the blocks has the same orientation as the solution seams, c) the coarse grained layer in this block is tilted, d) the coarse grained layer is displaced, where the block is broken it is enriched in muscovite , also note the quartz grains do not show subgrain formation or undulose extinction (xpl), e) the end zones of the block have been enriched in muscovite (xpl), f) the solution seams show a C-S texture, g) a planar crack cuts through the solution seams

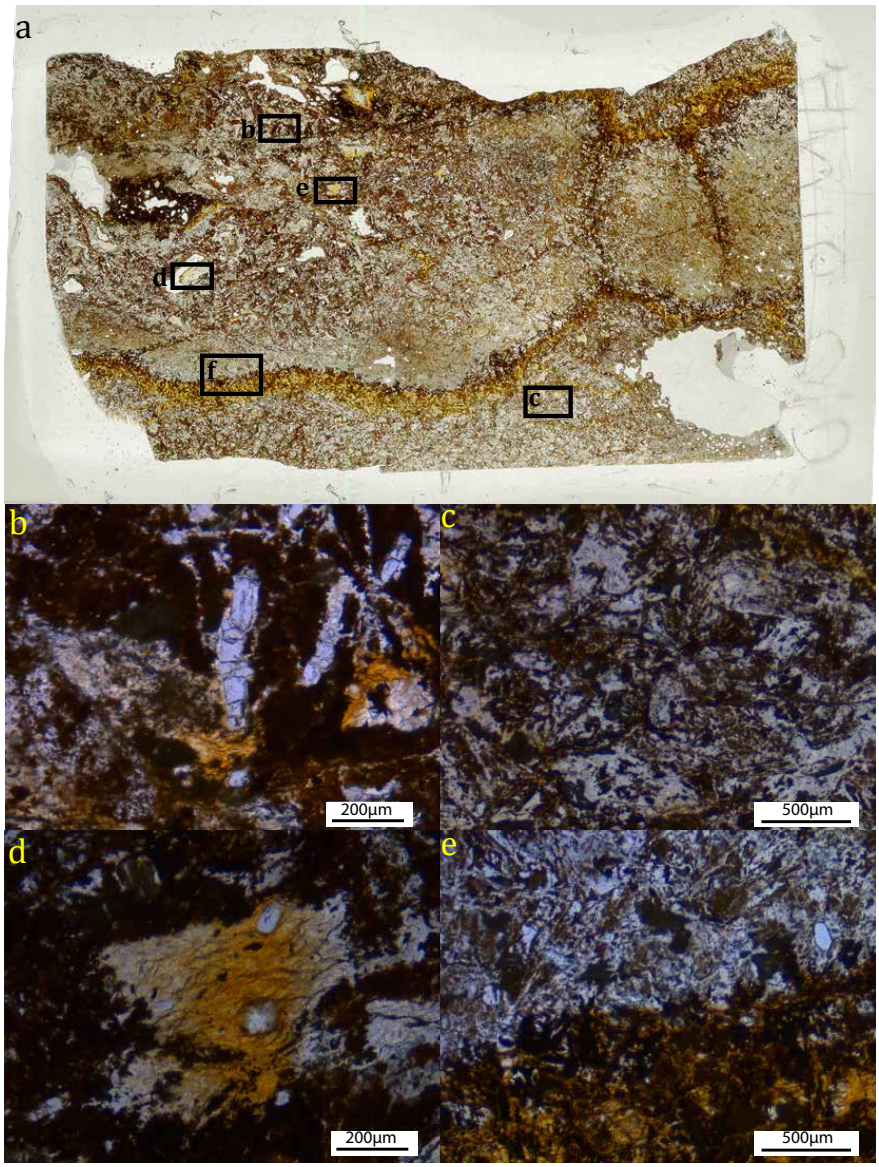

Figure 29: Photomicrographs of thin section AN16-010, the highly deformed layer at Cemaes B, with a) an overview of the sample, also showing where in the sample figures b-f come from, b) an apatite crystal, c) there is no clear alignment in this sample, d) wavy structure in muscovite, e) the reaction front where rutile is formed

layers, which are muscovite rich, can be seen on the bottom part of this thin section (AN16-011) (Fig.26a,b). Inside the quartz lens, there are the same variations in grain sizes as in the quartzite sample and also muscovite is present at the grain boundaries (Fig.26c). On top of that there are grains with linear extinction bands in them, these were also present in the quartzite (AN16-012), but are more clear in this sample (Fig.26d). The whole sample shows two directions of cracks, along which there are more iron and titanium oxides.

Fig.26e-h show the highly deformed layer going through the quartz. There are clear signs of pressure solution here, with wide (10-200μm) solution seams that curve around the larger quartz clasts. A second foliation is present in the solution seams (Fig.26h). The quartz clasts in the shear zone are mostly undeformed, the amount of grains that show subgrain formation is less than inside the quartz blocks. The small quartz block in the matrix does show subgrain formation, with quartz grains that are elongated perpendicular to the solution seams (Fig.26g).

quartz boudin The quartz boudin sample AN16-009 looked elongated in the field, but this is not clear in the thin section. The quartz grains are rounded and there are large variations in grainsize, with parts with coarse indenting grains (average diameter 277 μm) and other parts with a very fine recrystallized grainsize (average diameter 30 μm) (Fig.27c). Certain fine grained parts do show a clear elongation direction (Fig.27d), others do not. There do not seem to be any systematics in where the coarser and finer grained areas are. There are mostly horizontal solution seams and mostly (sub)vertical cracks. The solution seams are lined with muscovite (Fig.27g,h). Muscovite is also present in the quartz, both at the triple junctions between the coarse grains and in patches in the finer grained zones (Fig.27f). There are also zones made up solely of muscovite. In the middle of one of the finer grained zones there are square gaps where crystals used to be (Fig.27e).

quartz matrix The mélange matrix in sample AN16-008 contains many quartz blocks, with solution seams in between them. The blocks have variable sizes, being up to 4 mm in length and up to 2 mm thick (Fig.28a). In some of the blocks there are coarser sedimentary layers present, which show these blocks still have their original orientation and that the solution seams have formed parallel to the original bedding (Fig.28b). In places, these blocks are fractured and these zones are enriched in muscovite (Fig.28d). At the end of the blocks, there are zones filled with this same muscovite (Fig.28e). In the right-hand zone of this thin section, the blocks are not as rectangular and show more rotation as the coarse grained layers are not parallel to the solution seams any more (Fig.28c). The solution seams show C-S type structures, indicating dextral shear (Fig.28f). Through one area of solution seams, a shear fracture is present, which offsets all features. The amount of displacement is uncertain as no markers are present on both sides of the fracture (Fig.28g).

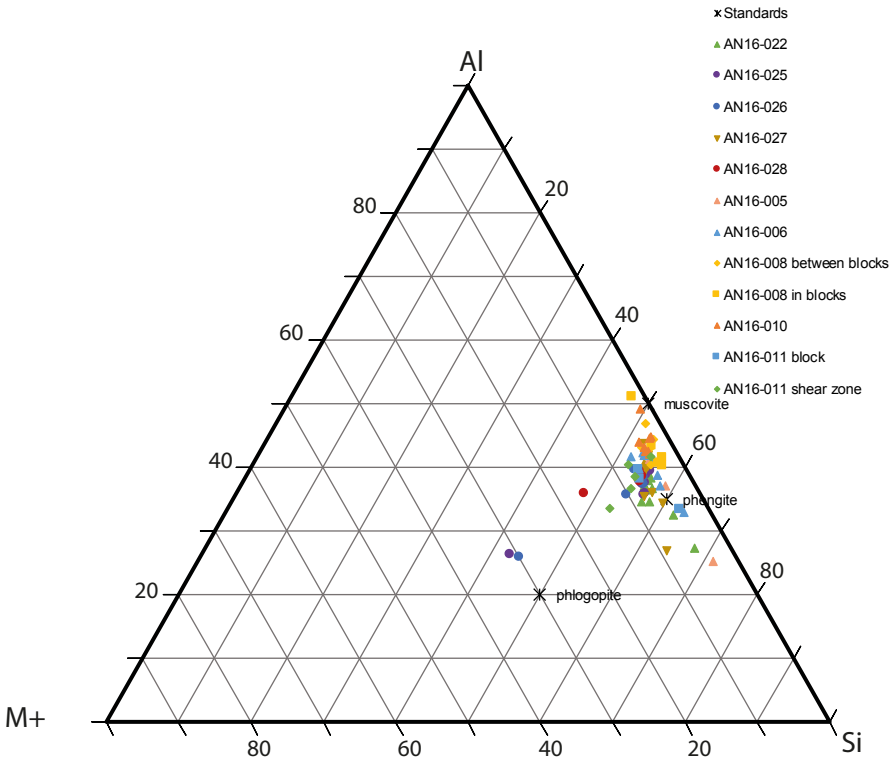

Figure 30: ternary graph showing the composition of white mica

'red' matrix In outcrop, there was one thin layer of a few centimeters wide, that seemed sheared and had a reddish colour. The thin section of this sample (Fig.29a) shows no foliation, but a very fine grained chaotic matrix (Fig.29c). This matrix consists of mostly muscovite, with some kaolinite and the dark grains are iron and titanium oxides. There are elongated apatite grains, which are sometimes broken (Fig.29b). In places there are larger zones of muscovite, up to millimeters in size. There may be quartz included in these zones and some of them show a wavy foliation (Fig.29d). There are clear reaction rims, where the light-coloured matrix is in sharp contrast with the black titanium oxides. On the side of the titanium oxides there is a zone that looks yellow in thin section, but that has the same composition as the light-coloured matrix (Fig.29e).

5.3 Mineral compositions

As the mineral assemblages in Table 1 show, several samples contain chlorite and white mica. Chlorite composition can be used to estimate paleotemperature. White mica end-member composition can be used to tell in which setting it was

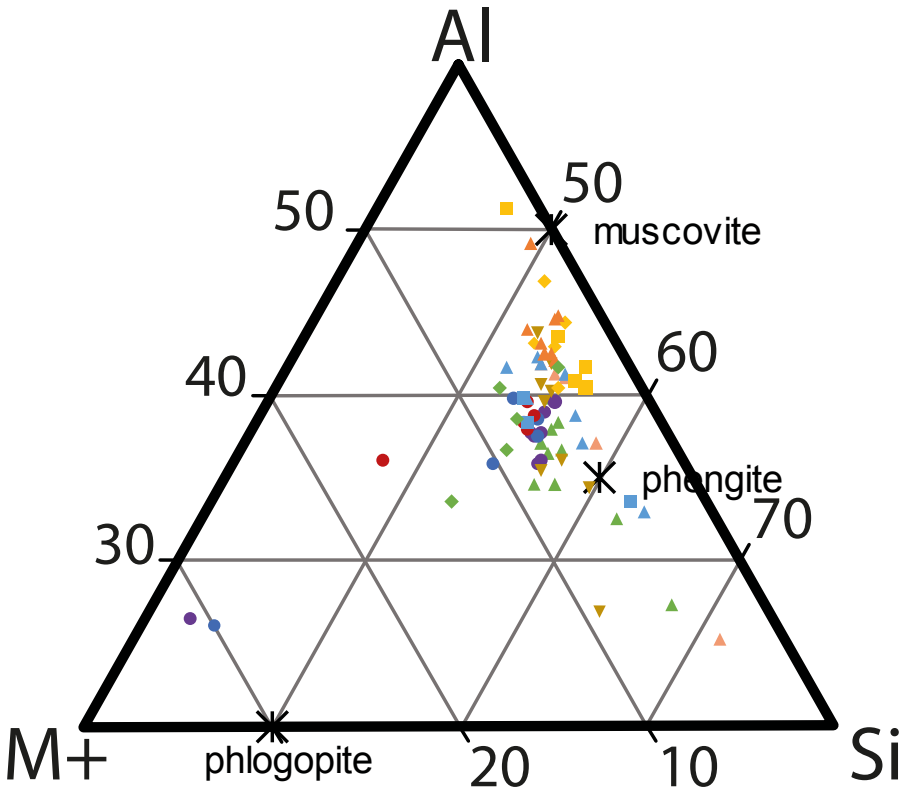

Figure 31: close-up of end-members compositions of white mica from Figure. 30, symbols are identical

formed. Therefore these compositions are given in Appendices A and B.

5.3.1 White mica

End-member composition of white mica depends on the relative amounts of aluminium (Al), silicium (Si) and the metals iron and magnesium (M+). Figure 30 gives an overview of these components as well as the end-members muscovite, phengite and phlogopite. This shows most white mica has a phengitic composition, with typical values of 3.3 Si p.f.u., although there are exceptions. There are two basalt measurements (circles) with a high M+ component, but these can be explained by being close to an iron-rich mineral interfering in the measurement.

There are sediment measurements (triangles) with higher than phengitic silica content, these generally also contain less potassium. This can be explained by the abundant quartz and albite in the sample, which may interfere with the measurements of the very fine mica. Another possibility is the presence of illite ($K_{1.5\text{-}1.0}Al_4[Si_{6.5\text{-}7.0}Al_{1.5\text{-}1.0}O_{20}](OH)_4$), distinguished from muscovite by the higher silica and lower potassium content and finer grain-size.

The quartz samples AN16-008 and AN16-010 (yellow and orange) have a higher muscovite content, but the muscovite in these samples might be detrital and can have inherited signatures. There does not seem to be any systematic variation of muscovite composition in between the quartz in the blocks (squares) and muscovite in shear zones (diamonds).

5.3.2 Chlorite

High concentrations of calcium, sodium and potassium in chlorite cause the estimated paleotemperature to be too low (Jiang et al., 1994). Table 2 gives an overview of chlorite compositions and calculated paleotemperature for samples where the amount of [Ca+Na+K] is <0.20 p.f.u. Temperatures are calculated using the methods by Cathelineau (1988), Zang and Fyfe (1995) and Kranidiotis and MacLean (1987). The method by Zang must be preferred when the content of iron relative to magnesium and manganese is high (>0.50) and although no samples reach values this high, differences between the geothermometers are significant for the samples with high iron content AN16-022, AN16-027 and AN16-028. Therefore it is likely that for these samples the temperature calculated using the method of Zang is more realistic. Therefore, formation temperature of the chlorite in AN16-022 is ∼230°C. For sample AN16-025 the geothermometers agree at a chlorite formation temperature of ∼240°C. The chlorite in the hyaloclastite sample AN16-026 was formed at a slightly higher temperature, but in this case the geothermometer of Kranidiotis and MacLean (1987) should be favoured, since this one must be preferred when magnesium content is high. Therefore the most realistic formation temperature is around ∼260°C. The deformed sediment AN16-027 has only two chlorite analyses with less than 0.20 [Ca+Na+K], which have a quite high iron content and a quite high magnesium content. The temperatures calculated by the different methods yield very different values, the real temperature is probably somewhere in between the calculated values around ∼270°C. The undeformed basalt AN16-028 also has relatively high iron content and magnesium content, the real value is around a temperature of ∼270°C.

Chlorite occurs both in the rock matrix as metamorphic chlorite and in veins as hydrothermal chlorite. There is no difference in calculated formation temperature for the two different types of chlorite. In the hyaloclastite and in the undeformed basalt, chlorite was also measured in vesicles. There seems to be no difference between the chlorite formation temperatures between the vesicles and the chlorite in veins.

Figure 32 shows that there is no relationship between temperature calculated from the chlorite and phengite content of muscovite, an indicator for pressure. There are large internal variations per sample and not much variation between the samples.

Table 2: Composition of chlorite in wt% and p.f.u., based on 28 oxygen, for analyses with <0.20 [Ca+Na+K] p.f.u.

Sample	AN16-022				AN16-025				AN16-026				
Analysis #	1	4	8	avg*	2	4	5	avg*	3	4	6***	7	avg*
MgO	16.28	15.22	15.59		27.81	29.13	28.95		32.18	32.98	32.39	32.49	
Al2O3	23.26	24.03	22.92		23.13	24.51	24.34		23.57	23.63	24.10	23.71	
SiO2	32.61	31.32	32.14		38.25	34.55	36.05		35.28	34.42	34.47	34.47	
K2O	0	0	0.32		0.56	0	0		0.00	0.00	0.00	0.00	
MnO	1.7	2.33	1.98		0	0	0		0.00	0.00	0.00	0.00	
FeO	26.15	27.09	27.05		10.25	11.82	10.67		8.97	8.97	9.04	9.34	
Total	100	99.99	100		100	100.01	100.01		100.00	100.00	100.00	100.00	
Si	5.93	5.75	5.90		6.38	5.84	6.04		5.89	5.76	5.77	5.78	
Al(IV)	2.07	2.25	2.10		1.62	2.16	1.96		2.11	2.24	2.23	2.22	
Al(VI)	2.92	2.95	2.86		2.93	2.72	2.84		2.53	2.42	2.52	2.46	
Fe	3.98	4.16	4.15		1.43	1.67	1.49		1.25	1.26	1.27	1.31	
Mn	0.26	0.36	0.31		0.00	0.00	0.00		0.00	0.00	0.00	0.00	
Mg	4.42	4.17	4.27		6.92	7.34	7.23		8.01	8.23	8.08	8.12	
Ca	0.00	0.00	0.00		0.00	0.00	0.00		0.00	0.00	0.00	0.00	
Na	0.00	0.00	0.00		0.00	0.00	0.00		0.00	0.00	0.00	0.00	
K	0.00	0.00	0.07		0.12	0.00	0.00		0.00	0.00	0.00	0.00	
Fe/(Fe+Mg+Mn)	0.46	0.48	0.48		0.17	0.19	0.17		0.14	0.13	0.14	0.14	
Ca+Na+K	0.00	0.00	0.07		0.12	0.00	0.00		0.00	0.00	0.00	0.00	
T(C)**	270.9	299.8	276.2	282	198.3	286.3	254.1	246	277.7	298.5	297.8	296.1	293
T(Z)**	225.9	243.2	227.9	232	204.9	261.7	241.8	236	260.7	274.7	273.9	272.5	270
T(K)**	271.3	291.7	275.9	280	202.1	261.0	238.8	234	251.7	265.2	264.9	264.0	261

Sample	AN16-027			AN16-028							
Analysis #	2	3	avg*	1	2	3	4***	5***	6***	10	avg*
MgO	20.42	18.39		21.56	23.88	22.34	22.43	23.14	22.27	23.56	
Al2O3	25.65	24.44		24.19	22.16	22.97	22.84	23.28	23.89	23.45	
SiO2	30.88	33.23		31.12	34.16	31.84	32.62	31.96	31.59	33.46	
K2O	0.00	0.00		0.00	0.00	0.00	0.00	0.00	0.00	0.00	
MnO	0.00	0.00		0.80	0.00	0.58	0.00	0.66	0.00	0.00	
FeO	23.06	23.94		22.33	19.80	22.27	22.11	20.97	22.25	19.53	
Total	100.00	100.00		100.00	100.00	100.00	100.00	100.00	100.00	100.00	
Si	5.51	5.92		5.57	5.99	5.69	5.80	5.68	5.63	5.86	
Ti	0.00	0.00		0.00	0.00	0.00	0.00	0.00	0.00	0.00	
Al(IV)	2.49	2.08		2.43	2.01	2.31	2.20	2.32	2.37	2.14	
Al(VI)	2.91	3.06		2.67	2.57	2.53	2.58	2.55	2.64	2.70	
Fe	3.44	3.57		3.34	2.90	3.33	3.29	3.11	3.31	2.86	
Mn	0.00	0.00		0.12	0.00	0.09	0.00	0.10	0.00	0.00	
Mg	5.43	4.89		5.75	6.24	5.95	5.94	6.13	5.91	6.15	
Ca	0.00	0.00		0.00	0.00	0.00	0.00	0.00	0.00	0.00	
Na	0.00	0.00		0.00	0.00	0.00	0.00	0.00	0.00	0.00	
K	0.00	0.00		0.00	0.00	0.00	0.00	0.00	0.00	0.00	
Fe/(Fe+Mg+Mn)	0.39	0.42		0.36	0.32	0.36	0.36	0.33	0.36	0.32	
Ca+Na+K	0.00	0.00		0.00	0.00	0.00	0.00	0.00	0.00	0.00	
T(C)**	338.2	272.5	305	329.5	261.5	310.1	292.6	312.3	320.2	282.3	301
T(Z)**	277.0	230.4	254	273.6	233.0	261.5	249.9	265.0	267.8	246.7	257
T(K)**	310.2	269.5	290	302.6	254.5	289.3	277.8	289.1	296.2	268.2	283

*average temperatures of the sample

** T(C) means temperature calculated according to Cathelineau (1988), T(Z) means temperature calculated according to Zang and Fyfe (1995), T(K) means temperature calculated according to Kranidiotis and MacLean (1987), all temperatures are in °C

*** these measurements are inside vesicles

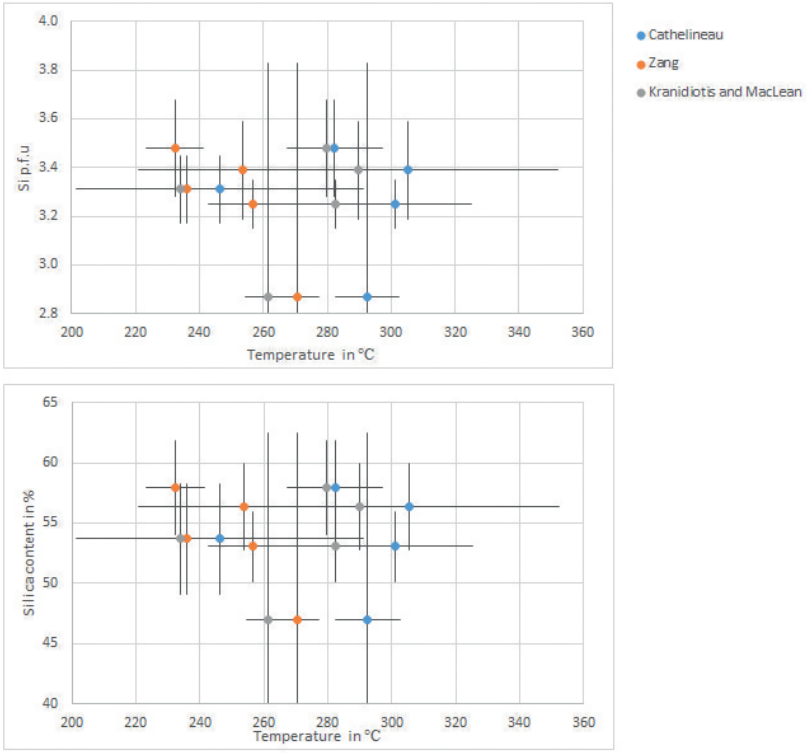

Figure 32: Temperatures calculated using the three different methods plotted against average sample silica content in phengite for a) amount of Si p.f.u. and b) percentage of Si of the total of silica, aluminium and M+ content, error bars are one standard deviation, only measurements of Table 2 are included

6 Discussion

When studied closely, samples of the two different locations share many deformation features, due to their common deformation history. The sequence of deformation events will be given first, including some problems and uncertainties, followed by the deformation of mineralized veins and carbonate blocks. After this, the importance of the different deformation mechanisms will be discussed and their implications for the deformation temperature. Using the temperature and appropriate laws and models for the found deformation mechanisms, estimates of stress and strain rate are made.

6.1 Deformation sequence

The sedimentary samples and mélange matrix share many deformation features. An overview of these is given in table 3. However, the basaltic samples do not show the same features and will therefore be treated separately.

6.1.1 D1: layer-perpendicular shortening

The first structure that developed in these rocks was a sedimentary foliation, preserved in relatively undeformed sediments like AN16-022, where the graded beds define the layering as sedimentary. In sample AN16-005, the other relatively undeformed sediment, the coarser lenses lack internal layering, but their alignment direction shows the sedimentary foliation. The quartz blocks in the mélange in sample AN16-008 have coarser layers that define this first sedimentary foliation S0. In carbonate sample AN16-007 this sedimentary layering is preserved by the fine stylolitic layers.

The pressure solution seams parallel to the sedimentary bedding indicate there was layer perpendicular compression, related to the burial of these rocks, under conditions where pressure solution was the dominant deformation mechanism. Bedding-parallel solution seams are present in all sedimentary samples, except AN16-004. The solution seams in this sample are not planar and curve around the also not planar bedding surfaces. The carbonate blocks AN16-007 and AN16-013 show irregular stylolites, as is common in carbonates (Railsback, 1993), instead of planar solution seams.

6.1.2 D2: oblique shortening

There was a second phase of shortening during which pressure solution was the dominant deformation mechanism in the sediments, because there is a second set of solution seams at an angle to the sedimentary foliation and first solution seams (Fig.33). These are especially clear in sample AN16-022, where they make an angle of 30° with the first sedimentary foliation. They are mostly visible in the finer grained layers, but seem to continue into the coarser grained layer as veins with some brown mineral. A possible explanation for this is that pressure solution is more efficient in the finer grained layers, because a finer

Table 3: overview of the deformation features seen in each sample

Sample number	short description	location	sedimentary layering S0	layer parallel solution seams S1	layer oblique solution seams S2	spaced foliation S3 (angle to S0)
AN16-004	Cemaes Bay A	most deformed mélange matrix	±	No	Yes	No
AN16-005	Cemaes Bay A	least deformed mélange matrix	Lenses	Yes	No	Yes (35°)
AN16-006	Cemaes Bay A	mélange matrix including small blocks	Yes*	Yes	Yes	No
AN16-007	Cemaes Bay A	carbonate block in mélange	Yes	Yes (stylolites)	No	No
AN16-008	Cemaes Bay B	mélange matrix	Yes	Yes	No	No
AN16-009	Cemaes Bay B	quartz block in mélange	No	Yes	No	No
AN16-010	Cemaes Bay B	fine grained mélange matrix	No	No	No	No
AN16-011	Cemaes Bay B	mélange matrix	Yes	Yes	No	No
AN16-012	Cemaes Bay B	quartzite block in mélange	No	No	No	No
AN16-013	Cemaes Bay A	elongated carbonate mélange block	No	Yes**	Yes**	No
AN16-022	Newborough Wood	folded siliceous mudstone	Yes	Yes	Yes	Yes (60°)
AN16-025	Llandwyn Island A	elongated pillow basalt in dolostone	No	No	No	No
AN16-026	Llandwyn Island A	deformed hyaloclastite	No	No	No	No
AN16-027	Llandwyn Island A	deformed schistose mudstone	±	Yes	No	No
AN16-028	Llandwyn Island B	greenish pillow basalt in less deformed lens	No	No***	Yes***	Yes (30°)

* assuming the blocks define a sedimentary layering

** there are two directions of stylolites

*** there are two alignment directions, but no solution seams, see text for explanation

grain size increases the rate of the process (Rutter, 1976). This may lead to a space accommodation problem in the coarser grained layer, which then needs to crack and when the cracks get filled the veins form. Sample AN16-004 also has solution seams that are not parallel to the bedding, but these do not define a clear foliation.

Sample AN16-013 has stylolites in two directions and although there is no sedimentary layering, it is likely these formed during the same deformation phases as the other solution seams, so one of these directions is parallel to the bedding and one is oblique. The angle in between these two directions is harder to estimate because of the irregular nature of the stylolites, but is roughly 60°, which is certainly significantly larger than in AN16-022.

Related to this shortening may be the C-S structures in the solution seams in samples AN16-008 and AN16-011, indicating shear displacement along the solution seams. In other samples, like AN16-005, AN16-006 and AN16-009, it is also possible there was shear displacement along the solution seams. Some of the blocks in AN16-008 are rotated, which can happen to rigid blocks in an otherwise ductile shear zone (Simpson and Schmid, 1983). This indicates there was a simple shear component on top of the volume loss due to pressure solution. Also the strain shadows around the blocks indicate this shear.

The hyaloclastite sample AN16-026 shows a clear elongation direction in the shape of the basalt lens and in the shape of the sheared vesicles. The basalt lens shows asymmetry and is pulled apart, causing fractures perpendicular to the elongation direction, which indicate this block was also subjected to simple shear. The vesicles are elongated, which could be the result of pressure solution compaction, but there are no signs for pressure solution here, so it is most likely they are elongated because of the shear event. That there are no signs of pressure solution is also the problem, because it is not possible to relate this direction of shear to the direction of pressure solution, so it is theoretically possible these features are related to a different shear event. The vesicles close to the basalt have retained their supposedly original round shape, whereas vesicles further away are stretched. This means strains are higher in the carbonate matrix than close to the blocks.

6.1.3 D3: spaced foliation

The third, spaced foliation, which makes a larger angle with the primary foliation than the inclined solution seams, is present only in samples AN16-005 and AN16-022, both being relatively undeformed. Unfortunately, SEM studies have not revealed what defines this spaced foliation. Sample AN16-022 comes from an outcrop that shows upright folds, so this might be an axial planar foliation related to the folds seen in the outcrop. To know if this is the case, it should be investigated whether or not the angle between the foliation and the bedding changes along the fold.

This is in contrast to sample AN16-005, which was a relatively undeformed sedimentary part in the mélange. The angles relative to the bedding planes in these two samples are 60° (sample AN16-022) and 35° (sample AN16-005), but

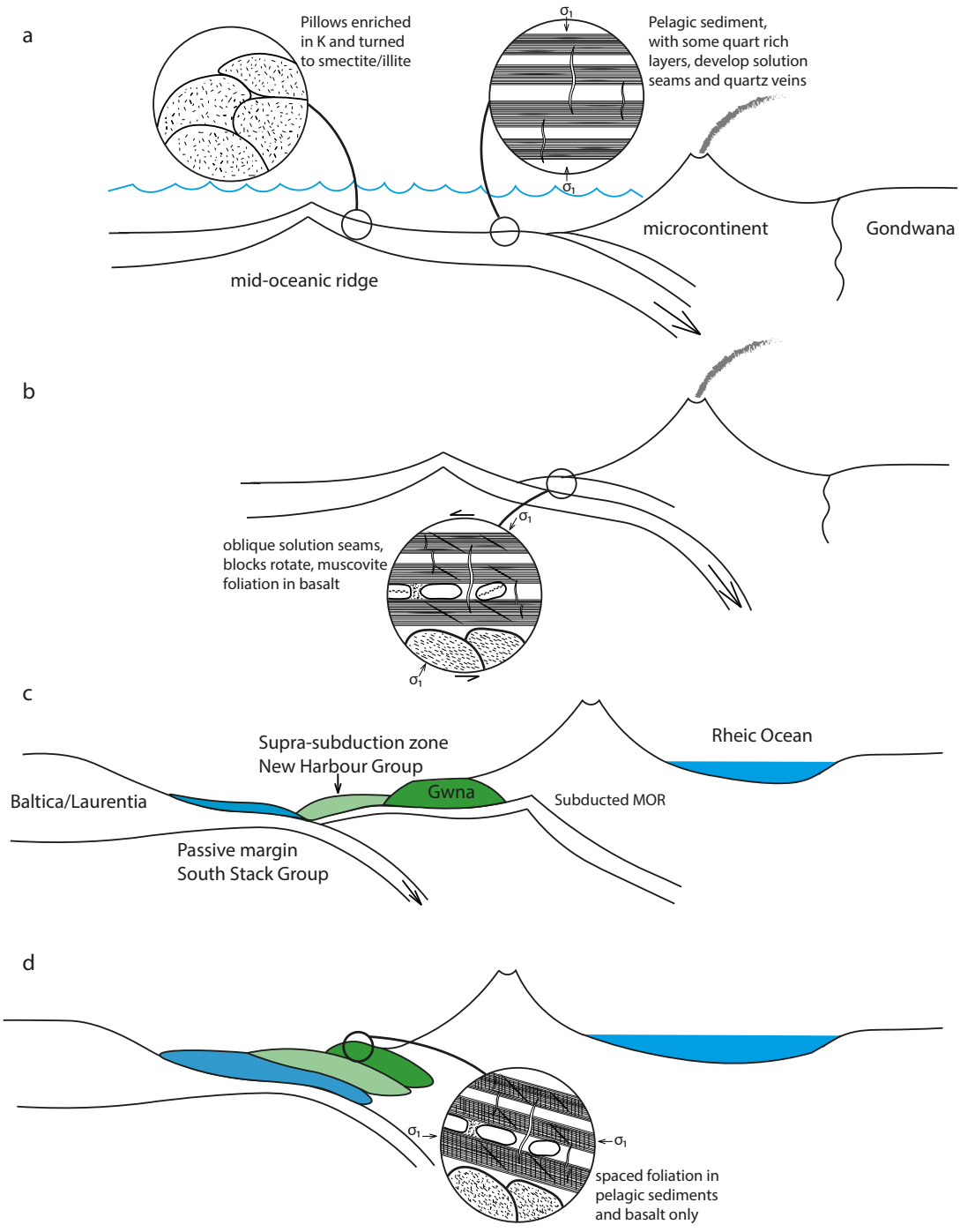

Figure 33: cartoon of deformation events, with first a) the sediments compact by pressure solution, b) subduction causes oblique solution seams, rotation of blocks and formation of a muscovite foliation in the pillow basalts, c) subduction of the mid-oceanic ridge stops subduction, the New Harbour group forms in a supra-subduction zone and the South Stack group forms as passive margin sediments, d) Collision causes underplating of the North-Harbour Group and South Stack Group and causes the development of a spaced foliation in the fine grained sediments and basalts

the orientations of the bedding planes are also different, so it might be that these spaced foliations have the same orientation on Llandwyn and at Cemaes Bay. This argues for this spaced foliation to develop late in the deformation history and might be the result of late shortening, for example by the closing of the Iapetus Ocean and the collision of Baltica and Laurentia with the microcontinent on which Anglesey was located.

6.1.4 Foliations in the basalt

When comparing the two basalt samples from Llandwyn, the first thing to be noted is the lack of foliation in sample AN16-028. This directly implies the foliation in AN16-025 must be a tectonic foliation, because if it was a flow lineation or related to burial, it should be present in both samples. There are two foliations in the deformed basalt, making an angle of about 30°. Although it is possible one of these is a D1 feature and related to layer-perpendicular compaction, the lack of a foliation in the undeformed basalt makes this unlikely. It is more likely these foliations are related to D2 and D3, but as they are similar in character it is not possible to determine which one is which.

6.2 Precipitates

6.2.1 Quartz veins

The thicker quartz veins that make an angle with the solution seams could in principle be related to both pressure solution foliations. They are offset by both the horizontal and the inclined solution seams and in places the cracks related to the inclined solution seams seem to overgrow the veins. This would indicate the veins were present before there was pressure solution, but it is most likely they formed simultaneously. This is because veins form parallel to the maximum principal stress whereas solution seams form perpendicular to the maximum principal stress. As these veins vary in angle from perpendicular to the layer-parallel solution seams to perpendicular to the inclined solution seams, they have formed during the same stress regime and the quartz in the veins is likely to be the result of dissolution along these solution seams.

6.2.2 Carbonate in veins

The calcite veins in the basalt samples have irregular shapes and do not form a foliation like the quartz veins. This is not surprising as it was visible in outcrops that the calcite filled the interpillow spaces. The calcite is recrystallized even in the less deformed basalt. In this less deformed basalt sample (AN16-028), the recrystallization took place by the formation of subgrains, although no subgrains are rotated enough to actually make new, recrystallized grains. Less twinned crystals are present in the middle of one calcite zone, these show only little signs of subgrain formation and probably grew by grain boundary migration as the grain boundaries are bulging into the surrounding grains.

In the more deformed basalt sample (AN16-025), the calcite is also more deformed. Instead of only thin twins and subgrains, there are many thick twins and subgrain formation has progressed to a point where there are already many small recrystallized grains. Even twins are recrystallized. An exception to this are two dolomitized grains with only very fine twins in this sample. Dolomite can be primary but can also form by recrystallization from calcite. The fact that magnesium content in the dolomite is significantly less than 0.50 p.f.u. means this dolomite is (partly) recrystallized (Kaczmarek and Sibley, 2014). This needs magnesium-rich fluids, but the transformation from illite to muscovite releases significant amounts of magnesium (Van de Kamp, 2008). Dolomite is stronger than calcite (Jamison and Spang, 1976) and twin morphology does not have the same temperature dependence as calcite (Barber et al., 1981). The fact there are some deformation twins in the dolomite means the dolomitization took place at least before the last deformation phase, but possibly much earlier.

6.2.3 Carbonate blocks

Both carbonate blocks show stylolites and perpendicular veins of recrystallized carbonate. These features are probably related, as the stylolites form by pressure solution and the fluids responsible for this must escape. Cracks will form preferentially at right angles to the stylolites, which is clearly the case in the dolomitic AN16-007.

The calcite sample AN16-013 does not show the same amount of brittle deformation, but has more complex fracture and stylolite patterns. There certainly has been more than one direction of shortening during the lifetime of this block. It is also possible the block has rotated as it got incorporated in the mélange and one direction reflects the original compaction direction and the other is a shear-related foliation.

The fact that there are no twins in this sample indicates there were no ductile creep processes, but only brittle breaking of the rock causing the cracks that are now filled by new large grains due to dissolution-precipitation processes. That there are no twins in this block might be explained by dolomitization after the deformation, which would make the evidence of deformation disappear. It is also possible no twins were formed at all, as dolomite is much stronger. Unfortunately there is no compositional data from this sample, so there are no indications on whether this dolomite is primary or recrystallized.

6.3 Deformation mechanisms and temperature

Different deformation mechanisms are dominant at different temperatures and strain rates. Therefore, when a certain deformation mechanism is observed, this has implications for the deformation temperature. Another way of estimating paleotemperature is the mineral assemblage and the exact chemical composition of certain minerals. This section gives an overview of the different temperature ranges found and their implications.

6.3.1 Mineral assemblage

The absence of high pressure and temperature minerals places an upper bound on deformation temperature. The mineral assemblage of quartz, muscovite and chlorite found in the Gwna mélange (see Tab.1) is stable up to a temperature of 500-550°C. At higher temperatures it will transform into garnet and biotite (Bucher and Grapes, 2011).

The muscovite in the samples is mostly very fine grained, except for some larger grains in AN16-010. Muscovite can form by the reaction of illite to muscovite and quartz, the small amounts of illite make this a likely source for the muscovite. This reaction also releases magnesium, 0.81 MgO per muscovite molecule, which could be a magnesium source for the calcite to dolomite transition. The illite to muscovite transformation takes place over a temperature range of 190-500°C, but this occurs in two stages. Between 200 and 300°C, illite is replaced by very fine crystalline muscovite and at temperatures of 300-500°C, this is replaced by coarser muscovite grains (Van de Kamp, 2008). The very fine grainsize therefore suggests the muscovite in the Gwna mélange has not been subjected to temperatures much above 300°C.

6.3.2 Basalt alignment

The crystal alignment in basalt sample AN16-025 implies ductile deformation. Basalts have been observed in lab experiments to start deforming ductilely at temperatures above ∼800°C, but extrapolated to geological strain rates this may start at temperatures as low as 550 °C (Violay et al., 2012). In order to reach temperatures this high in a subduction zone with typical low geothermal gradients around 10-15 °C/km, the deformation should have occurred at unlikely depths over several hundreds of kilometers. These rocks have not been to these depths, so there has to be another explanation for the crystal alignment.

EDS measurements on the SEM showed the aligned minerals are muscovite crystals, which at low temperatures replaces illite, which replaces smectites (Van de Kamp, 2008). Potassium-rich smectites commonly form by seafloor alteration, where potassium and magnesium are taken from seawater (Melson and Thompson, 1973). This means the rock composition is not the one of a basalt any more, but the distinct pillow shape in outcrop ensures these were basalts upon the time of formation. The alignment of the muscovite minerals, which is a sheet silicate, makes shear displacement easy along the basal mica planes. The question when this alignment formed is therefore important, because if this alignment was present before incorporation in the subduction zone, it would make deformation of the basalt easier and may therefore cause deformation to localize in the basalt.

6.3.3 Quartz deformation

There are several types of indicators of crystal-plastic deformation in quartz in the samples. These include the observation of extinction bands (AN16-011),

elongated grains (AN16-009 and AN16-011), subgrains (AN16-009 and AN16-012) and recrystallized grains at the grain boundaries (AN16-012).

- extinction bands Several different types exist of what are here described as extinction bands, mainly distinguished by their width and the orientation relative to the crystallographic planes (Derez et al., 2015). Current research includes findings of extinction bands in the High-Ardenne slate belt, deformed under sub-greenschist conditions (Derez et al., 2016), like the Gwna Group. This research stresses that until more is known about the formation mechanisms of these structures, no interpretations about the deformation conditions can be made.

These deformation bands only occur in a few rounded grains, which makes it possible the extinction bands did not form in this sandstone, but in the protolith. The quartz does not come from the microcontinents, because these are made of ocean island basalts, so it must come from Gondwana, probably Amazonia, where also the zircons come from (section 3.1). Amazonia has a long history including many deformation events, and it is certainly possible the extinction bands formed in Amazonia before they were incorporated in the sandstones in the Gwna mélange.

- subgrains and elongated grains Temperature estimations for deformation mechanisms in quartz come from Stipp et al. (2002b), who describe cataclastic flow, bulging (BLG), subgrain rotation (SGR) and grain boundary migration (GBM) in the Tonale fault zone. This is a strike-slip shear zone, where the temperature gradient is constrained by various metamorphic mineral reactions and pressure is constant at 250-300 MPa (Fig.34). It is described as a natural laboratory for deformation of quartz, but samples are taken from quartz veins and grains therefore have no prior deformation history.

Compared to this study, the range of quartz deformation microstructures observed in the Gwna mélange samples have to be formed over a range of temperatures. According to Stipp et al. (2002b), the large elongated grains with irregular grain boundaries in samples AN16-009 and AN16-011 form at temperatures above 530°C, where grain boundary migration occurs. Subgrains like those in samples AN16-009 and AN16-012 form at temperatures of ∼490°C. The small recrystallized grains at the grain boundaries in AN16-012 form at ∼400°C, at the boundary between the bulging and subgrain formation regimes. The arrays of small grains cross-cutting larger grains indicate cataclastic flow, which occurs at temperatures below 280°C.

However, quartz deformation mechanisms are not solely dependent on temperature. To determine when dislocation creep mechanisms like subgrain formation become dominant, differential stress is also of importance, as are strain rate and water fugacity (Hirth and Tullis, 1992). What is more, the quartz grains are detrital and may therefore have inherited high dislocation densities from their source. It is known that quartz grains in deformed rocks of low metamorphic grades have higher dislocation densities than quartz crystals in veins (Blum

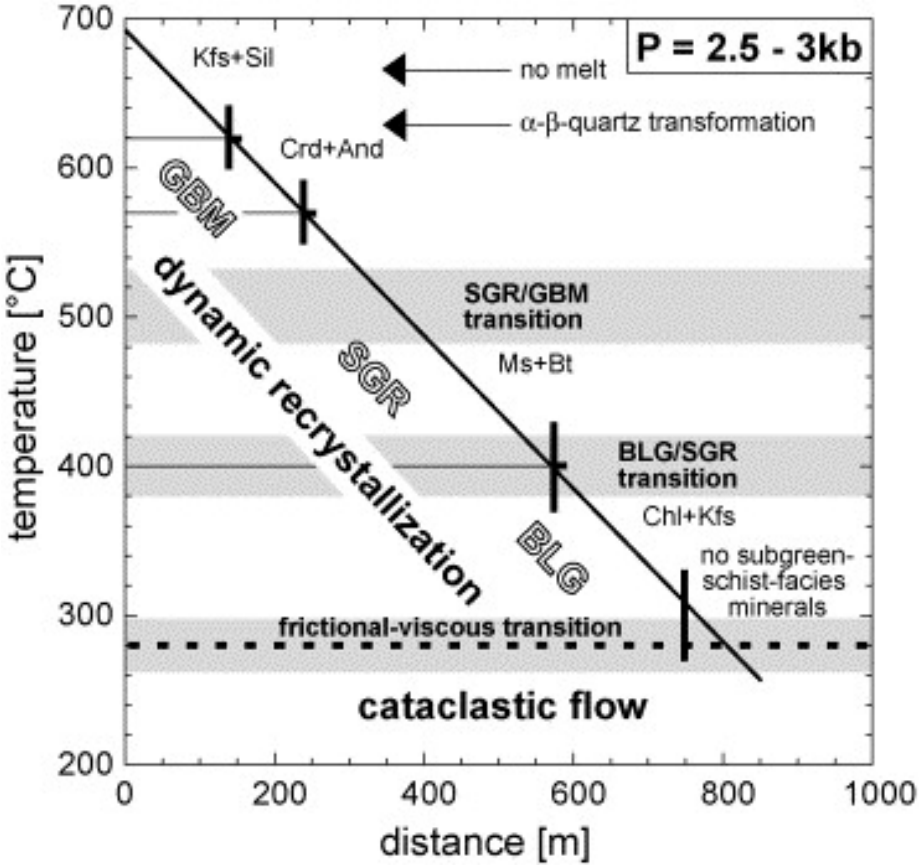

Figure 34: With increasing distance along the Tonale fault zone, the temperature decreases and deformation mechanism changes. From: Stipp et al. (2002b)

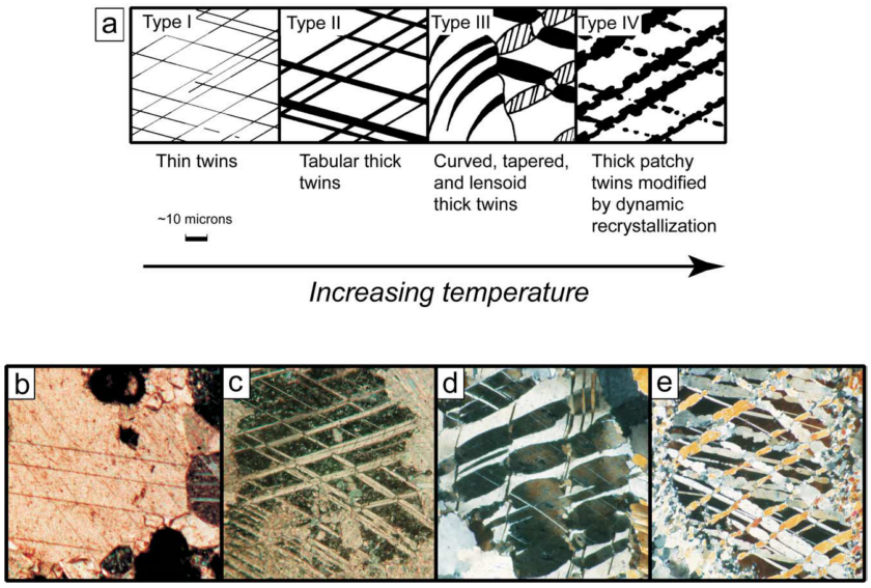

Figure 35: the type of twins that develop in calcite depends on deformation temperature. From: Ferrill et al. (2004)

et al., 1990). Although there are no studies that systematically investigate the effect of inherited dislocation density on dislocation creep mechanisms, the fact the amount of impurities and lattice defects influence the motion of dislocations through a crystal (Mitchell, 1975) suggests that the detrital grains of the Gwna mélange may have been easier to deform by dislocation creep than quartz in veins as described by Stipp et al. (2002b).

- pressure solution When a fluid phase is present, quartz may also deform by pressure solution. There are two different indications that pressure solution played a role in the deformation of the quartz-rich samples. Samples AN16-009, AN16-011 and AN16-012 exhibit grain-to-grain indentations, where quartz was dissolved at the stressed grain contact and precipitated at nearby low stress grain boundaries. Many quartz and carbonate-rich samples show solution seams (e.g. AN16-004, AN16-008 and AN16-022) and stylolites (AN16-007 and AN16-013), where quartz is dissolved and is transported out of the system so that residues of mica's and oxides are left behind .

Pressure solution in fine grained quartz at geological strain rates occurs at temperatures between 200 and 350°C, although it may continue up to higher temperatures and does not need high confining pressures. When temperatures become too high, or when there are no accessible fluids, Coble creep becomes an important mechanism (Mcclay, 1977).

6.3.4 Calcite twinning

Twinning is mainly observed in calcite veins in the basalt and in the calcite block, not in the dolomite block and in the dolomite in the hyaloclastite. This might be because the dolomitization occured after deformation, causing the deformation twins to disappear or because dolomite is stronger and twins were never formed. It is unlikely the matrix of the hyaloclastite was not deformed in the first place, because of the presence of sheared vesicles.

Deformation twins in calcite form at low temperatures and the amount of twinning depends on stress. The type of twinning however, depends on temperature. Below 170°C higher strains cause new thin twins to form, whereas at higher temperatures >200°C, twin lamellae grow thicker. Above temperatures of 250°C, dynamic recrystallization starts, causing irregular twin boundaries (Fig.35) (Ferrill et al., 2004).

Calcite is present in the basalt samples, the hyaloclastite and in the calcite block. In deformed basalt sample AN16-025, most twins are irregular and recrystallized. Two grains show thin twins, but these are with 36% MgO dolomitic. Undeformed basalt sample AN16-028 also shows curved irregular twins. The carbonate in hyaloclastite sample AN16-026 shows mainly untwinned dolomite. This all indicated deformation temperatures above 250°C. Although dynamic recrystallization might start at slightly lower temperatures in large monomineralic calcite grain, due to high dislocation densities, like the ones in the basalt samples.

The calcite in the block from Cemaes Bay, AN16-013, shows all kinds of twins. It is likely that deformation temperatures were >250°C and that most grains in this block have recrystallized afterwards. This could also explain the very elongated shape of the block in outcrop. In the larger grains that form vein-like structures, also thin twins are present. This means more deformation must have occurred after this recrystallization had ceased and the temperature had decreased to below 170°C.

6.3.5 Chlorite composition

As described in section 5.3.2, the chlorite formed at temperatures of about 230-270°C. The range reflects both inaccuracy in the geothermometers and measurements, as well as the differences in temperature over the timespan during which the chlorite was formed. The metamorphic chlorite within the rock and the hydrothermal chlorite in the veins and vesicles give similar formation temperatures. This indicates they were probably formed at the same time, although there are no visible cross-cutting relationships and it is possible they formed at different times at the same temperature.

6.3.6 Deformation temperature

All these different temperature indicators taken together indicate that the temperature during D1 was high enough for pressure solution in the quartz and calcite, so above 200°C.

Table 4: overview of estimated and measured deformation temperatures and their relative timing to the deformation events, see text for argumentation

method	temperature	D1	D2	D3
quartz -elongated grains	530°C		- - - - - -	
quartz -subgrains	490°C		- - - - - -	
quartz -recrytallized grains	400°C		- - - - - -	
quartz -pressure solution	200-350°C	———	———	
fine grained muscovite	200-300°C		———	———
chlorite	230-270°C		———	
calcite -recrystallization	250°C		———	
calcite -thin twins	170°C			———

During the main subduction mélange forming event D2, when the chlorite formed as well, temperatures were up to 270°C, as indicated by the chlorite geothermometer. The recrystallization in calcite also shows temperatures were at least higher than 250°C. Pressure solution causes geological strain rates at least up to temperatures of 350°C (Mcclay, 1977), although it may coexist with other deformation mechanisms up to much higher temperatures. The other quartz deformation mechanisms would indicate higher temperatures. However, the chlorite geothermometer is reliable for temperatures up to 400°C (Frimmel, 1997) and although individual measurement may not reflect peak metamorphic conditions, the fact that no single measurement gives a temperature above 300°C makes it unlikely deformation temperatures have been much higher. Combined with the very fine grained muscovite that has not recrystallized into larger, more stable grains, which also indicates the temperature has not been higher than ∼300°C for a significant amount of time. This means deformation temperature was likely around 270-280°C and the quartz subgrains and recrystallization must have occured in spite of this relatively low temperature.

Possible explanations for the formation of subgrains and recrystallization at these low temperatures might be hydrolytic weakening, as subduction zones usually contain significant amounts of water. Another possibility is the presence of relatively high amounts of pre-existing dislocations in the quartz, as they are detrital and were likely deformed before. There might even be a combined effect, as grains with high dislocation densities might be more prone to hydrolytic weakening.

During the last deformation phase D3 the spaced foliation formed. The nature of this foliation is unknown, but the fact that it was not visible in back-scatter electron images means it is not defined by a compositional variation. This means that the foliation was not formed by a temperature driven mineral reaction, which means there is no direct measure for temperature. However, recrystallized carbonate grains show twins that indicate deformation must have occured after recrystallization when temperatures had decreased to below 170°C. If this was during the last deformation event, this means this spaced

foliation formed at a similar temperature.

6.4 Implications for seismicity in a subduction zone

6.4.1 Seismicity

In order to have a seismically active zone, there has to be brittle deformation (see section 2.4). The few signs of seismic behaviour in the Gwna mélange are the broken blocks in sample AN16-008, the small microcracks in sample AN16-012 and the veins present in the quartz and carbonate blocks. The veins are not very abundant and their orientation suggest many of these are related to burial and are not formed in the subduction zone. The small microcracks and broken blocks are restricted to the quartz and may be sources for microseismicity, as described by Fagereng et al. (2014). Most of the deformation in the quartz blocks is by ductile processes and the carbonate blocks that are present are deformed by recrystallization, which is also an aseismic process.

6.4.2 Aseismicity

Wintsch et al. (1995) give two main explanations why fault zones can be aseismic, high fluid pressures or the presence of phyllosilicates, especially if they define a foliation. High fluid pressures are common in subduction zone settings, due to dehydration of the downgoing slab, and will lead to vein swarms (Sibson, 2013). There are no vein swarms in the studied samples, the veins that are present are generally perpendicular to the sedimentary layering and solution seams and are therefore most likely related to burial processes. This makes it unlikely fluid overpressures played an important role in the deformation of the Gwna mélange.

Phyllosilicates, like muscovite, can weaken fault zones if they are abundant enough and if they are aligned so that they form a continuous foliation. Muscovite was present in the basalt before it was incorporated in the subduction zone, because it is also present in the undeformed basalt. When the basalt is deformed, the muscovite forms a foliation inferring that the deformation was mostly along these minerals.

The sediment samples show large amounts of muscovite as well, along with amounts of quartz, apatite and oxide grains small enough to be completely embedded in a matrix of the mica. Pressure solution during the burial of the sediments caused solution seams that are depleted in quartz, or enriched in muscovite. This defines a foliation of micaceous minerals along which deformation is easy. Because deformation will localize in the easily deformable parts, the muscovite foliation present in all samples is important for the overall strength of the subduction zone.

6.4.3 Aseismic subduction zones

Around the world, there is a division between subduction zones that exhibit episodic seismic slip in the form of large (M_{max} >8.3) earthquakes and subduc-

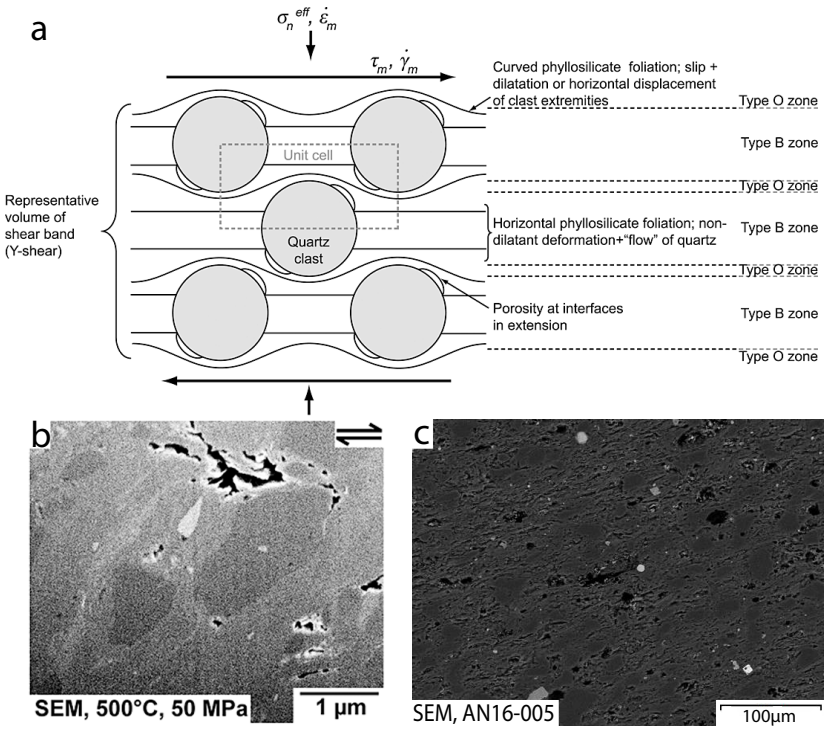

Figure 36: comparison of a) model microstructure as described by Den Hartog and Spiers (2014), b) experimentally deformed illite-quartz gouge (a+b from Den Hartog and Spiers (2014)) and c) naturally deformed muscovite-quartz subduction mélange matrix

tion zones that deform mostly by creep, with small- to medium-size earthquakes (Gao and Wang, 2014). These seismic subduction zones are capable of producing large earthquakes because of their smooth surface, which means that they can slip over large areas in one event (Bachmann et al., 2009). They are smooth because they do not have much topography like subducting seamounts or because there are large amounts of sediments present (Scholl et al., 2011). Rough subduction faults lead to deformation by creep at rates similar to plate movements rates and do not produce large earthquakes (Wang and Bilek, 2014).

The Gwna mélange consists of pillow basalts and sediments of a very young oceanic plate (<10 Ma, section 3.3), which means the amounts of sediments subducting were small. Determining the paleo-topography of the subducting plate is more difficult, but the stromatolitic limestones suggest stromatolites were abundant and may have formed seamounts, making the subduction interface of the Gwna mélange a rough surface. This fits with the observation of deformation by creep being dominant.

6.5 Modelling the Gwna mélange deformation

6.5.1 Matrix

Models for subduction zones that deform by creep assume a microstructure of quartz clasts embedded in a matrix of phyllosilicates (Fig.36a) (Fagereng and den Hartog, 2016). They combine frictional sliding on the phyllosilicate planes with deformation by pressure solution in the quartz clasts. Seismogenesis is controlled by the rate of pressure solution which counteracts the dilatation caused by slip along the anastomosing foliation (Den Hartog and Spiers, 2014). These models assume pressure solution in the quartz clasts and velocity-weakening, seismogenic behaviour when pressure solution is not fast enough. No other ductile deformation mechanisms are incorporated in these models.

The muscovite-rich matrix of the Gwna mélange closely resembles the conceptual model microstructure and the experimentally deformed illite-quartz gouges by Den Hartog and Spiers (2014) (Fig.36). The model predicts for illite gouges, deforming at steady plate boundary strain rates, that this model applies at temperatures above 100°C (Fagereng and den Hartog, 2016). Muscovite is similar to illite, but the different material constants can change this number slightly. The Gwna mélange was formed at temperatures above this critical value and since the microstructures are similar, this model applies for the matrix, including the single quartz grains in the matrix, but not the larger blocks.

6.5.2 Quartz blocks

The quartz blocks in the matrix did not deform by pressure solution only, therefore the model that applies for the matrix with single quartz grains in foliated muscovite, cannot be applied to the larger quartz blocks in a muscovite matrix. The quartz blocks that are present take many different shapes. Blocks in AN16-008 are small, internally undeformed angular blocks. Their small size and high matrix content made it possible to float along, rotate if necessary, but did not require any internal deformation. Other, larger blocks, like AN16-009, AN16-011 and AN16-012, do show internal deformation. These blocks were elongated in outcrop, which fits with their internal structure showing signs of ductile deformation. Microstructures include elongated grains, subgrain formation and recrystallization by bulging, which means both dislocation creep and dislocation glide mechanisms have played a role in deformation of the quartz. The question is why these mechanisms were favoured over pressure solution.

There are several key parameters that influence the deformation mechanisms. First of all, for pressure solution, a fluid phase is needed. The absence of accessible fluids would be an explanation for the lack of pressure solution. The quartz blocks have very low porosities, which could mean water would not get in to the quartz blocks. However, almost all grain boundaries contain muscovite. This would not only mean there is some water present in these hydrated minerals, they could also provide a fluid pathway and if the muscovite is formed by the reaction of illite, which also releases water, this means there was at least some

water present in the blocks. If there was no water present, the dominant deformation would be Coble creep, the dry equivalent of pressure solution, because at low temperatures the movement of vacancies is easier than the movement of dislocations, due to the higher activation energy of this last process (Wheeler, 1992).

Other parameters include temperature, of which the effect has already been explained, but this does not explain why there is a difference in dominant deformation mechanism between the matrix and the blocks, since the blocks have not been warmer than the matrix. Grainsize plays another important role, larger grains are more difficult to deform by pressure solution as the path from quartz source to sink is increased (Knipe, 1989). It might be the grainsize was too large for pressure solution and other mechanisms were favoured. To test this, flow laws for ductile creep and pressure solution can be compared. The mechanism yielding the highest strain rate will be the dominant deformation mechanism (Fig.37a). The flow law for ductile creep in the blocks is:

$$\sigma = exp(\frac{1}{n}(\frac{Q}{RT} + ln(\frac{\dot{\gamma}}{A}))) \tag{1}$$

in which n, Q and A are constants, for which values from Jaoul and Tullis (1984) are used, R is the universal gas constant and T is deformation temperature. There is no grainsize dependence, whereas the flow law for pressure solution in quartz, does depend on grainsize d. In the case of the dissolution reaction to be rate-controlling, which is the case in quartz (Niemeijer and Spiers, 2005), the flow law becomes:

$$\dot{\gamma} = A_s \frac{I}{d} \frac{\sigma\Omega}{RT} f(\phi) \tag{2}$$

in which A_s is a shape factor (2-10), I is the dissolution rate, Ω is the molar volume and f is a function of porosity ϕ.

Figure 37b shows that for a larger grainsize, the stress needed for ductile creep to occur decreases. It also shows that at the deformation temperature found (280°C) and the largest average grainsize (256$\pm$100μm, sample AN16-012), stresses have to reach unlikely values of several hundred MPa before the grainsize is too large for pressure solution to occur.

6.5.3 Stress and strain rate in the blocks

Strain rate is also important for deformation mechanisms in the quartz blocks. At high strain rates there will be brittle deformation instead of ductile deformation. The matrix surrounding these blocks mainly consist of muscovite. If the matrix surrounding the blocks is easy to deform, most displacement will occur in the matrix, the strain rate will be higher in the matrix then in the blocks. This increases the stress on the blocks, this stress can be measured and from this the strain rate can be calculated.

Stress can be estimated from recrystallized grainsize in quartz using the formula $\sigma_{\text{diff}} = KD^{-p}$ in which σ is differential stress in MPa, D is grainsize (equivalent area spherical diameter) in μm $\pm 1\sigma$ and K and p are theoretical

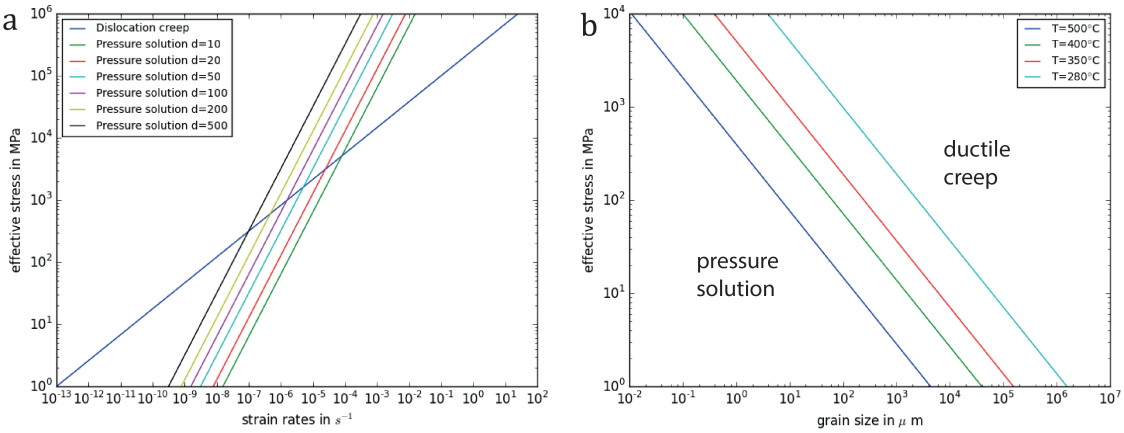

Figure 37: a) flow laws for ductile creep, which does not depend on grain size and for pressure solution, which does depend on grainsize d in μm (T=280°C), b) with increasing grainsize, the stress needed for switching to ductile creep decreases

Table 5: Differential stresses (MPa) calculated from recrystallized grainsize and subgrains

	recrystallized grains			subgrains		
	18±4.87			110±57.2		
	$-\sigma$	mean	$+\sigma$	$-\sigma$	mean	$+\sigma$
S&T	87.5	68.2	56.4	29.1	16.3	11.7
S&Tc	62.8	48.9	40.5	20.9	11.7	8.41
T	104.7	84.5	71.8	40.6	24.7	18.6
S	27.7	21.5	17.7	9.1	5.05	3.61

or empirical constants. Following Boutonnet et al. (2013) four different sets of constants are used. Only sample AN16-012 had measurable subgrains and recrystallized grains (Fig.25), but the amount of grains that could be measured is limited. These numbers are based on 41 measured recrystallized grains and only 19 measured subgrains. There are large differences between the four methods, so the values given in Tab.5 should be seen as rough estimates. The theoretical method by Twiss (1977) applies for subgrains, whereas the method by Shimizu (2008) applies to recrystallized grainsize. This gives a first order estimate for differential stress in the quartz blocks around 23 MPa.

Using the quartz-strain-rate-metry method described by Boutonnet et al. (2013), the differential stress σ_{diff} can be used to calculate strain rate in the blocks using the formula $\dot{\varepsilon} = A\sigma^n f_{H_2O}^m e^{Q/RT}$. Using the calculated differential stress of 23 MPa, a deformation temperature of 280°C and again using different sets of constants, the values given in Tab.6 are calculated. Boutonnet et al. (2013) have a reference way of calculating strain rate and find the flow laws by Paterson and Luan (1990) and Hirth et al. (2001) most accurate and favour the latter because it is constrained by experimental and natural data. However, this one depends on the water fugacity, which is unknown in our samples and had to be assumed, whereas the method by Paterson and Luan (1990) does not. Therefore this flow law is best to apply in this study, although the difference between the two flow laws is relatively small.

The strain rates in the quartz blocks obtained by this method are $< 10^{-29}$ s^{-1} and although there are many assumptions in these stress and strain rate calculations, these are very low. Strain rate ($\dot{\gamma}$) is a function of slip velocity (V) and width of the shear zone (w): $\dot{\gamma} = V/w$. This low strain rate would mean that if the deforming block was a meter thick, the slip velocity would be less than a nanometer per billion years. Geological strain rates in aseismic subduction zones are significantly higher. For example, estimated strain rates for the creeping northern Hikurangi margin are 10^{-11} to 10^{-9} s^{-1} (Fagereng and den Hartog, 2016). This is based on a subduction rate (V) of about 40 mm/year, which is about 10^{-9} m/s, divided over a shear zone width of 1-100 meters.

6.5.4 Stress and strain rate in the matrix

These low strain rates in the competent blocks are not surprising, considering strain rates are higher in the incompetent matrix (Fagereng and Sibson, 2010). As mentioned before, the matrix can be modeled using the method described by Den Hartog and Spiers (2014). This model is based on experiments where the strain rate is known, which can then be used to calculate shear stress. However, if the assumption is made that the maximum shear stress is half the differential stress, this can be used to estimate an upper bound to the strain rate.

The model describes a dilational and a non-dilational regime. The non-dilational regime is when pressure solution is fast enough to keep up with the deformation along the foliation planes and therefore no porosity is created. For dilational deformation the macroscopic shear stress τ_m must be higher than the

Table 6: strain rates calculated using different flow laws, for a differential stress of 23 MPa and a temperature of 280°C, f_{H_2O} is 17.5 MPa, corresponding to a depth of 10km

	Q	A	n	m	strain rate
	kJ mol^{-1}	$MPa^{-n}s^{-1}$	-	-	s^{-1}
Luan and Paterson (1992)	152	$4.00e^{-10}$	4	0	$4.92e^{-33}$
Paterson and Luan (1990)	135	$6.50e^{-08}$	3	0	$5.16e^{-29}$
Hirth et al. (2001)	135	$6.30e^{-12}$	4	1	$2.01e^{-30}$
Rutter and Brodie (2004)	242	$1.20e^{-04}$	3	1	$1.82e^{-44}$
Gleason and Tullis (1995)	223	$1.10e^{-04}$	4	0	$7.68e^{-41}$
Holyoke and Kronenberg (2010)	223	$5.10e^{-04}$	4	0	$3.56e^{-40}$

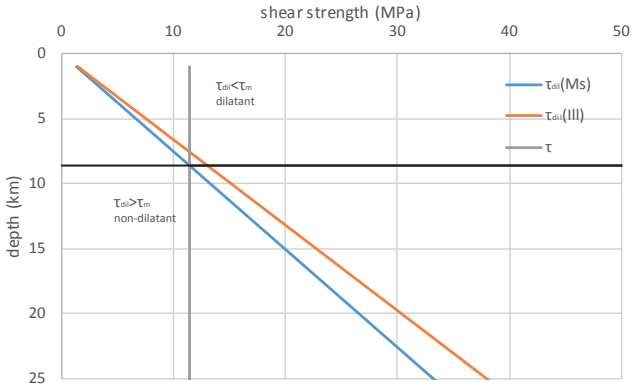

Figure 38: shear stress needed for dilatant deformation increases with depth, when it is lower than the macroscopic shear stress there will be dilatant deformation, when it is higher than the macroscopic shear stress there will be non-dilatant deformation

stress needed for dilatation τ_{dil}, which can be calculated using the following formula:

$$\tau_{dil} = \frac{\mu_{ph}(1 + \tan^2 \Psi_{fr})}{1 - \mu_{ph}^2 \tan^2 \Psi_{fr}} \sigma_n^{\text{eff}} \tag{3}$$

In which μ_{ph} is the friction coefficient of the phyllosilicate, which varies with temperature and strain, as described by Den Hartog et al. (2013). For the current deformation temperature of 280°C and high strains, this is 0.502, which is lower than the value for illite at this temperature (0.57, Den Hartog and Spiers (2014)). Ψ_{fr} is a geometrical factor to account for the inclination of the foliation, which again depends on grainsize, quartz fraction and quartz grain shape. σ_n^{eff} is the effective normal stress, which depends on fluid pressure factor $\lambda = \frac{P_f}{\sigma_n^{\text{eff}}}$ and depth. Using equation 3 in combination with the grain size of 20μm and assumed λ=0.9 allows for calculation of τ_{dil} over a range of depths.

The maximum macroscopic shear stress τ_m is half of differential stress, which was calculated above from the recrystallized grainsize in the blocks. This can be compared to the stress needed for dilatant deformation, as is done in Fig.38. The microstructures show low porosity and no brittlely deforming clasts, so deformation was in the non-dilational regime. For the estimated maximum macroscopic shear stress, there was dilational deformation at depth larger than 9 kilometers.

To calculate strain rate from shear stress, the assumption is made that the macroscopic shear stress (τ_m) is equal to shear stresses in the B-zone and O-zone (Fig.36a), so $\tau_m = \tau_B = \tau_O$. The shear stress in these two zones is a combination of shear stress along the foliation (τ_{ph}) and shear stress in the quartz (τ_{qtz-B} and τ_{qtz-O}). Knowing the macroscopic shear stress and calculation of τ_{ph} from the effective normal stress and the friction coefficient of muscovite, allows for the calculation of the shear stress in the quartz. With this shear stress known, the shear stress in the quartz in the B-zone (τ_{qtz-B}) and O-zone (τ_{qtz-O}) can be calculated using the following formulas:

$$\tau_B = \tau_{ph}(1 - \frac{A_{qtz-b}}{LD}) + \tau_{qtz-b}\frac{A_{qtz-b}}{LD} \tag{4}$$

$$\tau_O = \tau_{ph}(1 - \frac{A_{qtz-o}}{LD}) + \tau_{qtz-o}\frac{A_{qtz-b}}{LD} \tag{5}$$

In which A_{qtz-b}, A_{qtz-o} and L are geometrical constants, depending on grainsize D, porosity and quartz fraction. Porosity has to be lower than critical porosity, so it has to be lower than 1% and how much lower has no significant influence on the strain rate.

Knowing the shear stress in the quartz in both zones makes it possible to calculate the strain rates in both parts, using:

$$\dot{\gamma}_{qtz-b} = \frac{AI\tau_{qtz-b}\Omega}{RT}\frac{D-2}{D(D-x)} \tag{6}$$

$$\dot{\gamma}_{qtz-o} = \frac{2I\tau_{qtz-o}\Omega}{RT}\frac{1}{\sqrt{Dx - x^2}} \tag{7}$$

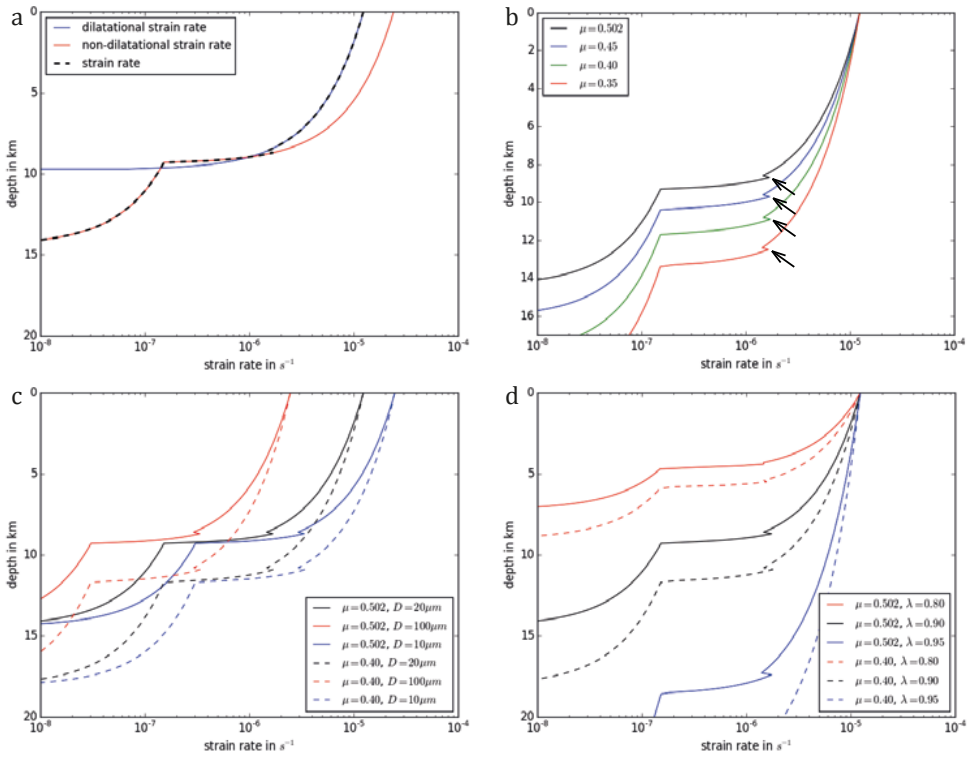

Figure 39: strain rate with depth: a) dilatational strain rate and non-dilatational strain rate, transition is based on depth where τ_{dil} is overcome by τ_m, b) sensitivity of strain rate to changes in friction coefficient μ (λ=0.90, D=20μm), arrows point to the little indent which marks the change from dilational to non-dilational deformation c) sensitivity of strain rate to changes in grain size D (λ=0.90), d) sensitivity of strain rate to changes in fluid pressure factor λ (D=20μm)

The total strain rate $\dot{\gamma}_m$ is the sum of the strain rates in the b- and o-zone, $\dot{\gamma}_m = \dot{\gamma}_{qtz-b} + \dot{\gamma}_{qtz-o}$. During non-dilational deformation, strain rates in the o-zone can not become negative. This causes a sudden change in the non-dilational strain rate, visible in Figure 39.

Using this approach to the current value for maximum macroscopic shear stress 11.5 MPa, combined with a deformation temperature of 280°C, grain size of 20μm, porosity of 0.5%, λ is 0.9 and an estimated quartz fraction of 0.4, the macroscopic strain rates vary between 10^{-6} and 10^{-8} s^{-1} for depths of 9-14 km (Fig.39a). The strain rates found are higher than the estimated values of 10^{-10}, but this is an upper bound, using the maximum macroscopic shear stress.

At depths larger than 14 km, deformation is not possible at the calculated maximum shear stress τ_m and the constants used. The frictional strength of

sliding along the phyllosilicates depends on effective normal stress and with increasing depth, this becomes larger than the value for shear stress calculated above. This would mean that τ_{qtz-b} would have to become negative, leading to negative strain rates. This is an effect of keeping the shear stress fixed and taking the calculations to depths that are unrealistic for the current deformation and indicates up to which depth deformation is possible at the shear stress used.

Limitations of this model are the uncertainties in many constants. The value given for friction coefficient μ (0.502), is measured in lab experiments using aggregates. Sliding along the basal phyllosilicate (001) planes causes friction to be much lower, about half of the friction coefficient of a powder (Kawai et al., 2015). Since the muscovite in the mélange matrix is partly aligned, it is likely there is some sliding along the basal planes. This means the friction coefficient might be lower than the measured 0.502. Figure 39b shows that a lower friction coefficient mainly influences the depth at which the transition from dilational to non-dilational occurs. Strain rates for the range over which there is non-dilational deformation remain similar. Grainsize variations do not cause a change in depth for non-dilational deformation, but do cause significant differences in strain rate (Fig.39c). An average grain size of 20μm was measured in the matrix, but variations between 10 and 100μm cause a difference in strain rate of about an order of magnitude. Possibly the most uncertain of all is the fluid pressure, which has the largest effect. Similar to the friction coefficient, it mainly causes variation in depth, rather than in strain rate. If deformation depth was known, this could provide insight in values of these constants.

6.5.5 Combined model

In the end, the total rheological behaviour of the rock is governed by both the weak matrix and the strong blocks. Handy et al. (1999) give ways of calculating whole rock strength and strain rate from two phases. In the Gwna mélange, both the quartz blocks and the matrix are deforming by viscous mechanisms, therefore the following formula applies:

$$\tau_r = \tau_w \phi_w^{-1/\tau_c} + \tau_s (1 - \phi_w^{-1/\tau_c}) \tag{8}$$

In which τ_r is the shear strength of the whole rock, τ_s and τ_r are the shear strengths of the strong (quartz) and weak (matrix) phases, respectively, ϕ_w is the volume fraction of the weak phase and τ_c is the viscous strength contrast. This viscous strength contrast is the ratio between the reference shear strengths of the strong and the weak phase, $\tau_c = \frac{\tau_{sr}}{\tau_w r}$. This means the shear strength of the material at the macroscopic strain rate $\dot{\gamma}_r$. Using the similarity to the northern Hikurangi margin, the reference strain rate is estimated to be $10^{-10} s^{-1}$.

The quartz is deforming by ductile creep and follows the flow law in equation (1). The weak matrix is deforming in the way described by the model, and using $\dot{\gamma}_r$, the shear stress in the matrix can be calculated, after which the strength contrast τ_c is known.

With these, the shear strain rates in the weak and strong phase can be

calculated, using:

$$\dot{\gamma}_w = \dot{\gamma}_r \phi_w^{-1/\tau_c} \tag{9}$$

and

$$\dot{\gamma}_s = \dot{\gamma}_r (1 - \phi_w^{1-(1/\tau_c)})/(1 - \phi_w) \tag{10}$$

These shear strain rates are then used to calculate the shear stresses in the weak and strong phase.

Using the reference strain rate of $10^{-10}s^{-1}$ and a flow law for dislocation creep in quartz for the blocks and using the model for the matrix described above to calculate the strength of the matrix, the strength contrast found is $\tau_c = 3466$. The corresponding strain rates are $\dot{\gamma}_w = 1.43 * 10^{-10}s^{-1}$ and $\dot{\gamma}_s = 3.43 * 10^{-14}s^{-1}$, for the weak matrix and the strong quartz blocks, respectively.

6.5.6 Comparison to real values

Real values for strain rates will probably be less extreme than calculated. In the quartz blocks, strain rates from recrystallized grainsize may have been higher than the calculated $5 * 10^{-29}s^{-1}$ if water and preexisting high dislocation densities helped the dislocation creep process. On the other hand, the strain rate in the matrix, that was calculated to be $1.3 * 10^{-7}s^{-1}$, is an upper bound and real strain rates in the matrix were lower. In principle, the method of Handy et al. (1999) could be used to calculate the real strain rate and competence contrast from these two strain rates. However, the difference is too large, there are no real solutions to these equations because the competence contrast would have to be infinitely large.

The strain rate in the quartz blocks must be significantly higher to get realistic values. If the strain rate in the quartz would be ten orders of magnitude faster, $5 * 10^{-19}s^{-1}$, the strength contrast would have to be $2.1 * 10^{11}$, so roughly 8 orders of magnitude higher than found by using the reference strain rate. The macroscopic strain rate is largely influenced by the strain rate in the matrix and in this scenario it would be $9.2 * 10^{-8}$.

This strain rate is still higher than the estimated 10^{-11}-10^{-9}, but this can be the result of more localized deformation in a shear zone that was thinner than 1-100m. To reach strain rates of 10^{-7}-10^{-8} and assuming the subduction rate of the Gwna mélange was similar to the northern Hikurangi margin at about 40 mm/year, the shear zone thickness must have been 1-10 cm. This fits with the localized zones that were observed at both Llandwyn Island and Cemaes Bay.

So to explain the aseismicity, this means that although the strain rate found by applying the model for the matrix is an upper bound, strain rates in the mélange matrix can be high enough to keep up with plate boundary subduction rates. This suggests that subduction mélanges can deform aseismically if the amount of matrix is high enough.

It should be mentioned that this only considers deformation in the mélange. It has been suggested before that deformation localizes along the upper boundary of the mélange (Wakabayashi and Rowe, 2015). This is also where the pseudotachylites that are found in mélanges are located (Kimura et al., 2012).

There is no localized shear zone found as upper boundary of the Gwna mélange, instead it is unconformably overlain by Ordovician sediments (Wood, 2012). This does not mean there was no roof thrust present during deformation, but makes it impossible to say whether or not deformation localized on the upper boundary. It may be that although the mélange is capable of deforming aseismically, it does not prevent earthquakes happening along the roof thrust, which can migrate into the mélange, but there is no evidence for (or against) it.

6.6 General implications

The main findings of this research concern the rheology of certain lithologies. First of all, the basalt, which is often considered a strong rock, at least stronger than the sediments, was easily deformed in this subduction mélange. This is because the composition is changed to consist mostly of phyllosilicates, in this case muscovite. The muscovite in the basalt has a composition that indicates formation in the subduction zone, but it is likely the muscovite formed from illite that was formed on the sea-floor. Basalts do not contain large amounts of potassium and seawater is the likely source for the enrichment in this element that is needed to form these minerals. If the formation of illite or muscovite is common on modern-day sea-floors, this means at least the upper layer of the basalts should be considered a mechanically weak and easy to deform layer.

The quartz blocks in the matrix were thought to deform seismically, causing tremor and slow slip or very low frequency earthquakes (see section 2.4). There are signs of compaction by pressure solution, as has been reported in other subduction mélanges, but there are no signs of brittle deformation. Instead the microstructures indicate dislocation creep to have occurred, although temperatures found ($\sim$280°C) were thought to be too low for these ductile deformation mechanisms. Quartz must be weaker than is currently believed, possibly because experiments and natural data are limited to undeformed quartz, whereas sedimentary quartzites consist of grains that may have experienced earlier deformation in their source, causing imperfections in the grains. Water content may also play a role and it is possible there is a combined effect.

What this ductile behaviour shows us, is that it is possible to have aseismically deforming subduction mélanges. If the amount of phyllosilicate-rich mélange matrix is high enough, strain rates in the matrix can keep up with subduction zone convergence rates. The strength contrast with the (quartz) blocks is large and the blocks are deforming slowly.

6.7 Suggestions for further research

- First of all, more research should be focused on how representative the numbers in this study are. Most values for strain rates and stresses are based on a very limited number of subgrainsize and recrystallized grainsize measurements.

- Irrespective of what these numbers say, this research indicates there were

dislocation creep mechanisms active at relatively low temperatures. Further research should focus on reasons why this occurs and how representative lab experiments are for naturally deformed quartz. Suggested reasons for the quartz deforming this way are the effect of starting dislocation density and water, further research is needed to tell whether these effects indeed play a role.

- This research does also not answer the question why the quartz is not deforming in brittle ways, as is observed in other subduction mélanges. Since the quartz is often held responsible for seismicity in subduction zones, it should be investigated why and under what circumstances this brittle and seismic or ductile and aseismic deformation occurs.

- Basalts in this study were found to be weak due to high amounts of muscovite. It should be investigated under what circumstances and up to which depths this happens and if this is also occurs in modern-day subduction zones, or that this might be limited to the warmer, more Mg-rich pre-Cambrian ocean floor.

- Last of all, there is the question how important the roof thrust is in subduction complexes. Is it possible there was no roof thrust to the Gwna mélange and that all deformation was taken up by the mélange, or do all subduction zones need a roof thrust? If so, how much of the deformation occurs on the roof thrust and does slip have to be seismic?

7 Conclusions

1. The Gwna mélange shows evidence of at least three deformation phases: vertical shortening during sediment accumulation on the seafloor (D1), causing layer-parallel solution seams; oblique shortening during subduction and mélange formation (D2), causing oblique solution seams and shear displacement along pre-existing solution seams; and late-stage shortening (D3) causing a spaced foliation.

2. Deformation mechanisms during subduction are different in the mélange matrix than in the quartz blocks. The mélange matrix deforms by frictional sliding over the abundant muscovite phyllosilicate planes, which are more aligned due to the earlier pressure solution compaction, in combination with pressure solution in single quartz grains present in the matrix. The blocks deform by ductile creep processes, despite relatively low temperatures of $\sim$280°C.

3. Deformation in the matrix was aseismic and deformation in the blocks was mostly aseismic, except for veins that may also be linked to earlier pressure solution, small angular blocks and micro-cracks.

4. The basalt acts as weak matrix rather than as strong blocks, which can be explained by the large amounts of phyllosilicates present in the basalt.

5. The competence contrast between the blocks and the matrix is large, causing differences between strain rates in the blocks and the matrix of several orders of magnitude. Macroscopic strain rate is mainly governed by the strain rate in the weak matrix and with abundant phyllosilicates, aseismic frictional sliding can reach rates high enough to allow constant creep, without the need for seismic events.

References

Aharonov, E. and Katsman, R. (2009). Interaction between pressure solution and clays in stylolite development: insights from modeling. *American Journal of Science*, 309(7):607–632.

Asanuma, H., Okada, Y., Fujisaki, W., Suzuki, K., Sato, T., Sawaki, Y., Sakata, S., Yamamoto, S., Hirata, T., Maruyama, S., and Windley, B. F. (2015). Reconstruction of ocean plate stratigraphy in the Gwna Group, NW Wales: Implications for the subduction-accretion process of a latest Proterozoic trench-forearc. *Tectonophysics*, 662:195–207.

Bachmann, R., Oncken, O., Glodny, J., Seifert, W., Georgieva, V., and Sudo, M. (2009). Exposed plate interface in the European Alps reveals fabric styles and gradients related to an ancient seismogenic coupling zone. *Journal of Geophysical Research: Solid Earth*, 114(5):1–23.

Barber, A. J. and Max, M. D. (1979). A new look at the Mona Complex (Anglesey, North Wales). *Journal of the Geological Society*, 136(4):407–432.

Barber, D. J., Heard, H. C., and Wenk, H. R. (1981). Deformation of dolomite single crystals from 20-800 C. *Physics and Chemistry of Minerals*, 7(6):271–286.

Blum, A. E., Yund, R. A., and Lasaga, A. C. (1990). The effect of dislocation density on the dissolution rate of quartz. *Geochimica et Cosmochimica Acta*, 54(2):283–297.

Boutonnet, E., Leloup, P. H., Sassier, C., Gardien, V., and Ricard, Y. (2013). Ductile strain rate measurements document long-term strain localization in the continental crust. *Geology*, 41(8):819–822.

Bucher, K. and Grapes, R. (2011). *Petrogenesis of Metamorphic Rocks*. Springer.

Cathelineau, M. (1988). Cation site occupancy in Chlorite and Illites as a function of temperature. *Clay minerals*, 23(4):471–485.

Cloos, M. and Shreve, R. L. (1988). Subduction-channel model of prism accretion, melange formation, sediment subduction, and subduction erosion at convergent plate margins: 1. Background and description. *Pure and Applied Geophysics PAGEOPH*, 128(3-4):455–500.

Cloos, M. and Shreve, R. L. (1996). Shear-zone thickness and the seismicity of Chilean- and Marianas-type subduction zones. *Geology*, 24(2):107–110.

Collins, A. S. and Buchan, C. (2004). Provenance and age constraints of the South Stack Group, Anglesey, UK: U-Pb SIMS detrital zircon data. *Journal of the Geological Society*, 161(5):743–746.

Cowan, D. S. (1982). Deformation of partly dewatered and consolidated Franciscan sediments near Piedras Blancas Point, California. *Geological Society, London, Special Publications*, 10(1):439–457.

Cowan, D. S. (1985). Structural styles in Mesozoic and Cenozoic mélanges in the western Cordillera of North America. *Geological Society of America Bulletin*, 96(4):451–462.

Dallmeyer, R. D. and Gibbons, W. (1987). The age of blueschist metamorphism in Anglesey, North Wales: evidence from 40Ar/39Ar mineral dates of the Penmynydd schists. *Journal of the Geological Society*, 144(6):843–850.

de Caritat, P., Hutcheon, I., and Walshe, J. L. (1993). Chlorite geothermometry: A review. *Clays and Clay Minerals*, 41(2):219–239.

Den Hartog, S. A. M., Niemeijer, A. R., and Spiers, C. J. (2013). Friction on subduction megathrust faults: Beyond the illite-muscovite transition. *Earth and Planetary Science Letters*, 373:8–19.

Den Hartog, S. A. M. and Spiers, C. J. (2014). A microphysical model for fault gouge friction applied to subduction megathrusts. *Journal of Geophysical Research: Solid Earth*, 119(2):1510–1529.

Derez, T., Pennock, G., Drury, M., and Sintubin, M. (2015). Low-temperature intracrystalline deformation microstructures in quartz. *Journal of Structural Geology*, 71:3–23.

Derez, T., Pennock, G., Drury, M., and Sintubin, M. (2016). Three sets of crystallographic sub-planar structures in quartz formed by tectonic deformation. *Earth and Planetary Science Letters*, 442:157–161.

Fagereng, Å. and den Hartog, S. A. M. (2016). Subduction megathrust creep governed by pressure solution and frictionalviscous flow. *Nature Geoscience*, 1(December).

Fagereng, Å. and Ellis, S. (2009). On factors controlling the depth of interseismic coupling on the Hikurangi subduction interface, New Zealand. *Earth and Planetary Science Letters*, 278(1-2):120–130.

Fagereng, Å., Hillary, G. W. B., and Diener, J. F. A. (2014). Brittle-viscous deformation, slow slip, and tremor. *Geophysical Research Letters*, 41(12):4159–4167.

Fagereng, Å. and Sibson, R. H. (2010). Mélange rheology and seismic style. *Geology*, 38(8):751–754.

Ferrill, D. A., Morris, A. P., Evans, M. A., Burkhard, M., Groshong, R. H., and Onasch, C. M. (2004). Calcite twin morphology: A low-temperature deformation geothermometer. *Journal of Structural Geology*, 26(8):1521–1529.

Festa, A., Dilek, Y., Pini, G. A., Codegone, G., and Ogata, K. (2012). Mechanisms and processes of stratal disruption and mixing in the development of mélanges and broken formations: Redefining and classifying mélanges. *Tectonophysics*, 568-569:7–24.

Festa, A., Pini, G. A., Dilek, Y., and Codegone, G. (2010). Mélanges and mélange-forming processes: a historical overview and new concepts. *International Geology Review*, 52(10-12):1040–1105.

Frimmel, H. E. (1997). Chlorite Thermometry in the Witwatersrand Basin: Constraints on the Paleoproterozoic Geotherm in the Kaapvaal Craton, South Africa. *Journal of Geology*, 105:601–615.

Gao, X. and Wang, K. (2014). Strength of stick-slip and creeping subduction megathrusts from heat flow observations. *Science*, 345(6200):1038–1041.

Gleason, G. C. and Tullis, J. (1995). A flow law for dislocation creep of quartz aggregates determined with the molten salt cell. *Tectonophysics*, 247:1–23.

Greenly, E. (1919). *The Geology of Anglesey (Volume 1)*.

Grigull, S., Krohe, A., Moos, C., Wassmann, S., and Stöckhert, B. (2012). "Order from chaos": A field-based estimate on bulk rheology of tectonic mélanges formed in subduction zones. *Tectonophysics*, 568-569:86–101.

Guidotti, C. V., Sassi, F. P., Comodi, P., Zanazzi, P. F., and Blencoe, J. G. (2000). The contrasting responses of muscovite and paragonite to increasing pressure: Petrological implications. *Canadian Mineralogist*, 38(3):707–712.

Handy, M. R., Wissing, S. B., and Streit, L. E. (1999). Frictional-viscous flow in mylonite with varied bimineralic composition and its effect on lithospheric strength. *Tectonophysics*, 303(1-4):175–191.

Hayman, N. W. and Lavier, L. L. (2014). The geologic record of deep episodic tremor and slip. *Geology*, 42(3):195–198.

Hickman, S. H. and Evans, B. (1995). Kinetics of pressure solution at halite-silica interfaces and intergranular clay films. *Journal of Geophysical Research-Solid Earth*, 100(B7):13113–13132.

Hirth, G., Teyssier, C., and Dunlap, W. J. (2001). An evaluation of quartzite flow laws based on comparisons between experimentally and naturally deformed rocks. *International Journal of Earth Sciences*, 90(1):77–87.

Hirth, G. and Tullis, J. (1992). Dislocation creep regimes in quartz aggregates. *Journal of Structural Geology*, 14(2):145–159.

Holyoke, C. W. and Kronenberg, A. K. (2010). Accurate differential stress measurement using the molten salt cell and solid salt assemblies in the Griggs apparatus with applications to strength, piezometers and rheology. *Tectonophysics*, 494(1-2):17–31.

Horák, J. M. and Evans, J. a. (2011). Early Neoproterozoic limestones from the Gwna Group, Anglesey. *Geological Magazine*, 148(01):78–88.

Hsü, K. J. (1968). Principles of Mélanges and Their Bearing on the Franciscan-Knoxville Paradox. *Geological Society of America Bulletin*, 79(August):1063–1074.

Hsü, K. J. (1974). Melanges and their distinction from olistostromes. pages 321–333.

Ikari, M. J., Niemeijer, A. R., Spiers, C. J., Kopf, A. J., and Saffer, D. M. (2013). Experimental evidence linking slip instability with seafloor lithology and topography at the Costa Rica convergent margin. *Geology*, 41(8):891–894.

Jamison, W. R. and Spang, J. H. (1976). Use of calcite twin lamellae to infer differential stress. *Bulletin of the Geological Society of America*, 87(6):868–872.

Jaoul, O. and Tullis, J. (1984). The effect of varying water contents on the creep behaviour of heavitree quartzite. *Journal of Geophysical Research*, 89(B6):4298–4312.

Jiang, W.-T., Peacor, D. R., and Buseck, P. R. (1994). Chlorite Geothermometry? - Contamination and Apparent Octahedral Vacancies. *Clay and Clay Minerals*, 42(5):593–605.

Kaczmarek, S. E. and Sibley, D. F. (2014). Direct physical evidence of dolomite recrystallization. *Sedimentology*, 61(6):1862–1882.

Kawai, K., Sakuma, H., Katayama, I., and Tamura, K. (2015). Frictional characteristics of single and polycrystalline muscovite and influence of fluid chemistry. *Journal of Geophysical Research B: Solid Earth*, 120(9):6209–6218.

Kawai, T., Windley, B. F., Terabayashi, M., Yamamoto, H., Isozaki, Y., and Maruyama, S. (2008). Neoproterozoic glaciation in the mid-oceanic realm: An example from hemi-pelagic mudstones on Llanddwyn Island, Anglesey, UK. *Gondwana Research*, 14(1-2):105–114.

Kawai, T., Windley, B. F., Terabayashi, M., Yamamoto, H., Maruyama, S., and Isozaki, Y. (2006). Mineral isograds and metamorphic zones of the Anglesey blueschist belt, UK: Implications for the metamorphic development of a Neoproterozoic subduction-accretion complex. *Journal of Metamorphic Geology*, 24(7):591–602.

Kawai, T., Windley, B. F., Terabayashi, M., Yamamoto, H., Maruyama, S., Omori, S., Shibuya, T., Sawaki, Y., and Isozaki, Y. (2007). Geotectonic framework of the Blueschist Unit on Anglesey-Lleyn, UK, and its role in the development of a Neoproterozoic accretionary orogen. *Precambrian Research*, 153(1-2):11–28.

Kimura, G., Kitamura, Y., Hashimoto, Y., Yamaguchi, A., Shibata, T., Ujiie, K., and Okamoto, S. (2007). Transition of accretionary wedge structures around the up-dip limit of the seismogenic subduction zone. *Earth and Planetary Science Letters*, 255(3-4):471–484.

Kimura, G., Yamaguchi, A., Hojo, M., Kitamura, Y., Kameda, J., Ujiie, K., Hamada, Y., Hamahashi, M., and Hina, S. (2012). Tectonic mélange as fault rock of subduction plate boundary. *Tectonophysics*, 568-569:25–38.

Kitamura, Y. and Kimura, G. (2012). Dynamic role of tectonic mélange during interseismic process of plate boundary mega earthquakes. *Tectonophysics*, 568-569:39–52.

Kitamura, Y., Sato, K., Ikesawa, E., Ikehara-Ohmori, K., Kimura, G., Kondo, H., Ujiie, K., Onishi, C. T., Kawabata, K., Hashimoto, Y., Mukoyoshi, H., and Masago, H. (2005). Mélange and its seismogenic roof décollement: A plate boundary fault rock in the subduction zone - An example from the Shimanto Belt, Japan. *Tectonics*, 24(5):1–15.

Knipe, R. J. (1989). Deformation mechanisms - recognition from natural tectonites. *Journal of Structural Geology*, 11(1/2):127–146.

Kranidiotis, P. and MacLean, W. H. (1987). Systematics of chlorite alteration at the Phelps Dodge massive sulfide deposit, Matagami, Quebec. *Economic Geology*, 82(7):1898–1911.

Luan, F. C. and Paterson, M. S. (1992). Preparation and Deformation of Synthetic Aggregates of Quartz. *Journal of Geophysical Research-Solid Earth*, 97(B1):301–320.

Maruyama, S., Kawai, T., and Windley, B. F. (2010). Ocean plate stratigraphy and its imbrication in an accretionary orogen : the Mona Complex , Anglesey Lleyn , Wales , UK. *Geological Society of London*, 338:55–75.

Mcclay, K. R. (1977). Pressure solution and Coble creep in rocks and minerals : a review. *Journal of the Geological Society*, 134:57–70.

Melson, W. G. and Thompson, G. (1973). Glassy abyssal basalts, atlantic sea floor near st. paul's rocks: Petrography and composition of secondary clay minerals. *Bulletin of the Geological Society of America*, 84(2):703–716.

Mitchell, J. B. (1975). Imperfections and Microstructure. *Metallography*, 8:5–70.

Niemeijer, A. R. and Spiers, C. J. (2005). Influence of phyllosilicates on fault strength in the brittle-ductile transition: insights from rock analogue experiments. *Geological Society, London, Special Publications*, 245(1):303–327.

Palin, R. M. and White, R. W. (2016). Emergence of blueschists on Earth linked to secular changes in oceanic crust composition. *Nature Geoscience*, 9(January):60.

Passchier, C. W. and Trouw, R. A. J. (1996). *Microtectonics*. Springer.

Paterson, M. S. and Luan, F. C. (1990). Quartzite rheology under geologic conditions. *Geological Society, London, Special Publications*, (54):299–307.

Pearce, J. A., Lippard, S. J., and Roberts, S. (1984). Characteristics and tectonic significance of supra-suprasubduction zone ophiolites. *Geological Society Special Publication*, 16:74–94.

Phillips, E. (1991). The lithostratigraphy, sedimentology and tectonic setting of the Monian Supergroup, western Anglesey, North Wales. *Journal of the Geological Society*, 148(6):1079–1090.

Pollock, J. C., Hibbard, J. P., and Staal, C. R. V. (2012). A paleogeographical review of the peri-Gondwanan realm of the Appalachian orogen. *Canadian Journal of Earth Sciences*, 49(November):259–288.

Pollock, J. C., Hibbard, J. P., and Sylvester, P. J. (2009). Early Ordovician rifting of Avalonia and birth of the Rheic Ocean: U-Pb detrital zircon constraints from Newfoundland. *Journal of the Geological Society*, 166(3):501–515.

Railsback, L. B. (1993). Lithologic controls on morphology of pressure-dissolution surfaces (stylolites and dissolution seams) in Paleozoic carbonate rocks from the mideastern United States. *Journal of Sedimentary Research*, 63(3):513–522.

Raymond, L. A. (1975). Tectonite and Melange A Distinction. *Geology*, (2):7–9.

Raymond, L. A. (1984). Classification of melanges. *Geological Society of America, Special Paper*, 198:7–20.

Rowe, C. D., Moore, J. C., and Remitti, F. (2013). The thickness of subduction plate boundary faults from the seafloor into the seismogenic zone. *Geology*, 41(9):991–994.

Ruff, L. J. (1989). Do trench sediments affect great earthquake occurrence in subduction zones? *Pure and applied geophysics*, 129(1-2):263–282.

Rutter, E. H. (1976). The kinetics of rock deformation by pressure solution. *Philosophical Transactions of the Royal Society of London*, A(283):203–219.

Rutter, E. H. and Brodie, K. H. (2004). Experimental grain size-sensitive flow of hot-pressed Brazilian quartz aggregates. *Journal of Structural Geology*, 26(11):2011–2023.

Saito, T., Uno, M., Sato, T., Fujisaki, W., Haraguchi, S., bing Li, Y., Sawaki, Y., Yamamoto, S., and Maruyama, S. (2015). Geochemistry of accreted metavolcanic rocks from the Neoproterozoic Gwna Group of Anglesey-Lleyn, NW Wales, U.K.: MORB and OIB in the Iapetus Ocean. *Tectonophysics*, 662:243–255.

Sato, T., Sawaki, Y., Asanuma, H., Fujisaki, W., Okada, Y., Maruyama, S., Isozaki, Y., Shozugawa, K., Matsuo, M., and Windley, B. F. (2015). Redox condition of the late Neoproterozoic pelagic deep ocean: 57Fe Mössbauer analyses of pelagic mudstones in the Ediacaran accretionary complex, Wales, UK. *Tectonophysics*, 662:472–480.

Scholl, D. W., Kirby, S. H., and von Huene, R. (2011). Exploring a link between great and giant megathrust earthquakes and relative thickness of sediment and eroded debris in the subduction channel to roughness of subducted relief. *American Geophysical Union, Fall Meeting 2011, abstract #T14-B01.*

Shimizu, I. (2008). Theories and applicability of grain size piezometers: The role of dynamic recrystallization mechanisms. *Journal of Structural Geology*, 30(7):899–917.

Shreve, R. L. and Cloos, M. (1986). Dynamics of Sediment Subduction, Melange Formation, and Prism Accretion. *Journal of Geophysical Research-Solid Earth*, 91(B10):10229–10245.

Sibson, R. H. (2013). Stress switching in subduction forearcs: Implications for overpressure containment and strength cycling on megathrusts. *Tectonophysics*, 600:142–152.

Silver, E. A. and Beutner, E. C. (1980). Melanges. *Geology*, 8:32–34.

Simpson and Schmid (1983). An evaluation of criteriea to deduce the sense of movement. *Geological Society of America Bulletin*, 94(11):1281–1288.

Stipp, M., Stunitz, H., Heilbronner, R., and Schmid, S. M. (2002a). Dynamic recrystallization of quartz: correlation between natural and experimental conditions. *Geological Society, London, Special Publications*, 200(1):171–190.

Stipp, M., Stünitz, H., Heilbronner, R., and Schmid, S. M. (2002b). The eastern Tonale fault zone: A 'natural laboratory' for crystal plastic deformation of quartz over a temperature range from 250 to 700 C. *Journal of Structural Geology*, 24(12):1861–1884.

Strachan, R., Collins, A., Buchan, C., Nance, R., Murphy, J., and D'Lemos, R. (2007). Terrane analysis along a Neoproterozoic active margin of Gondwana: insights from U-Pb zircon geochronology. *Journal of the Geological Society*, 164(1):57–60.

Thorpe, R. S. (1993). Geochemistry and eruptive environment of metavolcanic rocks from the Mona Complex of Anglesey, North Wales, U.K. *Geological Magazine*, 130(01):85–91.

Tucker, R. D. and Pharoah, T. C. (1991). U-Pb zircon ages for Late Precambrian igneous rocks in southern Britain. *Journal of the Geological Society*, 148(3):435–443.

Twiss, R. J. (1977). *Theory and Applicability of a Recrystallized Grain Size Paleopiezometer*, pages 227–244. Birkh{ä}user Basel, Basel.

Twiss, R. J. and Moores, E. M. (1992). *Structural Geology*. Macmillan.

Van de Kamp, P. C. (2008). Smectite-illite-muscovite transfomrations, quartz dissolution and silica release in shales. *Clays and clay minerals*, 56(1):66–81.

Violay, M., Gibert, B., Mainprice, D., Evans, B., Dautria, J. M., Azais, P., and Pezard, P. (2012). An experimental study of the brittle-ductile transition of basalt at oceanic crust pressure and temperature conditions. *Journal of Geophysical Research: Solid Earth*, 117(3):1–23.

Wakabayashi, J. (2015). Anatomy of a subduction complex: architecture of the Franciscan Complex, California, at multiple length and time scales. *International Geology Review*, 6814(February):37–41.

Wakabayashi, J. and Rowe, C. D. (2015). Whither the megathrust? Localization of large-scale subduction slip along the contact of a mélange. *International Geology Review*, 57(March):1–17.

Wakita, K. (2015). OPS mélange: a new term for mélanges of convergent margins of the world. *International Geology Review*, 57(5-8):529–539.

Waldron, J. W. F., Schofield, D. I., Dufrane, S. A., Floyd, J. D., Crowley, Q. G., Simonetti, A., Dokken, R. J., and Pothier, H. D. (2014). Ganderia-Laurentia collision in the Caledonides of Great Britain and Ireland. *Journal of the Geological Society*, 171(4):555–569.

Wang, K. and Bilek, S. L. (2014). Invited review paper: Fault creep caused by subduction of rough seafloor relief. *Tectonophysics*, 610:1–24.

Wheeler, J. (1992). Importance of pressure solution and coble creep in the deformation of polymineralic rocks. *Journal of Geophysical Research*, 97:4579–4586.

Wintsch, R. P., Christofferson, R., and Kronenberg, A. K. (1995). Fluid-rock reaction weakening of fault zones. *Journal of Geophysical Research*, 100(B7):13021–13032.

Wood, M. (2012). The Historical Development of the Term Mélange' and Its Relevance to the Precambrian Geology of Anglesey and the Lleyn Peninsula in Wales, UK. *Journal of Geography (Chigaku Zasshi)*, 121(1):168–180.

Zang, W. and Fyfe, W. S. (1995). Chloritization of the hydrothermally altered bedrock Igarap6 Bahia gold deposit, Carajas, Brazil. *Mineral. Deposita*, 30:30–38.

Appendices

A Muscovite composition

Muscovite composition in compound percentages and element per formula unit, based on 11 oxygen.

Table A.1: Sample AN16-022

Analysis #	1	2	3	4	5	6	7	8	9	10
Na2O	0	0	0.27	0.52	0	0.43	0	0	0	1.99
MgO	1.85	2.37	1.62	2.26	1.64	1.21	1.93	1.51	2.66	1.59
Al2O3	32.47	29.89	26.93	29.71	28.97	22.16	30.89	31.22	27.88	26.23
SiO2	52.58	53.01	52.77	54.48	53.02	64.95	53.48	53.68	53.9	58.96
K2O	10.46	10.89	12.31	10.06	11.13	7.69	10.19	10.04	10.06	6.95
TiO2	0	0	0.68	0	0.4	0	0	0	0.43	1.07
FeO	2.64	3.84	5.42	2.97	4.86	3.55	3.5	3.56	5.08	3.2
Total	100	100	100	100	100.02	99.99	99.99	100.01	100.01	99.99
Si	3.32	3.38	3.43	3.44	3.40	3.99	3.38	3.39	3.44	3.66
Ti	0.00	0.00	0.03	0.00	0.02	0.00	0.00	0.00	0.02	0.05
Al (IV)	0.68	0.62	0.57	0.56	0.60	0.01	0.62	0.61	0.56	0.34
Al	1.74	1.63	1.49	1.65	1.59	1.59	1.69	1.71	1.54	1.58
Fe	0.14	0.20	0.29	0.16	0.26	0.18	0.19	0.19	0.27	0.17
Mg	0.17	0.23	0.16	0.21	0.16	0.11	0.18	0.14	0.25	0.15
Na	0.00	0.00	0.03	0.06	0.00	0.05	0.00	0.00	0.00	0.24
K	0.84	0.89	1.02	0.81	0.91	0.60	0.82	0.81	0.82	0.55

Table A.2: Sample AN16-025

Analysis #	1	2	3	4	5	6	7	8
Na2O	0	0	0	0	0	0	0	0
MgO	1.8	18.02	1.5	2.47	2.04	1.96	2.43	2.29
Al2O3	31.53	24.26	32.29	30.62	30.19	30.38	29.04	29.02
SiO2	52.29	45.95	52.94	52.44	52.36	52.38	53.5	53.37
K2O	10.12	3.53	10.22	10.01	10.41	10.34	10.39	10.4
TiO2	0.83	0	0	0.43	0.52	0.74	0.42	0
FeO	3.43	8.23	3.04	4.03	4.49	4.2	4.21	4.92
Total	100	99.99	99.99	100	100.01	100	99.99	100
Si	3.31	2.96	3.34	3.33	3.34	3.34	3.41	3.41
Ti	0.04	0.00	0.00	0.02	0.02	0.04	0.02	0.00
Al (IV)	0.69	1.04	0.66	0.67	0.66	0.66	0.59	0.59
Al	1.67	0.80	1.74	1.63	1.61	1.62	1.59	1.59
Fe	0.18	0.44	0.16	0.21	0.24	0.22	0.22	0.26
Mg	0.17	1.73	0.14	0.23	0.19	0.19	0.23	0.22
Na	0.00	0.00	0.00	0.00	0.00	0.00	0.00	0.00
K	0.82	0.29	0.82	0.81	0.85	0.84	0.84	0.85

Table A.3: Sample AN16-026

Analysis #	1	2	3	4	5
Na2O	0.00	0.00	0.00	0.00	0.00
MgO	4.16	1.06	2.32	2.07	2.93
Al2O3	29.49	7.93	29.68	31.24	32.85
SiO2	52.06	15.72	51.62	52.24	51.32
K2O	9.34	3.28	10.57	10.35	9.75
TiO2	0.54	61.13	2.16	0.42	0.00
FeO	4.41	10.89	3.66	3.69	3.16
Total	100	100	100	100	100
Si	3.31	1.15	3.30	3.32	3.25
Ti	0.03	3.37	0.10	0.02	0.00
Al (IV)	0.69	2.85	0.70	0.68	0.75
Al	1.52	-2.16	1.53	1.66	1.69
Fe	0.23	0.67	0.20	0.20	0.17
Mg	0.39	0.12	0.22	0.20	0.28
Na	0.00	0.00	0.00	0.00	0.00
K	0.76	0.31	0.86	0.84	0.79

Table A.4: Sample AN16-027

Analysis #	1	2	3	4	5	6	7	8	9
Na2O	0.00	0.00	0.00	0.00	0.00	0.00	0.75	3.79	0.63
MgO	2.69	2.64	2.09	3.00	1.59	1.97	1.55	1.55	0.83
Al2O3	22.03	29.28	32.90	28.80	34.10	32.77	32.22	26.99	35.15
SiO2	61.58	54.81	51.55	54.01	51.68	52.50	52.24	55.21	49.32
K2O	7.73	10.61	11.21	10.59	10.83	10.73	9.61	8.88	10.39
TiO2	0.51	0.00	0.00	0.00	0.00	0.00	0.00	0.00	0.78
FeO	5.46	2.66	2.25	3.60	1.80	2.03	3.63	3.58	2.88
Total	100	100	100	100	100	100	100	100	100
Si	3.84	3.46	3.27	3.43	3.26	3.31	3.31	3.51	3.14
Ti	0.02	0.00	0.00	0.00	0.00	0.00	0.00	0.00	0.04
Al (IV)	0.16	0.54	0.73	0.57	0.74	0.69	0.69	0.49	0.86
Al	1.46	1.64	1.73	1.59	1.79	1.75	1.71	1.54	1.77
Fe	0.28	0.14	0.12	0.19	0.10	0.11	0.19	0.19	0.15
Mg	0.25	0.25	0.20	0.28	0.15	0.19	0.15	0.15	0.08
Na	0.00	0.00	0.00	0.00	0.00	0.00	0.09	0.47	0.08
K	0.61	0.85	0.91	0.86	0.87	0.86	0.78	0.72	0.84

Table A.5: Sample AN16-028

Analysis #	1	2	3	4	5
Na2O	0	0.577281	0	0	0
MgO	2.3025859	2.4186458	1.901366	1.813967	6.1256445
Al2O3	30.806952	30.903168	30.86506	31.823772	29.941992
SiO2	52.056914	51.709016	51.092747	50.888635	46.953888
K2O	10.512738	10.40126	12.179593	11.266595	9.1321661
TiO2	0.00	0.00	0.00	0.00	0.00
FeO	4.3208092	3.990629	3.9612327	4.2070313	7.8463086
Total	100	100	100	100	100
Si	3.32	3.30	3.29	3.27	3.07
Ti	0.00	0.00	0.00	0.00	0.00
Al (IV)	0.68	0.70	0.71	0.73	0.93
Al	1.64	1.63	1.64	1.67	1.37
Fe	0.23	0.21	0.21	0.23	0.43
Mg	0.22	0.23	0.18	0.17	0.60
Na	0.00	0.07	0.00	0.00	0.00
K	0.86	0.85	1.00	0.92	0.76

Table A.6: Sample AN16-005

Analysis #	1	2	3	4	5
Na2O	0.00	0.00	0.50	0.00	0.00
MgO	1.66	1.83	1.53	1.65	1.23
Al2O3	33.47	30.62	34.18	33.72	21.10
SiO2	52.99	57.20	51.27	52.27	70.10
K2O	10.45	8.85	9.80	10.33	5.64
TiO2	0.00	0.00	0.00	0.62	1.02
FeO	1.43	1.51	2.71	1.41	0.92
Total	100	100	100	100	100
Si	3.32	3.53	3.24	3.28	4.16
Ti	0.00	0.00	0.00	0.03	0.05
Al (IV)	0.68	0.47	0.76	0.72	-0.16
Al	1.79	1.76	1.78	1.77	1.64
Fe	0.08	0.08	0.14	0.07	0.05
Mg	0.16	0.17	0.14	0.15	0.11
Na	0.00	0.00	0.06	0.00	0.00
K	0.84	0.70	0.79	0.83	0.43

Table A.7: Sample AN16-006

Analysis #	1	2	3	4	5	6	7	8
Na2O	0.00	0.64	0.00	0.00	0.00	0.00	0.00	0.00
MgO	1.36	1.13	1.43	1.89	1.40	2.16	1.65	1.70
Al2O3	33.87	34.19	34.31	30.41	26.98	31.76	34.02	32.24
SiO2	49.41	50.58	51.45	55.87	61.18	54.88	53.25	51.27
K2O	9.95	10.07	9.76	9.67	8.72	9.85	9.66	10.10
TiO2	4.26	0.64	1.61	0.00	0.50	0.00	0.00	2.81
FeO	1.15	2.76	1.43	2.16	1.23	1.35	1.41	1.88
Total	100	100	100	100	100	100	100	100
Si	3.12	3.21	3.22	3.49	3.75	3.42	3.32	3.24
Ti	0.20	0.03	0.08	0.00	0.02	0.00	0.00	0.13
Al (IV)	0.88	0.79	0.78	0.51	0.25	0.58	0.68	0.76
Al	1.63	1.76	1.76	1.72	1.70	1.75	1.82	1.63
Fe	0.06	0.15	0.08	0.11	0.06	0.07	0.07	0.10
Mg	0.13	0.11	0.13	0.18	0.13	0.20	0.15	0.16
Na	0.00	0.08	0.00	0.00	0.00	0.00	0.00	0.00
K	0.80	0.81	0.78	0.77	0.68	0.78	0.77	0.81

Table A.8: Sample AN16-008

Analysis #	1	2	3	4	5	6	7	8	9	10
Na2O	0.70	0.00	0.00	0.00	0.45	0.00	0.00	0.48	0.00	0.00
MgO	0.81	1.06	0.79	0.97	1.33	1.15	0.95	1.05	1.24	1.31
Al2O3	38.95	35.71	43.00	36.66	32.51	34.24	34.21	35.21	33.26	33.74
SiO2	49.80	51.65	46.38	52.07	51.97	54.03	49.06	51.66	54.76	54.12
K2O	8.92	10.00	9.19	9.50	10.99	9.75	12.34	9.41	9.44	9.44
TiO2	0.00	0.48	0.00	0.00	0.56	0.00	2.22	0.98	0.00	0.00
FeO	0.81	1.10	0.63	0.81	2.19	0.83	1.22	1.22	1.30	1.40
Total	100	100	100	100	100	100	100	100	100	100
Si	3.10	3.23	2.89	3.23	3.29	3.35	3.13	3.23	3.40	3.36
Ti	0.00	0.02	0.00	0.00	0.03	0.00	0.11	0.05	0.00	0.00
Al (IV)	0.90	0.77	1.11	0.77	0.71	0.65	0.87	0.77	0.60	0.64
Al	1.96	1.86	2.05	1.92	1.72	1.86	1.71	1.82	1.83	1.83
Fe	0.04	0.06	0.03	0.04	0.12	0.04	0.07	0.06	0.07	0.07
Mg	0.07	0.10	0.07	0.09	0.13	0.11	0.09	0.10	0.11	0.12
Na	0.09	0.00	0.00	0.00	0.06	0.00	0.00	0.06	0.00	0.00
K	0.71	0.80	0.73	0.75	0.89	0.77	1.00	0.75	0.75	0.75

Table A.9: Sample AN16-010

Analysis #	1	2	3	4	5	8	9	6
Na2O	0.00	1.14	0.00	0.00	0.00	0.00	1.97	0.00
MgO	1.05	1.23	1.46	1.07	1.50	0.81	1.08	0.00
Al2O3	36.24	34.98	34.90	36.56	35.23	37.02	34.12	41.16
SiO2	49.91	51.80	51.57	50.89	50.64	51.33	51.49	48.60
P2O5	0.00	0.00	0.00	0.00	0.00	0.00	0.76	0.00
K2O	9.66	8.64	9.73	10.31	10.71	9.72	8.09	8.42
TiO2	0.00	0.00	0.91	0.00	0.61	0.00	0.00	0.00
FeO	3.14	2.22	1.44	1.16	1.32	1.11	2.49	1.82
Total	100	100	100	100	100	100	100	100
Si	3.15	3.24	3.23	3.19	3.19	3.20	3.25	3.02
Ti	0.00	0.00	0.04	0.00	0.03	0.00	0.00	0.00
Al (IV)	0.85	0.76	0.77	0.81	0.81	0.80	0.75	0.98
Al	1.85	1.82	1.80	1.89	1.80	1.92	1.80	2.04
P	0.00	0.00	0.00	0.00	0.00	0.00	0.04	0.00
Fe	0.17	0.12	0.08	0.06	0.07	0.06	0.13	0.09
Mg	0.10	0.11	0.14	0.10	0.14	0.08	0.10	0.00
Na	0.00	0.14	0.00	0.00	0.00	0.00	0.24	0.00
K	0.78	0.69	0.78	0.82	0.86	0.77	0.65	0.67

Table A.10: Sample AN16-011

Analysis #	1	2	3	4	5	6	7	8
Na2O	0.00	0.00	0.00	0.00	0.00	0.00	0.00	0.00
MgO	1.74	3.16	1.94	1.62	1.20	1.94	3.00	2.23
Al2O3	32.21	31.28	27.57	33.96	32.53	31.53	26.72	29.44
SiO2	50.96	52.21	60.24	52.20	49.26	51.92	49.64	51.15
K2O	10.75	10.80	9.00	10.65	10.33	9.31	9.75	11.02
TiO2	0.00	0.00	0.00	0.00	1.80	0.00	8.34	0.00
FeO	4.34	2.55	1.25	1.57	4.89	5.30	2.56	6.16
Total	100	100	100	100	100	100	100	100
Si	3.26	3.31	3.70	3.28	3.17	3.30	3.18	3.31
Ti	0.00	0.00	0.00	0.00	0.09	0.00	0.40	0.00
Al (IV)	0.74	0.69	0.30	0.72	0.83	0.70	0.82	0.69
Al	1.69	1.65	1.70	1.80	1.63	1.67	1.19	1.56
Fe	0.23	0.14	0.06	0.08	0.26	0.28	0.14	0.33
Mg	0.17	0.30	0.18	0.15	0.11	0.18	0.29	0.22
Na	0.00	0.00	0.00	0.00	0.00	0.00	0.00	0.00
K	0.88	0.87	0.71	0.85	0.85	0.76	0.80	0.91

B Chlorite composition

Chlorite composition in compound percentages and element per formula unit, based on 28 oxygen. T(C) means temperature calculated according to Cathelineau (1988), T(Z) means temperature calculated using the method by Zang and Fyfe (1995) and T(K) means temperature calculated using the method by Kranidiotis and MacLean (1987). Temperatures are in °C. Values in red have too high calcium, sodium and potassium to be reliable indicators for paleotemperatures, corrected average temperature is without these measurements.

Table B.1: Sample AN16-022

Analysis #	1	2	3*	4	5	6	7	8	9	average	corrected average
Na2O	0	0.7	0.91	0	0.88	0.52	0.64	0	0		
MgO	16.28	14.8	10.34	15.22	14.51	13.14	14.85	15.59	15.57		
Al2O3	23.26	23	20.61	24.03	22.88	20.22	23.27	22.92	23.19		
SiO2	32.61	33.57	48.97	31.32	35.06	43.9	33.85	32.14	35.49		
K2O	0	0	0.85	0	0	0.22	0	0.32	1.36		
CaO	0	0	0	0	0	0	0	0	0		
TiO2	0	0	0	0	0	0	0	0	0		
MnO	1.7	2.11	1.23	2.33	1.92	1.55	2	1.98	1.71		
FeO	26.15	25.82	17.08	27.09	24.75	20.44	25.4	27.05	22.68		
Total	100	100	99.99	99.99	100	99.99	100.01	100	100		
Si	5.93	6.11	8.23	5.75	6.32	7.58	6.13	5.90	6.35		
Ti	0.00	0.00	0.00	0.00	0.00	0.00	0.00	0.00	0.00		
Al(IV)	2.07	1.89	-0.23	2.25	1.68	0.42	1.87	2.10	1.65		
Al(VI)	2.92	3.04	4.32	2.95	3.18	3.69	3.10	2.86	3.24		
Fe	3.98	3.93	2.40	4.16	3.73	2.95	3.85	4.15	3.39		
Mn	0.26	0.33	0.18	0.36	0.29	0.23	0.31	0.31	0.26		
Mg	4.42	4.01	2.59	4.17	3.90	3.38	4.01	4.27	4.15		
Ca	0.00	0.00	0.00	0.00	0.00	0.00	0.00	0.00	0.00		
Na	0.00	0.25	0.30	0.00	0.31	0.17	0.22	0.00	0.00		
K	0.00	0.00	0.18	0.00	0.00	0.05	0.00	0.07	0.31		
Fe/(Fe+Mg+Mn)	0.46	0.48	0.46	0.48	0.47	0.45	0.47	0.48	0.43		
Ca+Na+K	0.00	0.25	0.48	0.00	0.31	0.22	0.22	0.07	0.31		
T(C)	270.9	242.9	-99.5	299.8	208.8	5.8	238.6	276.2	203.6	183	282
T(Z)	225.9	205.9	-18.9	243.2	183.9	51.9	203.5	227.9	183.8	167	232
T(K)	271.3	253.9	27.7	291.7	231.2	96.0	250.8	275.9	225.0	214	280

*possibly mixed with quartz

Table B.2: Sample AN16-025

Analysis #	1*	2	3	4	5	average	corrected average
Na2O	1.2	0	0	0	0		
MgO	13.65	27.81	27.68	29.13	28.95		
Al2O3	16.55	23.13	22.3	24.51	24.34		
SiO2	28.02	38.25	38.64	34.55	36.05		
K2O	1.34	0.56	1.14	0	0		
CaO	0	0	0	0	0		
TiO2	5.98	0	0	0	0		
MnO	0	0	0	0	0		
FeO	33.26	10.25	10.25	11.82	10.67		
Total	100	100	100.01	100.01	100.01		
Si	5.43	6.38	6.47	5.84	6.04		
Ti	0.87	0.00	0.00	0.00	0.00		
Al(IV)	2.57	1.62	1.53	2.16	1.96		
Al(VI)	1.21	2.93	2.87	2.72	2.84		
Fe	5.39	1.43	1.43	1.67	1.49		
Mn	0.00	0.00	0.00	0.00	0.00		
Mg	3.94	6.92	6.91	7.34	7.23		
Ca	0.00	0.00	0.00	0.00	0.00		
Na	0.45	0.00	0.00	0.00	0.00		
K	0.33	0.12	0.24	0.00	0.00		
Fe/(Fe+Mg+Mn)	0.58	0.17	0.17	0.19	0.17		
Ca+Na+K	0.78	0.12	0.24	0.00	0.00		
T(C)	351.7	198.3	184.7	286.3	254.1	255	246
T(Z)	268.2	204.9	195.9	261.7	241.8	234	236
T(K)	333.2	202.1	193.1	261.0	238.8	246	234

*possibly mixed with rutile

Table B.3: Sample AN16-026

Analysis #	1	2	3	4	5*	6*	7	average	corrected average
Na2O	0.80	1.33	0.00	0.00	0.00	0.00	0.00		
MgO	29.81	27.72	32.18	32.98	28.61	32.39	32.49		
Al2O3	21.85	22.42	23.57	23.63	24.52	24.10	23.71		
SiO2	37.87	39.54	35.28	34.42	36.98	34.47	34.47		
K2O	0.00	0.23	0.00	0.00	1.68	0.00	0.00		
CaO	0.36	0.00	0.00	0.00	0.00	0.00	0.00		
TiO2	0.93	0.89	0.00	0.00	0.00	0.00	0.00		
MnO	0.00	0.00	0.00	0.00	0.00	0.00	0.00		
FeO	8.37	7.88	8.97	8.97	8.20	9.04	9.34		
Total	100.00	100.00	100.00	100.00	100.00	100.00	100.00		
Si	6.30	6.54	5.89	5.76	6.17	5.77	5.78		
Ti	0.12	0.11	0.00	0.00	0.00	0.00	0.00		
Al(IV)	1.70	1.46	2.11	2.24	1.83	2.23	2.22		
Al(VI)	2.58	2.90	2.53	2.42	2.99	2.52	2.46		
Fe	1.16	1.09	1.25	1.26	1.14	1.27	1.31		
Mn	0.00	0.00	0.00	0.00	0.00	0.00	0.00		
Mg	7.39	6.83	8.01	8.23	7.11	8.08	8.12		
Ca	0.06	0.00	0.00	0.00	0.00	0.00	0.00		
Na	0.26	0.43	0.00	0.00	0.00	0.00	0.00		
K	0.00	0.05	0.00	0.00	0.36	0.00	0.00		
Fe/(Fe+Mg+Mn)	0.14	0.14	0.14	0.13	0.14	0.14	0.14		
Ca+Na+K	0.32	0.47	0.00	0.00	0.36	0.00	0.00		
T(C)	212.2	173.8	277.7	298.5	233.1	297.8	296.1	256	293
T(Z)	217.4	191.9	260.7	274.7	230.9	273.9	272.5	246	270
T(K)	208.6	183.4	251.7	265.2	222.5	264.9	264.0	237	261

*analyses 5 and 6 are chlorite inside vesicles

Table B.4: Sample AN16-027

Analysis #	1	2	3	average	corrected average
Na2O	0.00	0.00	0.00		
MgO	12.52	20.42	18.39		
Al2O3	30.13	25.65	24.44		
SiO2	44.93	30.88	33.23		
K2O	6.66	0.00	0.00		
CaO	0.00	0.00	0.00		
TiO2	0.00	0.00	0.00		
MnO	0.00	0.00	0.00		
FeO	5.75	23.06	23.94		
Total	100.00	100.00	100.00		
Si	7.36	5.51	5.92		
Ti	0.00	0.00	0.00		
Al(IV)	0.64	2.49	2.08		
Al(VI)	5.18	2.91	3.06		
Fe	0.79	3.44	3.57		
Mn	0.00	0.00	0.00		
Mg	3.06	5.43	4.89		
Ca	0.00	0.00	0.00		
Na	0.00	0.00	0.00		
K	1.39	0.00	0.00		
Fe/(Fe+Mg+Mn)	0.21	0.39	0.42		
Ca+Na+K	1.39	0.00	0.00		
T(C)	40.5	338.2	272.5	217	305
T(Z)	97.7	277.0	230.4	202	254
T(K)	100.7	310.2	269.5	227	290

Table B.5: Sample AN16-028

Analysis #	1	2	3	4*	5*	6*	7	8	9	10	average	corrected average
Na2O	0.00	0.00	0.00	0.00	0.00	0.00	0.00	0.00	0.00	0.00		
MgO	21.56	23.88	22.34	22.43	23.14	22.27	16.95	15.62	19.38	23.56		
Al2O3	24.19	22.16	22.97	22.84	23.28	23.89	24.13	25.57	24.51	23.45		
SiO2	31.12	34.16	31.84	32.62	31.96	31.59	40.00	40.15	36.70	33.46		
K2O	0.00	0.00	0.00	0.00	0.00	0.00	3.86	3.56	2.08	0.00		
CaO	0.00	0.00	0.00	0.00	0.00	0.00	0.00	0.00	0.00	0.00		
TiO2	0.00	0.00	0.00	0.00	0.00	0.00	0.00	0.00	0.00	0.00		
MnO	0.80	0.00	0.58	0.00	0.66	0.00	0.00	0.00	0.00	0.00		
FeO	22.33	19.80	22.27	22.11	20.97	22.25	15.06	15.11	17.33	19.53		
Total	100.00	100.00	100.00	100.00	100.00	100.00	100.00	100.00	100.00	100.00		
Si	5.57	5.99	5.69	5.80	5.68	5.63	6.87	6.87	6.37	5.86		
Ti	0.00	0.00	0.00	0.00	0.00	0.00	0.00	0.00	0.00	0.00		
Al(IV)	2.43	2.01	2.31	2.20	2.32	2.37	1.13	1.13	1.63	2.14		
Al(VI)	2.67	2.57	2.53	2.58	2.55	2.64	3.76	4.02	3.38	2.70		
Fe	3.34	2.90	3.33	3.29	3.11	3.31	2.16	2.16	2.51	2.86		
Mn	0.12	0.00	0.09	0.00	0.10	0.00	0.00	0.00	0.00	0.00		
Mg	5.75	6.24	5.95	5.94	6.13	5.91	4.34	3.98	5.01	6.15		
Ca	0.00	0.00	0.00	0.00	0.00	0.00	0.00	0.00	0.00	0.00		
Na	0.00	0.00	0.00	0.00	0.00	0.00	0.00	0.00	0.00	0.00		
K	0.00	0.00	0.00	0.00	0.00	0.00	0.85	0.78	0.46	0.00		
Fe/(Fe+Mg+Mn)	0.36	0.32	0.36	0.36	0.33	0.36	0.33	0.35	0.33	0.32		
Ca+Na+K	0.00	0.00	0.00	0.00	0.00	0.00	0.85	0.78	0.46	0.00		
T(C)	329.5	261.5	310.1	292.6	312.3	320.2	119.6	120.4	201.3	282.3	255	301
T(Z)	273.6	233.0	261.5	249.9	265.0	267.8	137.9	136.7	191.7	246.7	226	257
T(K)	302.6	254.5	289.3	277.8	289.1	296.2	162.2	164.1	216.1	268.2	252	283

*Analyses 4, 5 and 6 are chlorite in vesicles, others are chlorite in veins

Table B.6: Sample AN16-006

Analysis #	1
Na2O	2.57
MgO	9.39
Al2O3	33.23
SiO2	43.03
K2O	0.00
CaO	0.58
TiO2	1.24
MnO	0.00
FeO	9.97
Total	100.00
Si	7.00
Ti	0.15
Al(IV)	1.00
Al(VI)	5.37
Fe	1.36
Mn	0.00
Mg	2.28
Ca	0.10
Na	0.81
K	0.00
Fe/(Fe+Mg+Mn)	0.37
Ca+Na+K	0.91
T(C)	99.0
T(Z)	120.6
T(K)	151.7